“Molecular Dynamics of Shock Wave Interaction with Nanoscale Structured Materials”

by

Ahmad K Al-Qananwah

A dissertation submitted to the Graduate Faculty in Mechanical Engineering in partial fulfillment of the requirements for the degree of Doctor of Philosophy, The City University of New York

2012

This manuscript has been read and accepted for the Graduate Faculty in Engineering in satisfaction of the dissertation requirement for the degree of Doctor of Philosophy.

January 31, 2012 — Professor Yiannis Andreopoulos

Date

Chair of Examining Committee

January 31, 2012 — Professor Mumtaz Kassir

Date

Executive Officer

Professor Joel Koplik

Professor Charles Watkins

Professor Doyle Knight

Supervisory Committee

THE CITY UNIVERSITY OF NEW YORK

Abstract

"Molecular Dynamics of Shock Wave Interaction with Nanoscale Structured Material"

by

Ahmad K Al-Qananwah

Adviser: Professor Yiannis Andreopoulos

Co-adviser: Professor Joel Koplik

[Typical theoretical treatments of shock wave interactions are based on a continuum approach, which cannot resolve the spatial variations in solids with nano-scale porous structure. Nano-structured materials have the potential to attenuate the strength of traveling shock waves because of their high surface-to-volume ratio. To investigate such interactions we have developed a molecular dynamics simulation model, based on Short Range Attractive interactions. A piston, modeled as a uni-directional repulsive force field translating at a prescribed velocity, impinges on a region of gas which is compressed to form a shock, which in turn is driven against an atomistic solid wall. Periodic boundary conditions are used in the directions orthogonal to the piston motion, and we have considered solids based on either embedded atom potentials (target structure) or tethered potential (rigid piston, holding wall). Velocity, temperature and stress fields are computed locally in both gas and solid regions, and displacements within the solid are interpreted in terms of its elastic constants. In this work we present results of the elastic behavior of solid structures subjected to shock wave impact and analysis of energy transport and absorption in porous materials**.** The results indicated that the presence of nano-porous material layers in front of a target wall reduced the stress magnitude detected inside and the energy deposited there by about 30 percent while, at the same time, its loading rate was decreased substantially**]**

To the souls of my late parents

Acknowledgments

I would like to thank the faculty of the mechanical engineering department for their cooperation and support.

Foremost, I would like to express my sincere gratitude to my advisor Prof. Y. Andreopoulos for the continuous support of my Ph.D study and research, for his patience, motivation, enthusiasm, and immense knowledge that let me explore the unknown and taught me to observe problems in an engineer's point of view. His guidance helped me in all the time of research and writing of this thesis.

I would like to express my gratitude to Prof. Joel Koplik for his guidance, attention and efforts that he provided me with during the course of this research.

In fact prof. Andreopoulos and prof. Koplik have always provided me with valued constructive instructions accompanied with the ultimate support and concern without it this thesis would have been very difficult to accomplish.

I would like to thank the esteemed members of the examination committee for their participation and cooperation.

Finally, I would like express my great appreciation of the NSF financial support.

Table of Contents

Nomenclature

B	Bulk Modulus
C_{11}, C_{12}, C_{44}	The three distinct elastic constants (in Voigt notation)
E	Total energy
F	Force
G	Shear modulus
I	Impulse
K	Kinetic energy
m	Mass
N	Number of particles
n	Number density
P	Pressure
q	Heat flux
r	Position vector
T	Temperature
t	Time

U	Interaction potential
V	Volume
v	Velocity
v_p	Piston velocity
v_s	Shock speed
w	Weight function
α	Embedding strength
η	Porosity
Θ	Embedding function
Λ	Shock thickness
ρ	Density
ς	Strain
$\dot{\varsigma}$	Strain rate
σ	Stress
Φ_0	Energy Scale
ψ	Length Scale

List of Tables

List of Figures

Introduction

i. Motivation

Typical theoretical treatments of shock wave interactions are based on a continuum approach, which cannot resolve the spatial variations in solids with nano-scale porous structure. Typically the shock wave is treated as a discontinuity. The problem of mutual interaction between shockwave and solid has been only sparsely investigated at small time and length scales using Molecular Dynamics.

Several studies have been carried out to investigate the motion of shockwaves in fluids or waves in solids using continuum mechanics. However, the mutual interaction which takes place during the impact of the shockwave on the solid is more challenging to capture.

In this research we are trying to investigate this mutual interaction between fluid and solid at the nano-scale and particularly look at the energy transfer from the fluid to the solid by looking at the dissipative mechanisms. It's particularly intriguing to take advantage of the large surface to volume ratio available in nano-porous material.

ii. Literature review

Nanotechnology offers researchers the potential for creating unprecedented new materials with enhanced properties and devices that operate at length scales where classical Newtonian physics breaks down. Materials such as microframe structures with nano-trusses and nano-structure porous materials are seen as potentially revolutionizing the field of blast and ballistic protection. Structured nano materials because of their high surface-to-volume ratio offer an unprecedented

platform to manipulate shock or blast waves propagating through them and mitigate their effect by dissipation or phase cancellation. Understanding and predicting the behavior of material under the effects of dynamical thermomechanical extremes requires knowledge of interactions at the atomic, molecular, and microstructural levels. This understanding may lead to better ways of controlling them and design new materials for future applications.

At the continuum level, a shock is assumed to be a discontinuity with unknown properties, since the shock thickness is not resolved and its reflection occurs instantaneously. Realistically, for typical shock thicknesses and propagation velocities of 100 nm and 400 m/s, respectively, the interaction time is 0.25 ns. Thus the fast time- and small length- scales of this interaction necessitate the use of atomistic level computer simulations. The present work, which is an outgrowth of our experimental work with periodic composite structures and functionally graded materials subjected to shock loading [1-5], is aiming at a better understanding of the interaction of propagating shock waves with structured porous materials at the nanoscale level.

The novelty of the present work is in the nanoscale resolution of the mutual interaction between a shock wave and structured materials which includes, for the first time, a simultaneous and integrated/coupled treatment of multiple wave phenomena in both gas and solid phases. The objective of our current research is to develop a physical understanding and quantitative predictive capability to deal with the complex interactions between nanoscale materials and shock waves. This is accomplished by using molecular dynamics (MD) simulations. The present work in addition to extending our physical understanding has the potential to bridge the gap between atomistic and meso-scale modeling. Previous work describes shock interactions only at a much coarser level by averaging over atomic variables, and can only address this issue by trial and error.

An extensive but non exhaustive review on the subject of propagation of nonlinear waves in porous media at the macroscopic level can be found in [6]. Of particular interest is the interaction of shock waves with gas-solid mixtures where a substantial amount of experimental theoretical and computational work has been reported. It is reasonably well documented that shock waves propagating in foams or porous materials are attenuated [7, 8] and such accurately controllable shock attenuations are widely used in various engineering and industrial applications.

Modeling these phenomena is based on microscopic conservation laws (mass, momentum, and energy) from which macroscopic evolution equations (ordinary and partial differential equations) are derived, complemented by appropriate closures. Single and multi-phase approaches have been developed [9, 10]. The first fundamental study on the subject is that of Biot [11] on compression wave propagation by using poro-mechanics. A large number of papers have appeared in the literature following Biot's pioneering work, referring to microscopic representations of the phase balance equations within the framework of the theory of mixtures, but applying these concepts to nonlinear waves led to poor results. A more accurate representation of the momentum and energy processes at the internal surfaces of the porous medium was introduced [12] by including the Forchheimer term in the model of [13]. The basic paradox of these equations is that although they are inviscid in nature, so that the shock wave motion is adequately captured and resolved, the Forchheimer term, which approximately accounts for energy losses inside the pores, contains viscous effects.

It has been shown that upon the shock wave loading of a saturated porous material, the initial step-wise perturbation is split into two parts [14, 15]: the first wave in which pore fluid and porous material are compressed simultaneously, i.e. the solid and fluid particles have in phase

motion, and a second wave in which the pore fluid is compressed again, while the porous material relaxes, i.e. the two phases have out of phase motion. In some papers these two waves are known as deformation (fast, mode 1) and filtration (slow, mode 2) waves.

Grinten [15] found experimentally that the pressure inside the porous specimen increases gradually and no wave structure is evident in the pressure signals, suggesting that the wave propagation through the material is fully dispersed. In addition the fluid solid interaction has a non-linear nature as a non-linear drag law known as Forchheimer term in the momentum transport equation, was shown to best fit the data. In similar experiments, Levy et al. [17] found that the compaction wave broadness as it travels through the specimen and becomes dispersed.

In general, waves through porous materials will be attenuated. However, substantial amplification can occur when the material is placed in the vicinity or in contact with a backing plate [7, 8]. If porous materials are used as barriers to protect structures measurement of the total stress transmitted to the backing wall is more important than the pressure in the fluid phase. Such measurements have been reported in cases of polymeric (flexible) foams and granular materials under shock compaction [14, 18].

Yasuhara et al. [19] investigated experimentally the effect of porosity and the internal structure on the total stress at the back wall. For all foams tested in these experiments the maximum transient total stress at the back wall is larger than the pressure behind the reflected shock off a rigid wall. It was also observed that there is a delay time for the total stress rise compared to the rise of the pressure upon the reflection of the incident shock wave off a rigid wall suggesting that the stress wave transmitting through the foam decelerates as it moves within the foam.

Ben-Dor et al. [21] conducted a series of experiments on different types of granular materials where pressures in front, behind and within the granular material were recorded during the

impact with weak shock waves. The stress within the granular materials and the total stress at the back wall were measured. It was observed that the pressure behind the shock wave reflected off the material front face reaches the value of the pressure behind a reflected shock over a sold surface.

The experiments of Britan & Ben-Dor [20] concluded that the gas flow in the granular material due to the impact of the shock on the specimen is the main reason for the formation of the total stress at the end-wall which increases its peak value due to the additional compressive drag force that is applied on the granular particles. These authors argue that filtration process causes energy loss in the transmitted stress wave in the granular material, thus reducing the stress value.

The recent work by Kazemi-Kamyab et al. [6], which has focused on the effects rigid open-cell metallic (or ceramic) foams have in the transmission of stresses to a structure impacted by a shock wave, has shown that carefully selecting a porous material and its size it is possible to cancel out the contributions from the gas and solid phases and therefore avoid the stress wave overshot inside the back wall. The measured time-dependent signals were decomposed into two components, one with low frequency content which is argued that it is associated with Biot's slow wave and one with high frequency contributions which corresponds to the fast wave propagation. It is also argued that this decomposition can differentiate the effects of gas pressure in the pores from the stress in the matrix of the porous medium.

Shock wave experiments are particularly well suited for molecular dynamic (MD) simulations because in such experiments sample sizes are small and time scales are short, in the past few decades, many studies were carried out to investigate the behavior of the flow in the presence of a shockwave through molecular dynamics. Tsai et al. [33] studied the propagation of a planar shock in a dense Lennard-Jones fluid. Hoover [37] simulated the structure of a shock wave front

in a dense Lennard-Jones fluid, and found a good agreement with the solutions of the Navier-Stokes equation for strong shock. Holian, et al. [34] used 4,800 particles to simulate a dense-fluid shock wave and found differences to be relatively small when compared with the Navier-Stokes continuum mechanics. Holian [35] demonstrated that constitutive model of Navier Stokes hydrodynamics was accurate even on time and distance scales of MD. Woo et al. [36] have simulated piston-driven shock wave in hard sphere gas at Mach 1.5, 3, and 10. Schlamp et al. [37] simulated shock waves in dense nitrogen via Non-Equilibrium Molecular Dynamics "NEMD" and the steady state shock structure is resolved with 0.25 °A resolution, corresponding to 0.1 mean–free paths or 1/30th of the shock thickness.

Chapter One

Fundamentals

Statistical physics aims to explain the thermo-physical properties of matter and dynamic phenomena occurring in non-equilibrium processes on the basis of the properties of atoms and molecules and their interactions. Molecular Dynamics (MD) and Monte Carlo (MC) computer simulations performed during the recent decades have helped enormously to achieve this goal. The study of models plays an important role. Simple systems composed of "effectively" spherical particles are modeled with potentials that are linear combination of the inverse power of the distance *r* between two particles.

1.1 What is molecular dynamics?

It's a computer simulation technique where the time evolution of a set of interacting atoms is followed by integrating their equations of motion. The laws of classical mechanics are followed and most notably Newton's law: $F_i = m_i a_i$ for each atom i in a system constituted by N atoms. Where: m_i is the atom mass, r_i its position vector, $a_i = \frac{\partial^2 r_i}{\partial t^2}$ its acceleration, and F_i is the force acting upon it due to interactions with other atoms.

Molecular dynamics is a deterministic technique: given an initial set of positions and velocities, the subsequent time evolution is in principle completely determined. In more pictorial terms, atoms will "move" into the computer bumping into each other, wandering around, oscillating in

waves in concert with their neighbors, perhaps evaporating away from the system if there is a free surface, and so on, in away pretty similar to what atoms in a real substance would do.

1.2 Intermolecular potentials

The main ingredient of a simulation is the model for the physical system. For a molecular dynamics simulation this amounts to choosing the potential. A function $U(r_1, r_2, r_3....r_N)$ of the positions of the nuclei represents potential energy of the system when the atoms are arranged in that specific configuration. This function is usually constructed from the relative positions of the atoms with respect to each other, rather than from the absolute positions.

Forces are then derived as the gradients of the potential with respect at atomic displacements:

$$F_i = -\nabla_{r_i} U(r_1, r_2, r_3....r_N) \quad \text{…….. (1.1}$$

This form implies the presence of a conservation law of the total energy E=K+U, where K is the instantaneous kinetic energy.

The potential 'U' is often taken to be pair wise additive; that's, the interaction energy among N atoms is the sum of isolated two body contributions.

$$U(r^N) = \sum_{i>j} \sum u(r_{ij}) \quad \text{…….. (1.2}$$

Where $r^N = \{r_1, r_2, r_3....r_N\}$, set of sphere position vector, u: two body potential and $r_{ij} = \left| r_i - r_j \right|$, the scalar distance between the centers of atoms *i* and *j*.

1.2.1 Short Range Attractive Potential “SHRAT”

The standard Lennard Jones potential reads

$$U^{LJ} = 4\Phi_0\left(\left(\frac{\psi}{r}\right)^{12} - \left(\frac{\psi}{r}\right)^{6}\right), \quad r \le 2.5\psi \quad \ldots\ldots\ldots (1.3$$

where ψ, Φ_0 are length and energy scales respectively. The Short Range attractive potential takes the form [26,27]:

$$U^{SHRAT}(r) \sim \begin{cases} 3\left(r_{cut} - r\right)^4 - \left(r_{cut} - r_{\min}\right)\left(r_{cut} - r\right)^3, & r \le h \\ 0 & ,r > h \end{cases} \quad \ldots\ldots\ldots (1.4$$

This function has a minimum at $r = r_{\min}$. It intersects the horizontal axis (U=0) at $\psi = (4/3)r_{\min} - (1/3)r_{cut}$

This functional form has been used for the effective two-particle interaction in a variant of the embedded atom method for metals. For $r_{cut} = (113/81)\psi \approx 1.4\psi$ and $r_{\min} = (89/81)\psi \approx 1.1\psi$ the force at $r = \psi$ and the potential depth at $r = r_{\min}$ are equal to the corresponding values of LJ values. The resulting potential becomes

$$U^{SHRAT}(r) = 24\Phi_0\left(1 - r/\psi\right)\left[\left(r_{cut} - r\right)/\left(r_{cut} - r_{\min}\right)\right]^3, \quad r \le r_{cut} \quad \ldots\ldots\ldots (1.5$$

Choosing $r_{cut} = (3/2)\psi$ *and* $r_{\min} = (9/8)r_0$ and setting the depth of potential to Φ_0, in analogy to LJ potential, the explicit expression for the short range attractive model potential therefore reads

$$U^{SHRAT}(r)=\begin{cases}\frac{512}{27}\Phi_0\left(1-\frac{r}{\psi}\right)\left(3-2\frac{r}{\psi}\right)^3, & r\le 1.5\psi \\ 0 & ,r>1.5\psi\end{cases} \quad \text{…….. (1.6}$$

In units of Φ_0/ψ, the force at $(r=\psi)$ =512/27$\approx$19. The corresponding value for the LJ potential is 24. Notice that this potential is finite at *r=0,* $U^{SHRAT}(0)=\frac{512}{27}\Phi_0$.

Here, the cutoff is rather short ranged and smooth, such that not only the potential but also its first and second derivatives vanish at the cutoff distance. For temperatures below $10\Phi_0/k_B$, this is of no practical concern since the Boltzmann factor $\exp(-\Phi_0/k_BT)$ governing the fraction of particles that can reach this distance is less than $6x10^{-23}$.

In dimensionless notation, the LJ and SHRAT potentials read $U^{LJ}=4\left(r^{-12}-r^{-6}\right)$ and

$$U^{SHRAT}(r)=\begin{cases}\frac{512}{27}(1-r)(3-2r)^3, & r\le 3/2 \\ 0 & ,r>3/2\end{cases} \quad \text{…….. (1.7}$$

Both U^{LJ} and U^{SHRAT} are plotted in fig 1.1.

The Lorentz-Berthelot mixing rules are used for estimating intermolecular potential parameters between pairs of non-identical molecules, for the interaction of hetero-atomic pairs, the effective values of ψ and Φ_0 are calculated from those for the homo-atomic pairs using the mixing rules: arithmetic mean for ψ : $\psi_{ab}=\frac{1}{2}(\psi_a+\psi_b)$ and geometric mean for Φ_0: $\Phi_{0ab}=\sqrt{\Phi_{0a}\Phi_{0b}}$.

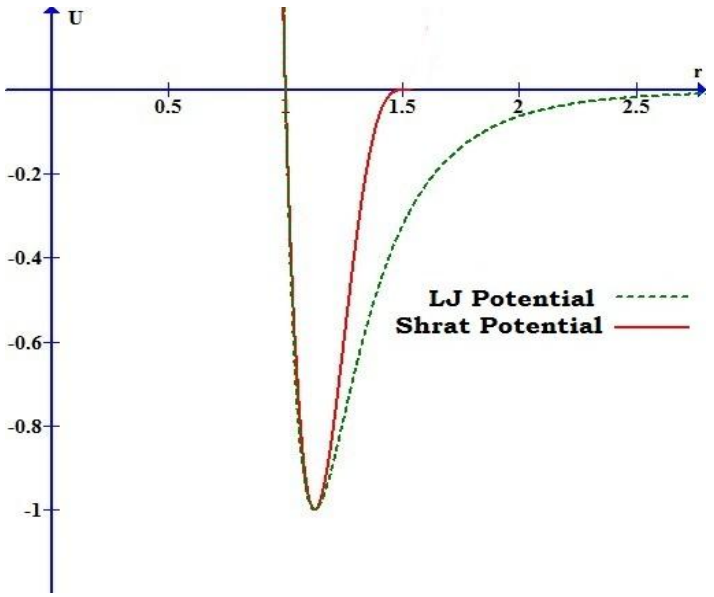

Fig 1.1 Lennard Jones potential and SHRAT Potential

1.2.2 Tethering potential

The tethering potential is introduced to better improve the elastic properties of the atomistic system where better solid behavior in terms of limiting the tendency of systems to deform or break is sought. The atomic sites are allowed to be tethered to a fixed point in space r_0, taken as their position at the beginning of the simulation. This is also known as position restraining. The specification, which comes as part of the molecular description, requires a tether potential type and the associated interaction parameters. Note, firstly, that application of tethering potentials means that momentum will no longer be a conserved quantity of the simulation. Secondly, in constant pressure simulations, where the MD cell changes size or shape, the reference position is scaled with the cell vectors.

The Harmonic potential $U^{teth}(r_{i0}) = 0.5k(r_{i0})^2$ …….(1.8

Where r_{i0} is the distance of the atom from its position at t=0, and k is the tethering constant . The force on the atom *i* arising from a tether potential is obtained using the general formula:

$$\underline{F}(r_{i0}) = -\frac{1}{r_{i0}}\left[\frac{\partial}{\partial r_{i0}} U^{teth}(r_{i0})\right]\underline{r}_{i0} = -k.\underline{r}_{i0} \text{ …….(1.9}$$

The contribution to be added to the atomic virial is given by

$$vir = \underline{r}_{i0}.\underline{F}(r_{i0}) = -k(r_{i0})^2 \text{ ……..(1.10}$$

The contribution to be added to the atomic stress tensor is given by

$$\sigma^{\mu\nu} = -\underline{r}^{\mu}_{io}.\underline{f}^{\nu}(r_{i0}) = k(\underline{r}^{\mu}_{io}.\underline{r}^{\nu}_{io}) \text{ …….(1.11}$$

where μ and ν indicate the ***x, y*** and ***z*** components. The atomic stress tensor derived in this way is symmetric.

1.2.3 Generic Embedded Atom Potential "GEAM"

Consider a model metal composed of N atoms at thermal equilibrium at temperature T located at positions $r^i, i = 1,2,..N$ contained in a volume V. The potential is the sum of two contributions to the total potential energy E: a conventional binary interaction term through a two-body interaction potential U and a term stemming from an embedding functional F , which models the effect of the electronic "glue" between atoms [30,31]

$$E = \sum_{i=1}^{N} \Theta(\rho_i^{emb}) + \sum_{j>i}^{N} U(r_{ij}) \ldots\ldots.(1.12$$

where r_{ij} denotes the norm of the relative vector $\mathrm{r}_{ij} = \mathrm{r}_i - \mathrm{r}_j$ between atoms *i* and *j*.

The embedding functional Θ has to be a nonlinear function of the (local) embedding densities ρ_i^{emb} of atoms $i = 1,2,..N$. The local embedding density ρ_i^{emb} is constructed from the radial coordinates of surrounding atoms and requires the choice of a weighting function

$$\rho_i^{emb} = \sum_{j \neq i} w(r^{ij}) + w(0) \ldots\ldots.(1.13$$

Here, $w(0)$ is the local embedding density of a solitary atom. The (effectively many-body) model potentials introduced above serve to model a variety of metal properties.

The potential contributions to the pressure tensor and the elastic moduli can be obtained from the terms of first and second-order in the expansion of the configurational free energy with respect to the Lagrangian strain tensor $S_{\mu\nu}$ defined through particle displacement written as $r_\nu^i \to r_\nu^i + r_\mu^i S_{\mu\nu}$ .The Greek subscripts μ, ν stand for Cartesian components associated with the x, y, z directions. This expansion is obtained from the standard expression for the configurational Helmholtz free energy $\beta F^{pot} = -\ln \int exp(-\beta E) dr^N$ with $\beta = 1/(k_B T)$.

For the binary potential function *U* a radially symmetric short ranged attractive (SHRAT) potential is used [26, 27]

$$U(r) = \phi_0 \psi^{-4} \left[3\left(r_{cut} - r\right)^4 - \left(r_{cut} - r_{\min}\right)\left(r_{cut} - r\right)^3 \right] \ldots\ldots.(1.14$$

for $r \le r_{cut}$ and $U(r) = 0$ other wise, with an energy scale ϕ_0, length scale ϕ_0 an interaction range $r_{\min}$, and cutoff radius r_{cut}. The well depth of the two-particle (binary interaction) potential U is $-U(r_{\min}) = \phi_0 \psi^{-4} \left(r_{cut} - r_{\min}\right)^4$. The SHRAT Potential has a finite value at r =0, i.e. $-U(r_{\min}) = \phi_0 \psi^{-4} r_{cut}^3 \left(4r_{\min} - r_{cut}\right)$. For temperatures below $0.1\phi_0 / k_B$ - due to the Boltzmann factor $\exp\left[-U(0)/k_B T\right]$ - the fraction of particles that reach zero distance is smaller than 10^{-51} for the choice of $r_{cut} = 1.6\psi$, $r_{\min} = 2^{1/6}\psi$.

The normalized Lucy's weight function in the definition of the embedding density is chosen[28]

$$w(r) = w_0 \left(1 + 3\frac{r}{r_{cut}}\right)\left(1 - \frac{r}{r_{cut}}\right)^3$$

for $r \le r_{cut}$ and $w(r) = 0$ other wise, with a pre-factor obtained by normalizing the weight function, $w_0 = w(0) = 105/(16\pi r_{cut}^3)$. (See fig 1.2).

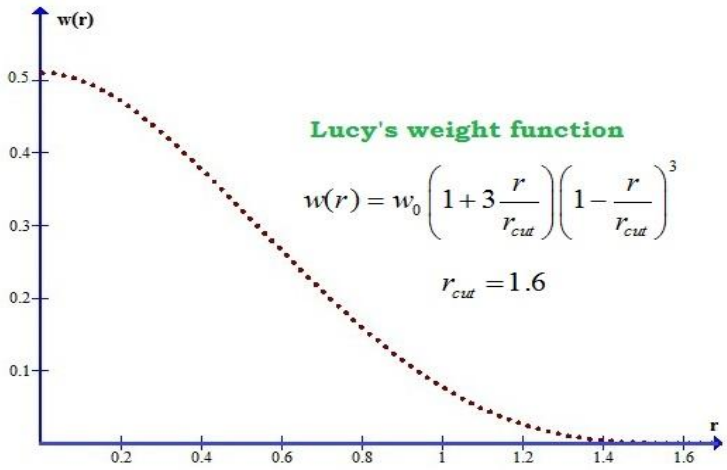

Fig 1.2 Lucy's weight function

The embedding potential in polynomial form is

$$\Theta(\rho^{emb}) = \phi_0 \sum_{k=2,4,...} \alpha_k \left[\left(\rho^{emb} - \rho_{des}^{emb} \right)^k - \left(w_0 - \rho_{des}^{emb} \right)^k \right] r_0^{3k} \quad \text{.....(1.16}$$

where ρ_{des}^{emb} is the desired embedding number density and α_k are the embedding strengths being part of the model. Odd terms in the sum are excluded since their contribution would be always repulsive in nature; the linear term (k=1) could be adsorbed in a modified pair potential U. The desired density in the model equals roughly $\rho_{des}^{emb} = \psi^{-3}$ the embedding density and particle number density $n \equiv N / V = \psi^{-3}$. The polynomial format of the embedding functional is computationally less expensive than the standard logarithmic form. Also, the ratio between cohesive energy E_{coh} (or energy per particle) and Bulk modulus can be systematically changed without influence on values of other constitutive properties of the system.

The components of force acting on particle i, directly obtained by differentiating the potential energy equation, are

$$F_\nu^i = -\sum_{i \neq j} \left[\nabla_\nu U(r)\big|_{ij} + \left(\frac{\partial \Theta(\rho^{emb})}{\partial \rho^{emb}}\bigg|_i + \frac{\partial \Theta(\rho^{emb})}{\partial \rho^{emb}}\bigg|_j \right) \nabla_\nu w(r)\big|_{ij} \right] \text{.....(1.17}$$

The Greek subscript ν stands for Cartesian components associated with the x, y, z directions.

Material	Packing	$\frac{r_c}{1.6}$	$\frac{r_m}{2^{1/6}}$	α_2	Mass/atom 'kg'
Cu	FCC	1.010	1.00	0.42	1.06E-25
Ag	FCC	1.006	1.00	0.70	1.790 E-25
Ni	FCC	1.017	1.02	0.20	9.75E-26

Table 1.1 GEAM Parameters for various metals.

1.3 Solving the equation of motion

1.3.1 Periodic boundary conditions

The presence of hard walls for the container of volume V would introduce large surface effects that would dominate the behavior of the fluid and obscure the bulk fluid behavior. Periodic Boundary Conditions (PBC) are used to avoid such surface effects. The PBC assumes that the primary cell is duplicated in all spatial direction, each replicated or "image" cell contains the same number of molecules having the same positions, velocities, etc. Molecules are free to move between adjacent cells so that conservation of number of particles "N" and energy "E" is maintained within primary cell and each of its images. In a three dimensional system of N particles in the primary cell has 26 images, see fig 1.3.

The key point is that each particle *i* in the cell should be thought as interacting not only with other particles j in the box, but also with their images in nearby boxes. Interactions can go through box boundaries.

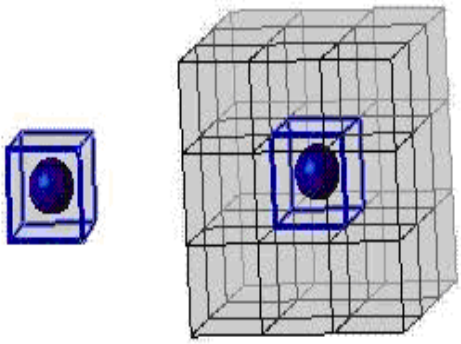

Figure 1.3 Periodic Boundary Conditions, primary cell has 26 images

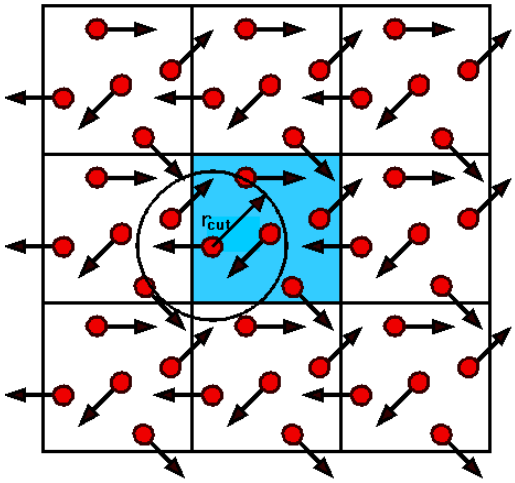

Figure 1.4 Periodic Boundary Conditions

PBC are applied by the transformation

$$x'_i = \begin{cases} x_i & \text{if} \quad 0 \le x_i \le L_x \\ x_i + L_x & \text{if} \quad x_i < 0 \\ x_i - L_x & \text{if} \quad x_i < L_x \end{cases} \qquad (1.18$$

L_x: cell length in x direction, same criterion can be applied to y and z directions.

1.3.2 Minimum image criterion

The minimum image convention is a procedure where one takes the nearest neighbor to an actual particle, regardless of whether this neighbor is an actual particle or an image particle. When using PBC the distance r_{ij} may be between particles *i* and *j* in the primary cell or between i and any of the images of j. In the case of relatively short range LJ potential it's sufficient to use only the one ij interaction that corresponding to the shortest of the 27 possible r_{ij} distance, see fig 1.5 and fig 1.6.

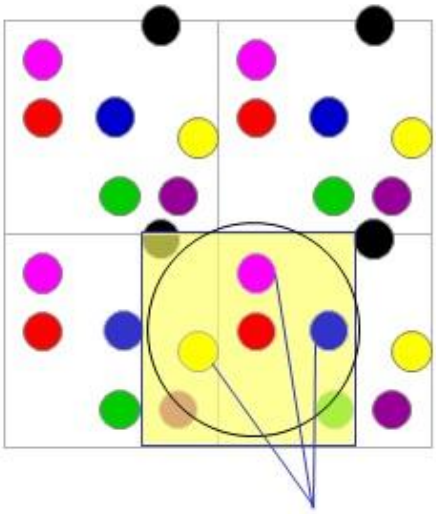

Only interactions considered

Figure 1.5 Minimum image criterion

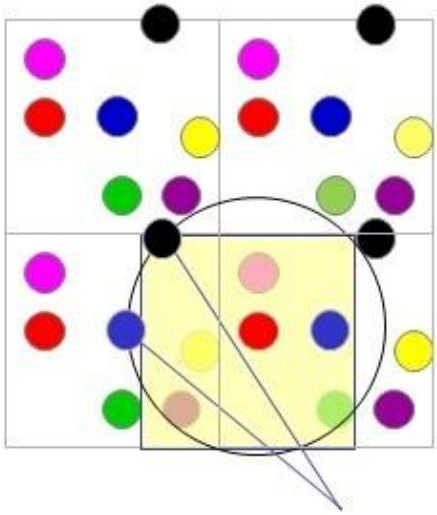

These two are same distance from central atom, yet: Black atom interacts blue atom does not

Figure 1.6 Minimum image criterion

1.3.3 Gears predictor corrector algorithm

Predictor Corrector Methods are composed of three steps: prediction, evaluation and correction.

Predict molecular positions and their derivatives at time t+Δt, using Taylor series expansion.

$$R^p(t+\Delta t) = R(t) + R1(t) + R2(t) + R3(t) + R4(t) + R5(t) \quad \ldots\ldots (1.19a$$

$$R1^p(t+\Delta t) = R1(t) + 2R2(t) + 3R3(t) + 4R4(t) + 5R5(t) \quad \ldots\ldots (1.19b$$

$$R2^p(t+\Delta t) = R2(t) + 3R3(t) + 6R4(t) + 10R5(t) \quad \ldots\ldots (1.19c$$

$$R3^p(t+\Delta t) = R3(t) + 4R4(t) + 10R5(t) \quad \ldots\ldots (1.19d$$

$$R4^{p}(t+\Delta t) = R4(t) + 5R5(t) \quad \ldots\ldots (1.19e$$

$$R5^{p}(t+\Delta t) = R5(t) \quad \ldots\ldots (1.19f$$

Where $R(t) = r_i$; $R1(t) = r_i' \ \Delta t$; $R2(t) = r_i'' \ (\Delta t)^2 / 2!$; $R3(t) = r_i''' \ (\Delta t)^3 / 3!$; $R4(t) = r_i^{(iv)} (\Delta t)^4 / 4!$,

$R5(t) = r_i^{(v)} (\Delta t)^5 / 5!$

Evaluate the intermolecular force F_i on each molecule at time t+Δt using the predicted positions.

$$F_i = -\nabla_{r_i} U(r_1, r_2, r_3 .... r_N) \ldots\ldots\ldots\ldots (1.1$$

$$F(r_{ij}) = -F(r_{ji}) \ \ldots\ldots\ldots\ldots (1.20$$

With the forces at $(t+\Delta t)$ from the above, Newton's second law can be used to determine the acceleration $r_i''(t+\Delta t)$, an error term is then formed from these accelerations and those predicted previously.

$\Delta r_i'' = [r_i''(t+\Delta t) - r_i''^{\,p}(t+\Delta t)]$ Or

$$\Delta R2 = \Delta r_i'' \ (\Delta t)^2 / 2! \ \ldots\ldots\ldots (1.21$$

Correct the predicted positions and their derivatives using the discrepancy $\Delta r_i''$ between the predicted acceleration and that given by evaluated force F_i, then corrected

$$R^{c}(t+\Delta t) = R^{p}(t) + R1^{p}(t) + R2^{p}(t) + R3^{p}(t) + R4^{p}(t) + R5^{p}(t) + \tfrac{3}{16}\Delta R2 \ \ldots\ldots\ldots (1.22a$$

$$R1^c(t+\Delta t) = R1^p(t) + 2R2^p(t) + 3R3^p(t) + 4R4^p(t) + 5R5^p(t) + \tfrac{251}{360}\Delta R2 \quad \ldots\ldots\ldots \text{(1.22b}$$

$$R2^c(t+\Delta t) = R2^p(t) + 3R3^p(t) + 6R4^p(t) + 10R5^p(t) + \Delta R2 \quad \ldots\ldots\ldots \text{(1.22c}$$

$$R3^c(t+\Delta t) = (t)R3^p(t) + 4R4^p(t) + 10R5^p(t) + \tfrac{11}{18}\Delta R2 \quad \ldots\ldots\ldots \text{(1.22d}$$

$$R4^c(t+\Delta t) = R4^p(t) + 5R5^p(t) + \tfrac{1}{6}\Delta R2 \quad \ldots\ldots\ldots \text{(1.22e}$$

$$R5^c(t+\Delta t) = R5^p(t) + \tfrac{1}{60}\Delta R2 \quad \ldots\ldots\ldots \text{(1.22f}$$

Where $R(t) = r_i$; $R1(t) = r_i'\ \Delta t$; $R2(t) = r_i''\ (\Delta t)^2/2!$; $R3(t) = r_i'''\ (\Delta t)^3/3!$; $R4(t) = r_i^{(iv)}(\Delta t)^4/4!$,

$R5(t) = r_i^{(v)}(\Delta t)^5/5!$

1.4 System of units

Simulation programs are conventionally written so that all quantities are dimensionless. As units of distance and energy we use the potential parameters ψ and ϕ_0, respectively, and as the unit of mass, that of one atom. The unitless (or reduced) forms for quantities are indicated by an asterisk. The reduced form of SHRAT potential becomes:

$$U^*(r) = \frac{512}{27}\left(1-r^*\right)\left(3-2r^*\right)^3 \quad \ldots\ldots\ldots \text{(1.23}$$

Where $U^* = U/\phi_0, r^* = r/\psi$.

1.4.1 Fundamental quantities

Mass m = mass of one atom

Length ψ

Energy ϕ_0

Time $t = \psi\sqrt{m/\phi_0}$

1.4.2 Derived quantities

Density $\rho^* = \rho\psi^3/m$

Force $F^* = F\psi/\phi_0$

Pressure $P^* = \mathrm{P}\psi^3/\phi_0$

Temperature $T^* = k_B T/\phi_0$ where $k_B = 1.38065 \times 10^{-23} \frac{\mathrm{m^2 kg}}{\mathrm{s^2 K}}$ is the Boltzmann Constant

Velocity $v^* = v\sqrt{m/\phi_0}$

Typical unit values for argon are show below in table 1.2

Length ψ (m)	Energy ϕ_0 (J)	Mass m (kg)	Time t(s)	Velocity v (m/s)	Force F (N)	Pressure P ($N.m^{-2}$)	Temperature T (k)
4.405×10^{-10}	1.65×10^{-21}	6.69×10^{-26}	2.17×10^{-12}	1.57×10^{2}	4.85×10^{-12}	4.20×10^{7}	120

Table 1.2 Physical quantity unit values for Argon

1.4.3 Reference values

The determined model parameters and reference values are not unique in the sense that it is possible to find similar sets which would as well resemble the properties of real materials. In following, reference values used to translate between dimensionless simulation quantities and experimental values of real materials. Any measurable quantity Q with a dimension [Q] specified in SI units kg, m, and s is made dimensionless by a reference quantity

$Q_{ref} = m^{\alpha+\gamma/2}\psi^{\beta+\gamma}\phi_0^{-\gamma/2}$ *for* [Q]=$kg^{\alpha}m^{\beta}s^{\gamma}$ ……(1.24

such that $Q = Q_{\text{dimless}}Q_{ref}$; quantities m; m, ψ and ϕ_0 provide the scales via the interaction potential Eq. (1.14) and the equations of motion. The reference values for length r, number density n, energy k_BT, temperature T, time t, pressure P, and the elastic moduli in terms of the simulation parameters are therefore $r_{ref} = \psi$, $n_{ref} = \psi^{-3}$, $\phi_0 = k_BT_{ref}$, $t_{ref} = \psi(m/\phi_0)^{1/2}$ and $P_{ref} = \phi_0\psi^{-3}$

for Ni, e.g., one obtains reference values $\phi_0 = 7.13\text{x}10^{-21}\text{J}$, $\psi = 2.28\,A^o$ and $n_{ref} = 84.6\,nm^{-3}$. $P_{ref} = 0.60\text{Gpa}$, atomic mass of Nickel $m_{Ni} = 9.76\text{x}10^{-26}\,\text{kg}$ and the reference time is estimated as $t_{ref} = 8.44\text{x}10^{-13}$ s.

1.5 Evaluation of physical properties

Measuring quantities in molecular dynamics usually means performing time averages of physical properties over the system trajectory. Physical properties are usually functions of the particle position vector and its derivative. So, for instance one can define the instantaneous value of a generic physical property A at time t:

$$A(t) = f(r_1(t),...,r_N(t),v_1(t),...,v_N(t)) \quad \text{..... (1.25}$$

and then obtain its average.

$$\langle A \rangle = \frac{1}{N_T} \sum_{t}^{N_T} A(t) \quad \text{..... (1.26}$$

where t in an index which runs over the time steps from 1 to the total number of time steps N_T .

Local properties can be evaluated by summing trajectories of the particles in each bin and averaging over the bin volume or the corresponding number of particle depending on the quantity that is computed.

1.5.1 Stress Tensor and Elastic constants

The total pressure tensor is a sum of kinetic and potential contributions. The potential part of the pressure is evaluated as a N-particle average according to [28]:

$$Vp_{\mu\nu}^{pot} = \langle \Phi_{\mu\nu} \rangle, \Phi_{\mu\nu} = \sum_{i \neq j} \phi_{\mu\nu}^{i}(\mathrm{r}^{ij}) \quad \text{..... (1.27}$$

Where $\sum_{i \neq j}$ denotes a double summation over pairs *ij* of (different) particles, the angular brackets indicate an ensemble or time average and the second rank tensor $\phi^i (i \in 1, ..., N)$ is given by

$$\phi^i_{\mu\nu}(\mathrm{r}^{ij}) = r^{ij}_{\mu}\left(\tfrac{1}{2}\nabla_{\nu} U(\mathrm{r}^{ij}) + \left.\frac{\partial F(\rho^{emb})}{\partial \rho^{emb}}\right|_i \nabla_{\nu} w(\mathrm{r}^{ij}) \right) \ldots\ldots\ldots \quad (1.28$$

$\nabla_{\nu} w(\mathrm{r}^{ij}) = r^{-1} r_{\nu} \partial w(r)/\partial r$ as for any function with spherical symmetry, i.e., when $w(\mathrm{r}) = w(r)$.

The kinetic part of the pressure p^{kin} obtained from peculiar velocity of particles,

$\mathrm{c}^i = \dot{\mathrm{r}}^i - \mathrm{v}(\mathrm{r}^i)$, where $\mathrm{v}(\mathrm{r}^i)$ denotes the (macroscopic) flow velocity on position of particle

$$Vp^{kin}_{\mu\nu} = \left\langle \sum_i m c^i_{\mu} c^i_{\nu} \right\rangle \ldots\ldots\ldots \quad (1.29$$

The scalar (isotropic) pressure p^{iso} is the trace of the total pressure tensor divided by the spatial dimension $p^{iso} = p_{\mu\mu}/3 =$. The symmetric traceless part of p^{iso} is associated with the shear stress and normal stress differences. The antisymmetric part of the pressure tensor vanishes for structure-less particles with spherical interaction.

The response of the material to deformation $s_{\mu\nu}$ is characterized by the elastic modulus tensor $G_{\lambda\kappa,\mu\nu}$ defined by linear relation $\sigma_{\lambda\kappa} = G_{\lambda\kappa,\mu\nu} s_{\mu\nu}$ · where $\sigma_{\lambda\kappa} = -(p^{pot,def}_{\lambda\kappa} - p^{pot,0}_{\lambda\kappa})$ is the negative difference between the potential contribution to the pressure tensor in the deformed state $p^{pot,def}_{\lambda\kappa}$ and its corresponding value $p^{pot,0}_{\lambda\kappa}$ in the un-deformed state.

$$VG_{\lambda\kappa,\mu\nu} = \left\langle \sum_{i\neq j} \phi^{i}_{\lambda\kappa,\mu\nu}(\mathrm{r}^{ij}) \right\rangle_0 + \tfrac{1}{3}\left\langle \Phi_{\mu\mu} \right\rangle_0 \delta_{\lambda\kappa}\delta_{\mu\nu} \quad \ldots\ldots\ldots \quad (1.30$$

The abbreviation is used $\phi^{i}_{\lambda\kappa,\mu\nu}(\mathrm{r}) = r_\lambda \nabla_\kappa \phi^{i}_{\mu\nu}(\mathrm{r})$. The subscript "0" in $\langle ....\rangle_0$ indicates a configurational average to be evaluated in the unstrained state. In the conventional "Voigt notation" the four indices (range 1-3) are replaced by two indices (range 1-6).

In this notation one denotes elastic moduli of cubic crystals and of the model with central interactions: $C_{11} = G_{xx,xx}, C_{12} = G_{xx,yy}$, and $C_{44} = G_{xy,xy}$. The conventional symmetrization according to $C_{44} = \left(G_{yx,yx} + G_{yx,xy} + G_{xy,yx} + G_{xy,xy}\right)/4$ is not essential In this case.

In this work, the axes x, y, z correspond to the directions [100], [010], [001] in the cubic crystal, i.e., to the deformation direction, its gradient direction and the direction normal to the shear deformation plane, respectively. In systems with cubic symmetry, spatial anisotropy is reflected by the existence of a minimum and a maximum of the shear modulus. The modulus C_{44} is associated with a displacement in the [100] direction and a (010) shear plane in a cubic crystal. This modulus stands for a maximum resistance the system with FCC structure can offer to shear. The same systems, with a displacement applied along the [110] direction and the (111) shear plane of the crystal, have minimum shear modulus associated with the modulus $\tilde{C}_{44} = (C_{11} - C_{12})/2$. For an isotropic system, C44 equals the orientationally averaged shear modulus G. As a component of the elastic modulus tensor, the shear modulus can be written

as $G \equiv \dfrac{3C_{44} + 2\tilde{C}_{44}}{5}$.

The response to a volume changing deformation of an isotropic solid can be inferred from the (isothermal) bulk modulus or compression modulus $B = n(\partial p^{iso,pot} / \partial n)_T$, where n = N/V is number density. The bulk and shear moduli are related in cubic crystals via a modified Cauchy relation valid for the embedded-atom method of the form Eq.(1.12) through

$$B = \tfrac{5}{3}G + 2p^{pot} + \frac{1}{9V}\left\langle \sum_i \frac{\partial^2 F}{\partial \rho^2}\bigg|_i \left(\sum_{j\neq i} r^{ij} \frac{\partial w}{\partial r}\bigg|_{ij} \right)^2 \right\rangle_0 \quad \ldots\ldots\ldots (1.31$$

1.5.2 Temperature

The temperature T is directly related to the kinetic energy by the well-known equi-partition formula, assigning an average kinetic K(t) energy k_BT/2 per degree of freedom:

$$K(t) = \tfrac{3}{2} N k_B T(t) \quad \ldots\ldots\ldots (1.32$$

Where: $K(t) = \sum_{i=1}^{N} \left(\frac{1}{2} m_i (\dot{\mathbf{r}}_\mathbf{i} - \mathbf{v}_\mathbf{i})^2 \right)$, $\mathbf{v}_i$ denotes the (macroscopic) flow velocity on position of particle and $\dot{\mathbf{r}}_\mathbf{i}$ the velocity vector of atom *i*.

1.5.3 Average velocity 'flow velocity'

Sum of the velocity of particles over their number

$$\bar{v} = \sum_i v_i / N \quad \ldots\ldots\ldots (1.33$$

The average can be made for the total velocity or one or more of its components.

1.5.4 Density

Number of particles per unit volume

$$\rho = N / V \quad \ldots\ldots\ldots \quad (1.34$$

1.5.5 Heat Flux

The instantaneous heat flux in a given direction, is evaluated from the energy associated with each atom in the simulation

$$\mathbf{q} = \frac{d}{dt}\frac{1}{V}\sum_{i=1}^{N}\mathbf{r}_i E_i \quad \ldots\ldots\ldots \quad (1.35$$

Where $\mathbf{q}$ is the heat flux vector, $\mathbf{r}_i$ the position vector of atom i and E_i the energy associated with atom i, and the sum is over all N atoms. The energy associated with each atom is the sum of its kinetic energy and potential energy [32]

$$E_i = \sum_{j=1}^{N}\left(\frac{1}{2}U(r_{ij}) + \frac{1}{2}m_i(\dot{\mathbf{r}}_\mathbf{i} - \mathbf{v}_\mathbf{i})^2\right) \quad \ldots\ldots\ldots \quad (1.36$$

where m_i is the mass of atom i, $\mathbf{v}_i$ denotes the (macroscopic) flow velocity on position of particle, $\dot{\mathbf{r}}_\mathbf{i}$ the velocity vector of atom i, and $U(r_{ij})$ the pair-wise interaction between atoms i and j when separated by a distance r_{ij}. Substituting into the above equation we get

$$\mathbf{q} = \frac{1}{V}\left[\sum_{i=1}^{N}\dot{\mathbf{r}}_\mathbf{i} E_i + \frac{1}{2}\sum_{i=1}^{N}\sum_{i\neq j}^{N}\mathbf{r}_{ij}(\mathbf{F}_i \bullet (\dot{\mathbf{r}}_\mathbf{i} - \mathbf{v}_\mathbf{i}))\right] \quad \ldots\ldots\ldots \quad (1.37$$

Where $\mathbf{r}_{ij}=\mathbf{r}_i-\mathbf{r}_j$ and $\mathbf{F}_{ij}$ is the force exerted on atom *i* by atom *j*. The first term within the square brackets is related to convection and the second to conduction.

However, solid particles with embedded atom interaction will have also embedding energy that needs to be added when calculating the heat flux in the solid structure.

1.5.6 Impulse

Impulse is the integral of a force with respect to time. When a force is applied to a rigid body it changes the momentum of that body. A small force applied for a long time can produce the same momentum change as a large force applied briefly, because it is the product of the force and the time for which it is applied that is important. The impulse is equal to the change of momentum.

$$I=\int_0^t F d\tilde{t}=\int_0^t \sigma A d\tilde{t} \quad \ldots.(1.38$$

Numerical integration is done using the trapezoidal rule. It works by approximating the function g(x) is by a linear function, see fig 1.17. Integration is then performed by calculating the area under the linear curve, hence:

$$\int_a^b g(x)dx=(b-a)\left(\frac{g(a)+g(b)}{2}\right)\ldots.(1.39$$

The domain is discretized into "N" equally spaced panels, or "N+1" grid points (1, 2, ..., N+1), where the grid spacing is "Δ=(b-a)/N", the approximation to the integral becomes

$$\int_a^b g(x)dx\approx\frac{\Delta}{2}\sum_{k=1}^{N} g(x_k)+g(x_{k+1})=\frac{b-a}{2N}\left(g(x_1)+2g(x_2)+2g(x_3)....+2g(x_{N-1})+g(x_N)\right)\ldots.(1.40$$

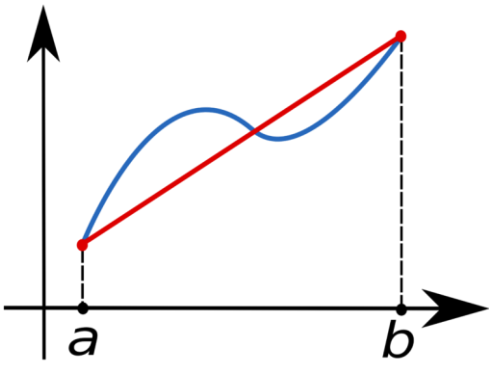

Fig 1.7 An arbitrary function g(x) is approximated by linear function.

1.5.7 Strain

A strain is a normalized measure of deformation representing the displacement between particles in the body relative to a reference length.

A general deformation of a body can be expressed in the form $x = g(x_0)$ where x_0 is the reference position of material points in the body. Such a measure does not distinguish between rigid body motions and changes in shape (and size) of the body. A deformation has units of length.

$$\zeta = \frac{\partial}{\partial x_0}(x - x_0) = \frac{\partial x}{\partial x_0} - 1 = \frac{\partial g(x)}{\partial x_0} - 1 \ldots\ldots \text{(1.41}$$

Chapter Two

Dynamics of Shock Waves Impacting Solid Wall

The basic idea is to simulate a piston driven shock wave as in the schematic diagram as shown in fig 2.2. The piston is given a constant speed impulsively and moves into a region containing gas particles; as a result, a shock wave is formed and propagated in the gas channel. In such simulation we note the following:

1. The initial number of particles in the unit remains constant throughout the simulation till the shock nears. This gives a constant value of the density in the upstream region and hence the upstream mean free path is also a constant value. The constant value of density in the upstream regions is an important feature for various purposes. One can only show a profile of the density as a ratio of a local density to the upstream density for a comparison purpose and the constant upstream density makes analysis simpler and clear.
2. The system is deterministic at all times and naturally evolves from the uniform initial configuration of particles to a shock profile.
3. The simulation of a piston driven shock wave closely resembles the corresponding physical experiment, even though assumptions are made on the nature of interactions among particles, and between particles and computational boundaries.
4. The shock can be monitored as it develops and if there is a sufficient distance between the shock wave and piston at the time of reflection, the shock reflection phenomena can also be studied in details.

2.1 Faced Centered Cubic ‘FCC’ structure

Atoms in solids at room temperature are almost completely lacking mobility. Their thermal motion is reduced to the vibrations about an equilibrium position and individual atoms can move from their positions only with great difficulty.

In metals valence electrons are not localized around nuclei. The dislocation of electrons from nuclei yields the strong decrease of kinetic energy and subsequently the increase of the binding energy in the metals. The interaction between atoms in metals is strong but depends little or not at all on the direction. Thus, metals tend to form one of the three densely packed structures (Faced Centered cubic ‘FCC’, Body Centered ‘BBC’ or Hexagonal Close Packed ‘HCP’).

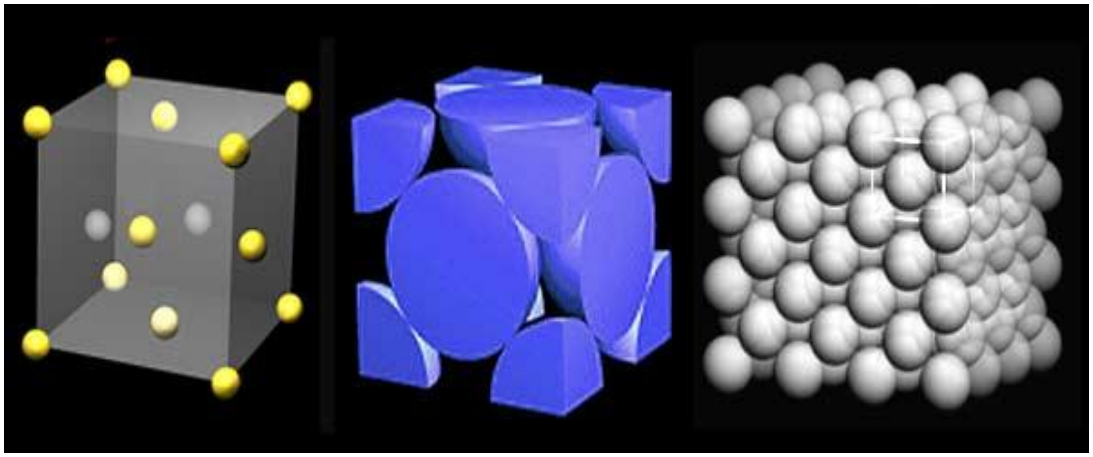

Figure 2.1 FCC structure

The face centered cubic structure shown in fig 2.1 has atoms located at each of the corners and the centers of all the cubic faces (left image above). Each of the corner atoms is the corner of another cube so the corner atoms are shared among eight unit cells. Additionally, each of its six face centered atoms is shared with an adjacent cell. Since 12 of its atoms are shared, it is said to have a coordination number of 12. The FCC unit cell consists of a net total of four atoms; eight

eighths from corners atoms and six halves of the face atoms as shown in the middle image above. The image below highlights a unit cell in a larger section of the lattice.

In the FCC structure the atoms can pack closer together than they can in the BCC structure. The atoms from one layer nest themselves in the empty space between the atoms of the adjacent layer. To picture packing arrangement, imagine a box filled with a layer of balls that are aligned in columns and rows. When a few additional balls are tossed in the box, they will not balance directly on top of the balls in the first layer but instead will come to rest in the pocket created between four balls of the bottom layer. As more balls are added they will pack together to fill up all the pockets. The packing factor (the volume of atoms in a cell per the total volume of a cell) is 0.74 for FCC crystals. Some of the metals that have the FCC structure include aluminum, copper, gold, iridium, lead, nickel, platinum and silver.

2.2 Shock tube model setup

Figure shows the computational domain schematically. The size of the domain is $L_x \text{ x } L_y \text{ x } L_z$ = $29\psi_w$ x $133.70\psi_w$ x $29\psi_w$. To left side of the domain (in y–direction) a wall that is formed of a two layers of a cubic face centered lattice (lattice size, a = $3.22\psi_w$, 2592 molecules) of nickel molecules. The domain is $29\psi_w$ high and deep. Another wall is placed at the right end of the domain; it consists of 12960 molecules of Nickel molecules that occupy an axial length of 16.10 ψ_w. The volume between the two walls ($L_{y,\,fluid}$ =$107.93\psi_w$) is filled with 2708 argon molecules. Moreover, at the far end of the solid wall, another solid wall ‘Holding wall’ is formed of two layers of a cubic face centered lattice (lattice size, a = $3.22\psi_w$, 2592 atoms) of Nickel molecules. Another identical wall ‘Ghost Wall’ is also formed to the left of the solid wall.

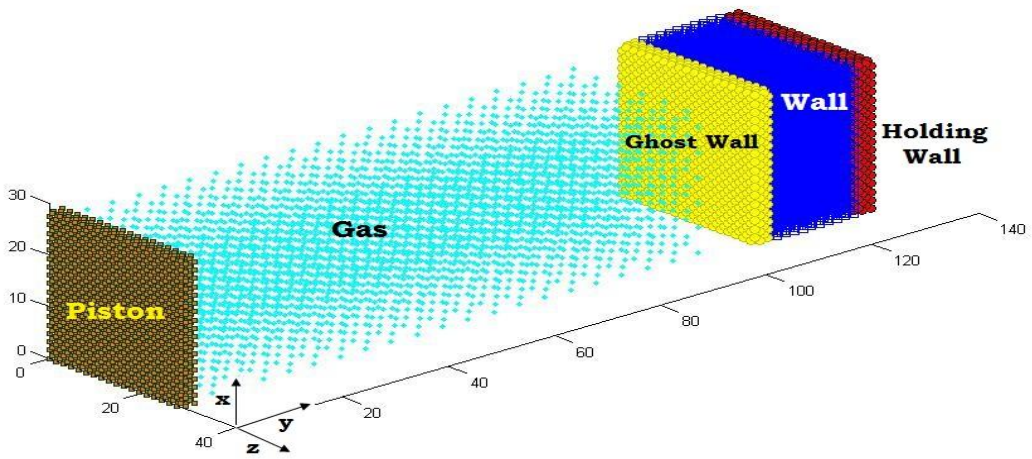

Fig 2.2 Schematic view of atomistic shock model

Solid particles interact according to the Generic Embedded Atom Method 'GEAM' Potential. The gas particles, gas-solid particles, solid-holding wall particles and piston-gas particles are interacting according to the Short Range Attractive Potential 'SHRAT'. The piston particles and the holding wall particles are tethered to lattice location with elastic springs and they also allowed to interact with each other according to 'SHRAT' potential. Periodic Boundary conditions are only applied in the transverse directions.

In MD calculations, the interaction depends on the neighboring molecules. In a cubic system surface effect is reduced (or eliminated) by applying Periodic Boundary Conditions 'PBC' in all three directions, each molecule will always have -on average- the same number of neighboring molecules as every other molecule. Once periodicity is not applied in one or more directions surface effect appears and molecules closer to the surface without PBC will have fewer neighbors than those further, hence less interaction takes place at the surface and calculation of

force, energy and all every other quantity will be affected due to the loss of periodicity in one or more direction.

Holding wall particles and ghost particles are introduced to overcome this problem. Ghost particles are adjacent to the solid wall from the wet side (i.e. the near side of the gas channel) and they only interact with particles of interest (solid wall in this case), the calculation of the embedding density function and its derivative is better computed and accordingly force, energy , elastic constants and all other properties. Ghost particles are also very important when it comes to simulate porous media, where they will fill up the gaps and interact with the solid particles. Rigidity and stiffness of solids will be maintained by introducing ghost particles to the system, moreover the total number of the solid structure 'solid particle, ghost particles and holding wall particles' will remain the same regardless of the value of porosity.

The holding wall is introduced to better calculate the embedding density function and its derivatives and to limit the solid wall motion in the normal direction. The holding wall particles are adjacent to the solid wall from the far side of the gas channel. The holding wall particles will show up in the embedding density calculations and will interact with the solid wall particles according to SHRAT potential and they will not interact with any other particles in the system.

2.3 Simulation details

2.3.1 Selection of time step

Two simulation cases with same initial conditions were performed but with two different values of time step: in the first case $\Delta t=0.005$ and in the second case $\Delta t=0.0025$. The physical properties were averaged every 100 time steps in the first case and every 200 time steps in the second case, i.e. properties were averaged over the same time duration of 0.5 time units in both cases.

Fig 2.3 shows pressure profiles in the gas flow domain generated by the propagating shock wave at various times in these cases with the two different time steps. The pressure profiles were plotted at the same times in both cases and the pressure values are in a very good agreement. Eventually the time step was set to 0.005, a value which will reduce the simulation time by half and will have no effect on the computed results.

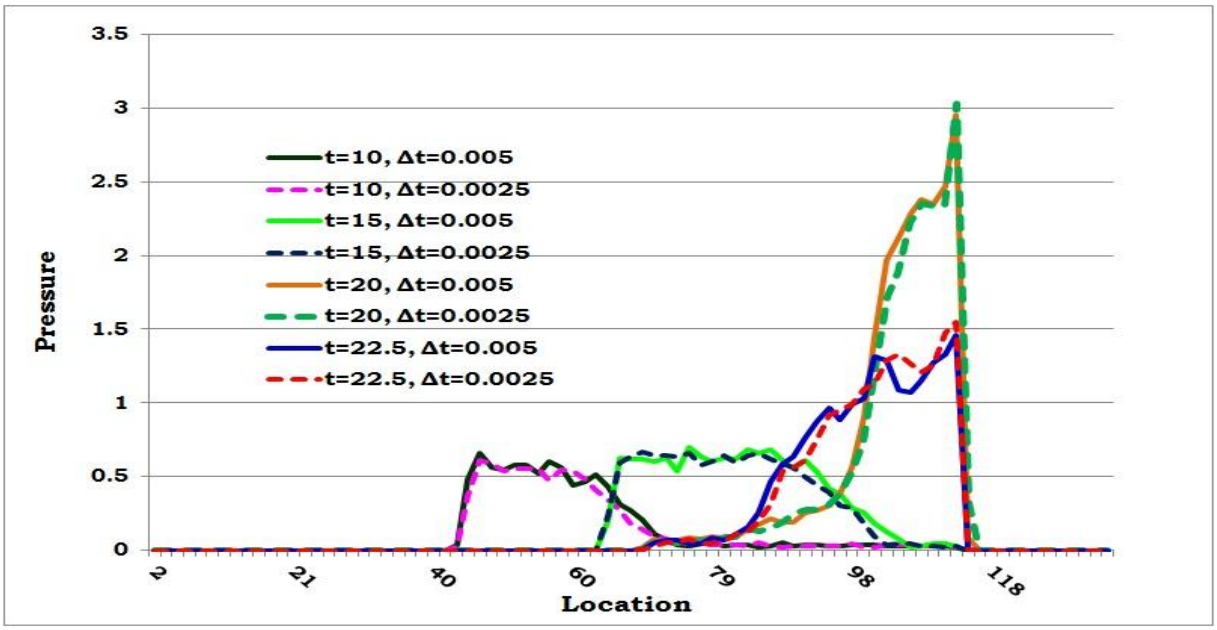

2.3 Pressure profiles in the gas flow domain generated by the propagating shock wave at various times at two different time steps.

2.3.2 System equilibration

The fluid molecules are placed initially with FCC structure within the fluid volume of the domain. The time step is set to 0.005 and a cut–off radius of $r_c = 1.5\psi_g$ or (ψ_{gw}) for all interactions except the solid-solid EAM interaction where it requires a cut-off radius of $1.6\psi_w$. The cut–off radius is enforced with respect to the individual atom distances. The system is then equilibrated for 10,000 time steps. Velocities and momentum are rescaled every 20 time steps to correspond to the desired temperature. At the end of the equilibration phase, the system state is

saved. Quantities can be locally computed by subdividing the computation domain into 2D cells ‘bins’ in the Y-X plane; the bins fill the sample “computational domain” without gaps and overlaps, see fig 2.4. Each cell has a size of = $1.61\psi_w$ ‘or one layer of a cubic face centered lattice’. Local properties can be evaluated by summing trajectories of the particles in each bin and averaging over the bin volume or the corresponding number of particles depending on the quantity that is computed.

One dimensional properties are computed by averaging over the cells in transverse-direction; consequently, the 2D cell configuration is reduced to one dimensional vertical slabs.

Fig 2.4 Channel 2d bins

During equilibration, properties were averaged every 500 time steps. After 10000 time steps steady state is reached and properties of both solid and gas are not significantly changed. Gas molecules are spreading over the whole gas channel and solid wall particles reached their equilibrium positions which are not significantly different from their initial position. The embedding density ‘glue’ kept these particles arranged in layers of the FCC lattice structure, besides, the glue limit the solid molecules motion to a vibrational motion around their equilibrium positions. Solid properties are presented by averaging over the whole solid wall length or locally slab by slab. One should note that there are 10 slabs containing the whole solid structure: first slab closest to the gas channel and last slab (10^{th} slab) closest to the holding wall.

2.4 Shock wave formation

After equilibration, another run was performed in which piston particles were allowed to accelerate. Once they reached the desired 'prescribed' velocity, the piston starts moving suddenly which results in compression of the gas particles and forming the shock wave that moves towards the solid wall. The shock wave is then propagated in the gas channel at speed greater than the piston speed, the shock span 'distance between shock front and the piston' is getting greater as the simulation time increases and the shock speed increases as it passes through the gas molecules.

The motion of the piston is stopped once the shock wave hits the solid wall, while the simulation was continued and shock wave reflection was observed. Properties in both solid and gas regions were averaged locally over the cell size every 100 time steps. These properties were stored in a separate file for post-processing. Shock thickness based on the maximum density gradient is defined as $\Lambda = (\rho_1 - \rho_0) / (\partial\rho / \partial y|_{\max})$. The shock width is calculated from the gradient of the normalized density profile and $\Delta\rho = \rho_1 - \rho_0$, denotes the density jump across the shock. The denominator is the largest spatial density gradient within the shock waves. Thus, Λ represents the distance over which the maximum gradient would have to be maintained in order to achieve the same density jump.

Over this short distance, the fluid state changes significantly so that it is immediately obvious that the continuum hypothesis is not applicable within the shock.

Fig. 2.4 shows a particular example for a shock in argon.

All quantities have been non-dimensionalized by the pre- and post-shock properties,

$$\tilde{\beta} = \frac{\beta - \beta_0}{\beta_1 - \beta_0}$$

where the subscripts 0 and 1 denote the pre- and post-shock state, respectively.

β could refer to the density, velocity, temperature, pressure, etc. Hence, zero corresponds to the pre-shock state and unity is the post-shock value.

An 8th order polynomial was used to interpolate the normalized data of temperature, pressure, velocity and density and plotted in fig 2.5; moreover, the maximum density gradient was found by differentiating the density plot formed by the corresponding interpolating polynomial.

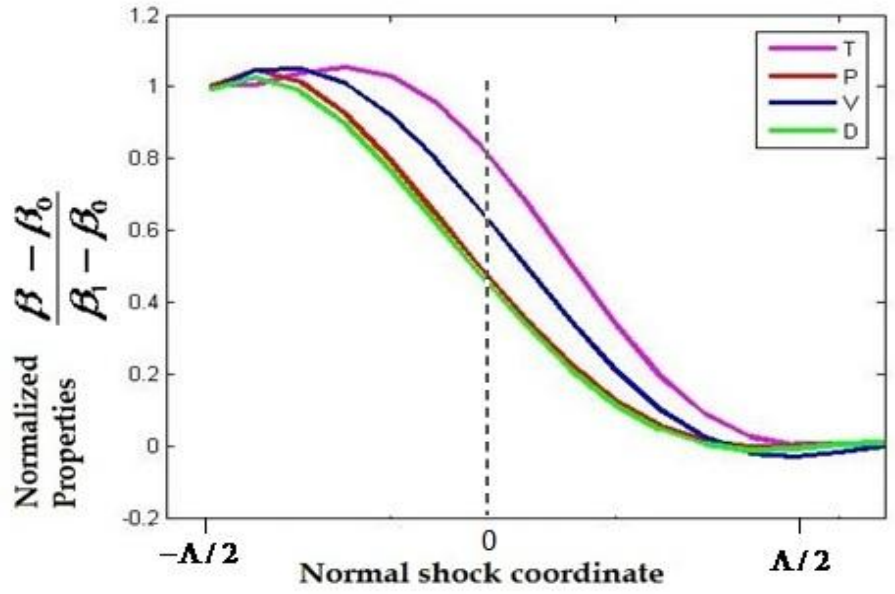

Fig 2.5 Normalized properties across the shock wave, where the subscripts 0 and 1 denote the pre– and post–shock state, respectively.

The temperature across the shock front leads all the quantities. This is due to the overshoot in temperature due to the increase in the normal component of velocity and temperature is in the order of velocity square. Velocity leads pressure and density but lags temperature due to the increase in the normal component of velocity.

When the shock wave has a steady profile, then, in coordinate fixed on the shock wave, the flows of mass, momentum and energy must have constant values throughout the steady profile:

ρu , $P_{yy} + \rho v^2$, $(E + (P_{yy} / \rho) + \frac{1}{2} v^2)\rho v + q$

All are conserved for $v_s - v_p \le v \le v_s$. P_{yy} and $q = -\kappa dT / dy$ are fluxes of y-momentum and energy in a co-moving frame of velocity *u* in the fluid respectively. ρ is the mass density and E is internal energy (excluding the kinetic energy of mass motion associated with the stream velocity *v*) per unit mass. When the conserved momentum and energy fluxes are evaluated far from the shock, where P_{yy} is equal to the equilibrium (inviscid and isotropic), pressure P and the heat flux h vanishes, then the conservation relations provide three relations among the material properties of the shocked and un-shocked material.

$\rho_0 v_0 = \rho_1 v_1$, $P_0 + \rho_0 v_0^2 = P_1 + \rho_1 v_1^2$, $E_0 + (P_0 / \rho_0) + \frac{1}{2} v_0^2 = E_1 + (P_1 / \rho_1) + \frac{1}{2} v_1^2$

Where subscripts 0,1 refer to un-shocked and shocked states respectively.

Considering a stationary shock, the un-shocked material (ρ_0, T_0) flows at velocity v_s toward a piston where the material is compressed to ρ_1 and heated to temperature T_1 and moves with the receding piston at velocity $v_s - v_p$, therefore, by the mass conservation

$\rho(y)v(y) = \rho_0 v_s = \rho_1 (v_s - v_p)$ hence $v_s = v_p / (1 - \rho_0 / \rho_1)$.

Volumetric strain in the shock is given by $\varsigma = \rho_0 / \rho_1 - 1 = -v_p / v_s$

Volumetric strain rate at the shock front $\dot{\varsigma} = \varsigma v_s / \Lambda = -v_p / \Lambda$, where Λ shock thickness.

Referring to fig 2.4, the max gradient of the density profile across the shock is -0.152 $m_w \psi_w^{-4}$ hence shock width Λ = 6.614 σ_w, also for ρ_0 / ρ_1 = 0.38, piston speed v_p = 4.0 we calculate: shock speed v_s = 6.452, volumetric strain ς =-0.62 and volumetric strain rate $\dot{\varsigma}$ =-0.605 s^{-1}.

2.5 Shock wave propagation in the gas channel

2.5.1 Temperature

Figure 2.6 shows the temperature profiles in the flow along the gas channel behind the moving shock wave at various instances. The shock and the induced flow behind appear to be developing up to the distance of $40\psi_w$ where the temperature reaches a constant value. The shock impacts the end wall (target) and it is subsequently reflected moving in the opposite direction, towards the piston. This reflection is associated with a considerable increase in temperature and a temperature ratio of about 4 across the incoming shock wave is been observed; however, across the reflected shock the temperature is about 8 times greater than that of the un-shocked gas.

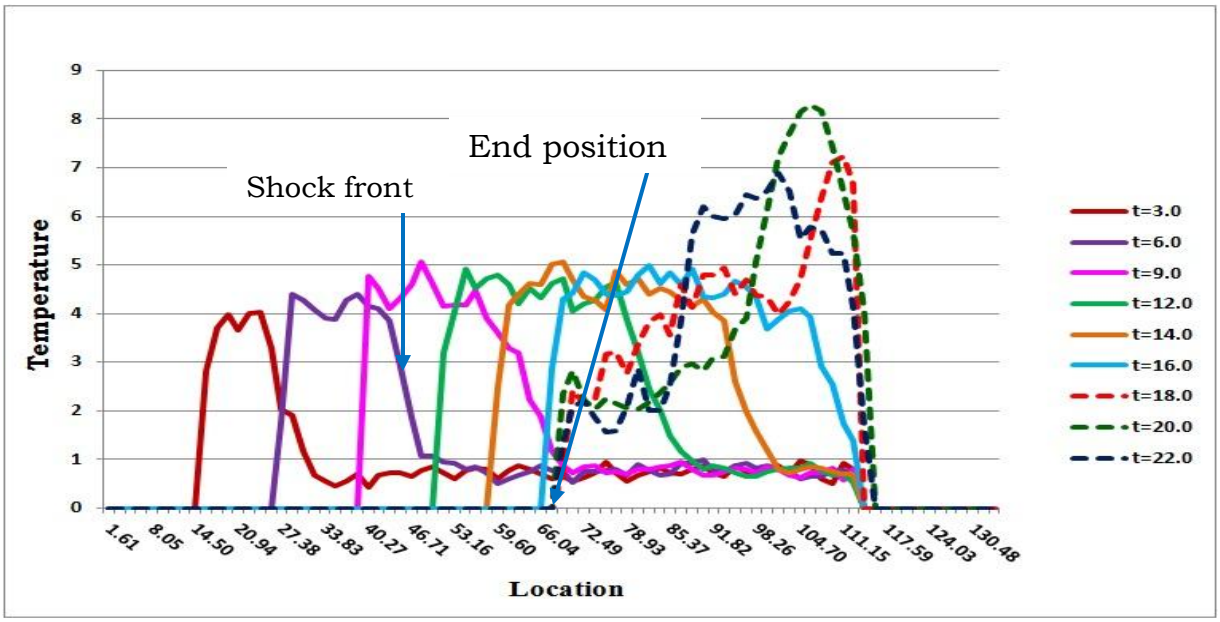

Fig 2.6 Temperature profiles in the gas flow domain generated by the propagating shock wave at various times.

At the solid wall, the shock wave is partially reflected and partially transmitted into the solid phase with energy being exchanged, so that part of the shock wave energy is reflected back into

the gas channel and the remaining part is exchanged with the solid molecules. The transmitted shock starts propagating inside the solid structure till it hits the holding wall. Unlike the microscopic behavior, the gas temperature behind the reflected shock is not constant at different times. Initially the temperature is high, and is subsequently decreased due to the energy exchange with the solid wall particles. The reflected shock off the end wall propagates toward the piston which has been stopped some time earlier and secondary reflections occur. The simulations were terminated at this time.

2.5.2 Pressure

As shown in fig 2.7 the pressure profiles in the gas channel exhibit a behavior similar to that of the temperature. The pressure ratio across the incoming shock wave is about 10 and about 5 across the reflected shock. Due to the energy exchange with the solid molecules, there is a pressure drop behind the reflected shock as it propagates back into the gas channel.

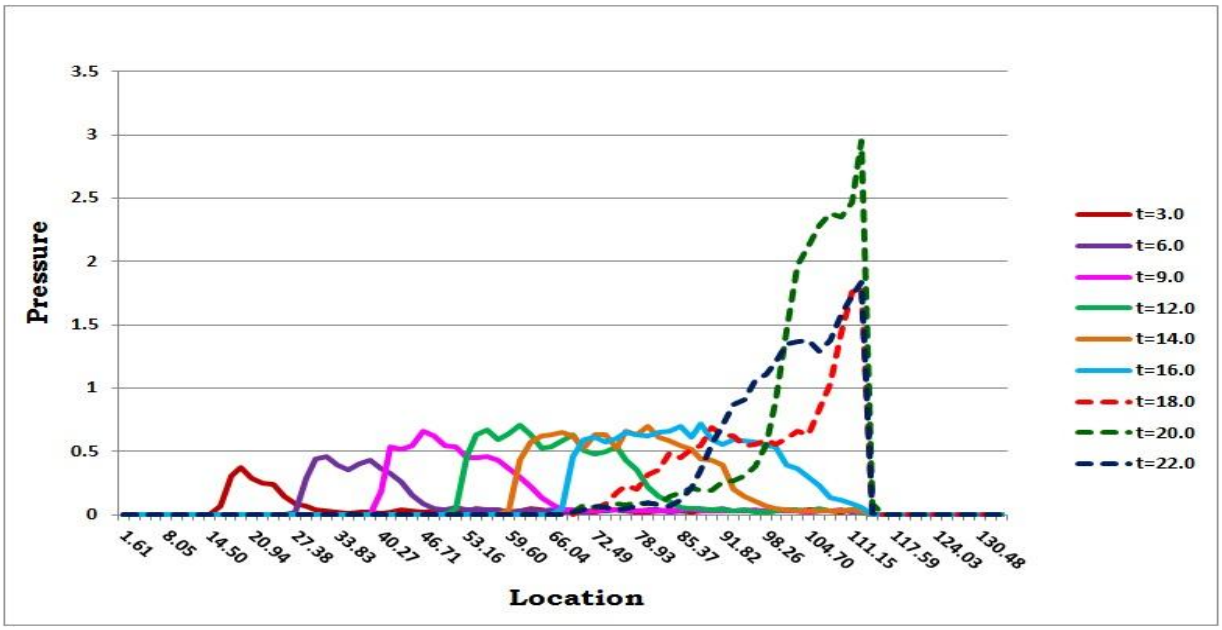

Fig 2.7 Pressure profiles in the gas flow domain generated by the propagating shock wave at various times.

2.5.3 Velocity

Figure 2.8 shows the velocity profiles of the shocked gas particles ahead of the piston which is the same as that of the piston. The results show that the distance between the shock front and the piston is getting greater as the simulation time increases since the shock speed is higher than the induced velocity of the molecules behind. Once it hits the target, reflection causes deceleration of the gas flow and eventually the flow changes direction towards the piston. When the shock hits the solid wall, not only energy is exchanged, but also the solid structure deforms, initially pushed and displaced in the downstream direction and subsequently in the opposite direction, which causes the gas flow to change direction. In the respect, the solid phase wall behaves like a vibrating elastic wall which is initially displaced in the y-positive direction during which the flow is decelerated followed by a displacement in the y- negative direction which results in a push of the gas molecules in the same direction.

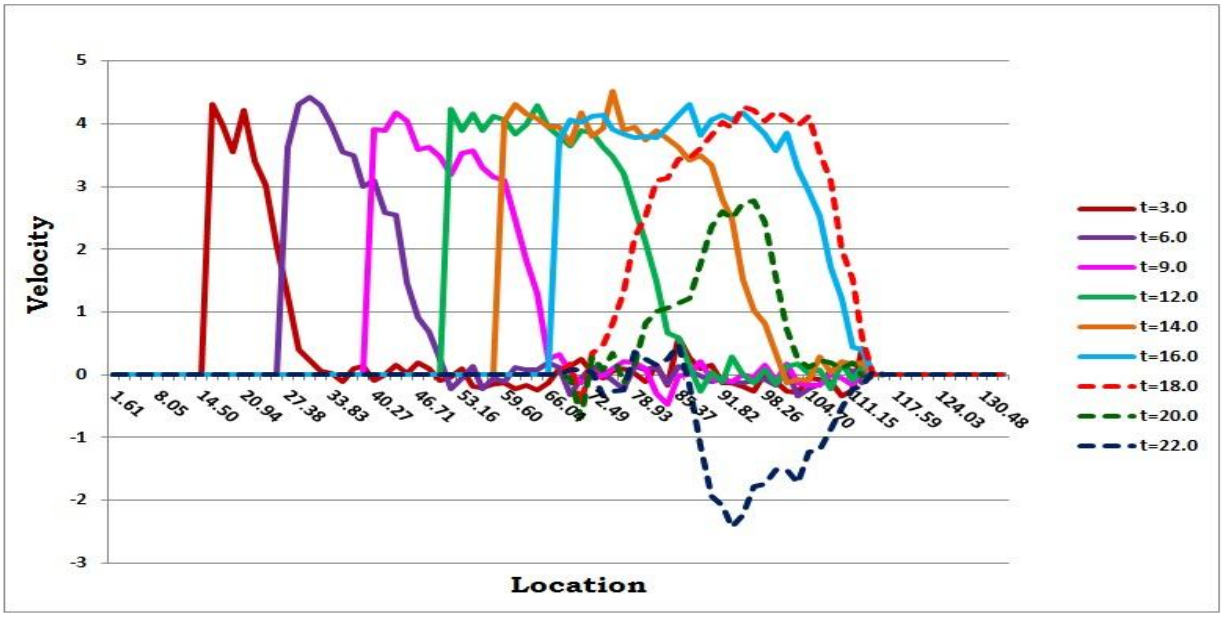

Fig 2.8 Velocity profiles in the gas flow domain generated by the propagating shock wave at various times.

2.5.4 Density

Figure 2.9 shows the density profiles in both the un-shocked and the shocked gas regions as the shock wave propagates in the gas channel. At the solid surface reflection takes place and density builds up gradually. At t=18, the first profile after the shock refection, the maximum density observed is 0.185. It builds up further to a maximum value of 0.185 almost twice that of the shocked gas. As the shock reflection goes on, a drop in gas density is observed in the region close to the solid-phase wall which is due to its elastic behavior. The drop in density in the left part of each of the density profiles after the shock reflection is associated with the arrest of the piston motion.

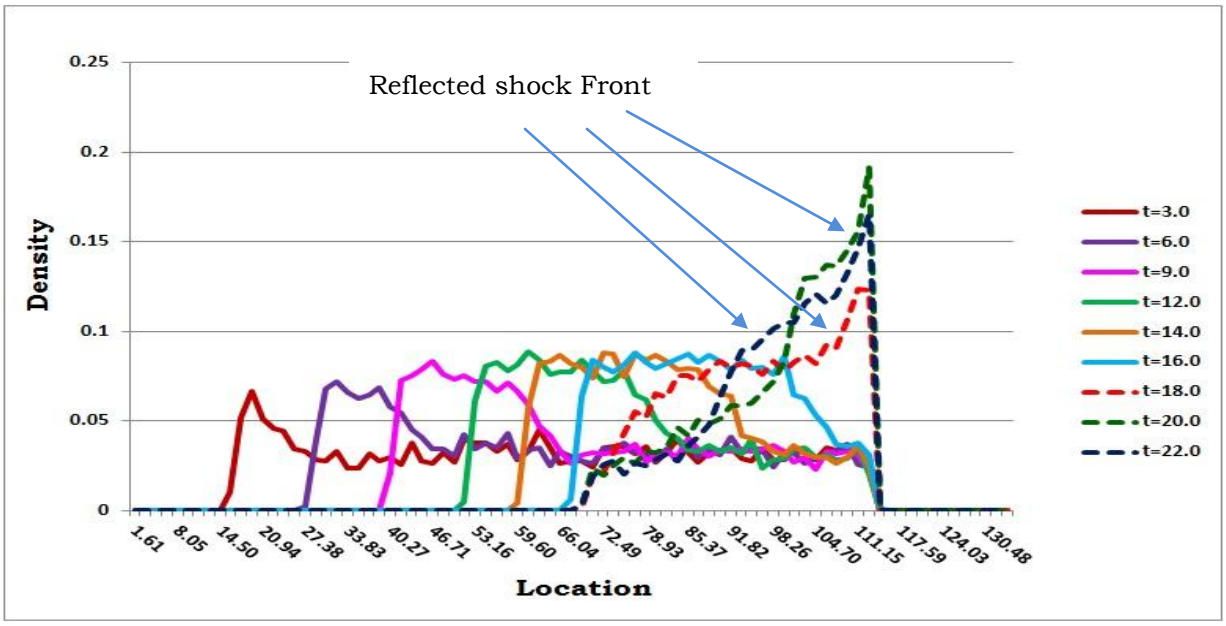

Fig 2.9 Density profiles in the gas flow domain generated by the propagating shock wave at various times.

2.5.5 Heat flux

Profiles of the heat flux in the gas channel during the shock propagation are shown in figure 2.10. The distribution of the heat flux is basically affected by the behavior of the gas molecular velocity and therefore some obvious similarities are evident between the heat flux and the velocity profiles. The heat flux increases across the propagating shock front.

During the shock wave reflection at the solid wall, the heat flux reaches a maximum value which is about 25% higher than that of the shocked gas behind the incoming shock. This jump in heat flux is due to the conversion of kinetic energy into heat during the reflection as well as to heat conduction that takes place at the wall. The heat flux decreases at different times after the shock reflection takes place and then changes sign as the flow changes direction.

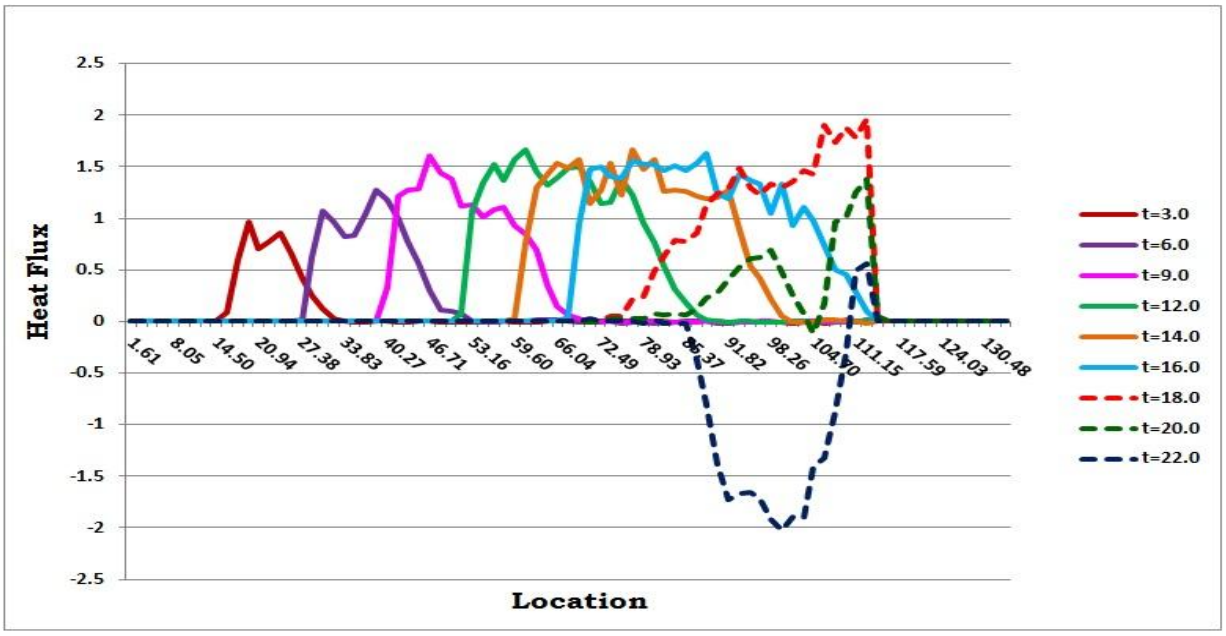

Fig 2.10 Heat flux profiles in the gas flow domain generated by the propagating shock wave at various times.

2.6 Shock at the solid surface

2.6.1 Normal stress at the gas solid interface

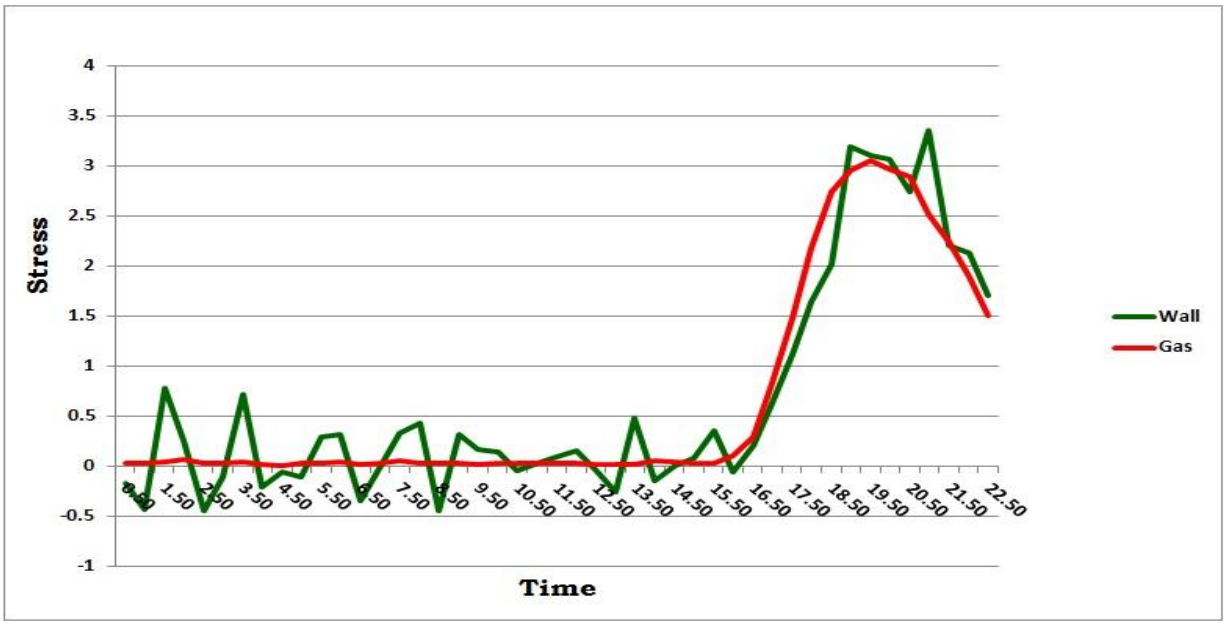

Fig 2.11 Continuity of normal stress at the gas solid interface during shock impact

Fig 2.11 shows that continuity of normal stress is observed and maintained during the shock impact on the solid structure. Both gas and solid during equilibrium have the same value of normal stress. When the shock hits the solid wall, normal stress in both solid and gas increases to a maximum and then decreases after the shock reflection takes place.

2.6.2 Gas pressure on the solid wall

Fig 2.12 shows that gas pressure increases as the shock wave hits the solid wall where kinetic energy of the gas molecules is converted to potential energy. During shock reflection pressure builds up on the wall, where most of the kinetic energy is changed into potential energy and flow

goes to rest before it changes direction and propagates back into the gas channel. Gas energy is exchanged with solid molecules and a drop of the pressure inside the gas phase is observed.

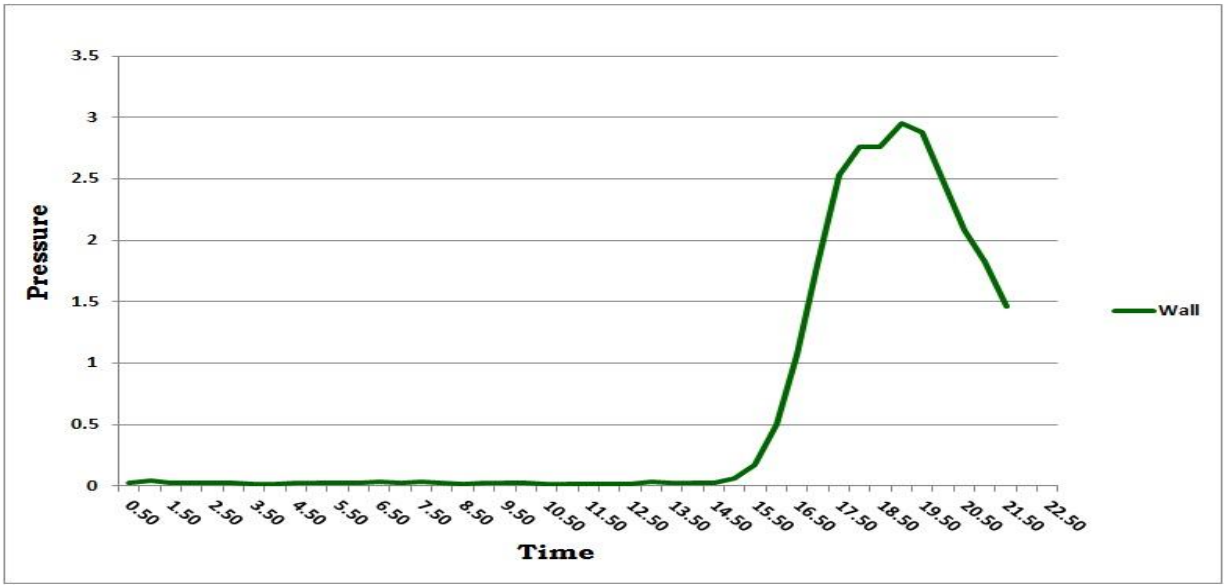

Fig 2.12 Variation of the gas total pressure on the solid wall during shock impact

2.6.3 Normal stress and its impulse on the solid wall

Impulse in the time integral of forces acting on the wall, normal stresses will exert impulsive forces on the solid structure. Numerical integration was used by applying the trapezoidal rule over the time period from the instant the piston starts moving till the end of simulation. When the shock wave hits the solid wall, the force exerted on the solid wall particles depends on the shock wave pressure and time duration of the shock impact. The impulsive force is the integral of the normal force that is normal stress multiplied by the wall area over the time duration. Since the pressure gradient across the shock wave is large and during reflection there is pressure buildup on the solid wall, the impulse significantly increases when shock hits the wall and during reflection. As the shock reflection proceeds normal stresses acting on the solid wall decreases a lower impulse force is exerted on the wall. The normal impulse can be calculated by considering

the normal stresses of the solid particles or the normal component of stress of the gas flow particles since continuity of normal stress maintained at all times, see fig 2.13 and fig 2.14.

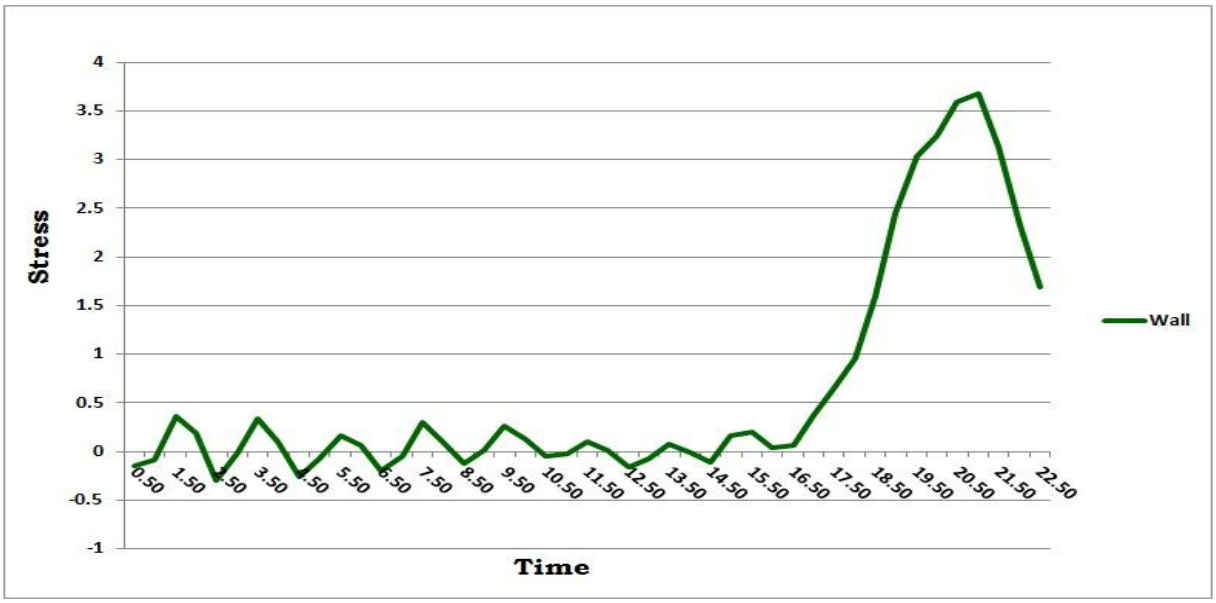

Fig 2.13 Variation of the average normal stress in the solid wall during shock impact

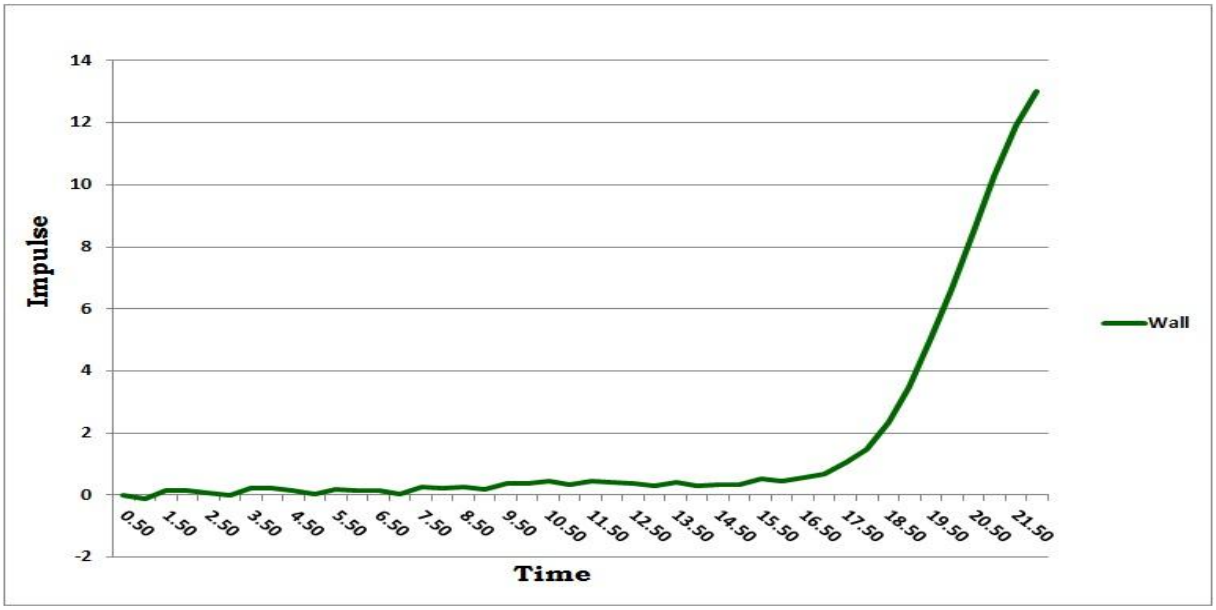

Fig 2.14 Variation of the solid wall normal impulse during shock impact

2.7 Solid properties

2.7.1 Average shear modulus

Referring to fig 2.15, before the shock hits the solid wall, the average shear modulus oscillates around a mean value. Once the shock hits the wall, it reaches a maximum value before it goes back to its average value when shock reflection takes place. The rise in the shear modulus due to strain rate effect is about 10%

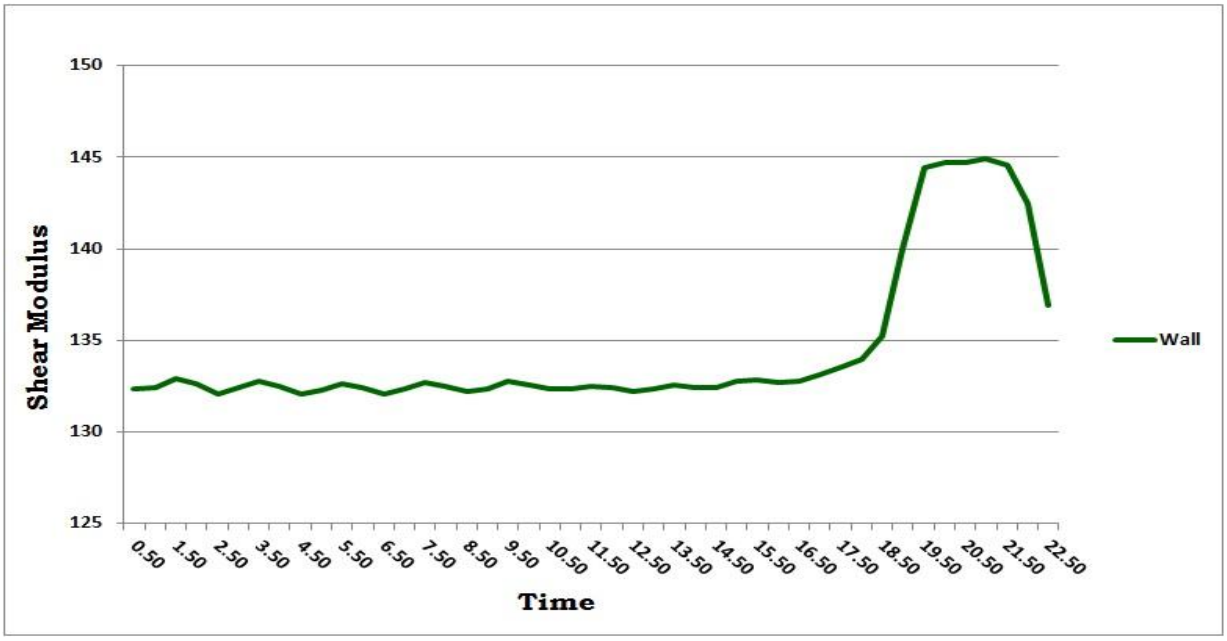

Fig 2.15 Variation of the average shear modulus of the solid-phase wall during shock impact

2.7.2 Local shear modulus

Referring to fig 2.16, at equilibrium front slabs have the same average value since they are surrounded by solid molecules that interacting only according to the 'GEAM' potential. However, solid particles at the end slab of the solid wall are interacting with the holding wall particles according to the 'SHRAT' potential that doesn't possess any embedding contribution, so the average value of shear modulus at the back edge is less than that of the front slabs. As the

shock wave hits the wall, front slabs will experience the most impact and will have higher increase in the shear modulus than that in the back slabs. In the front slabs, shock impact results in a primary jump in the shear modulus before it starts decreasing and when the shock is reflected back it causes the shear modulus to have another rise; however, back slabs are closer to the holding wall and shock reflection happens earlier that that in the front slabs, in fact primary rise in shear modulus due to the shock impact shortly followed by another rise due to the shock reflection, as a result one jump in the shear modulus is observed in the back slabs.

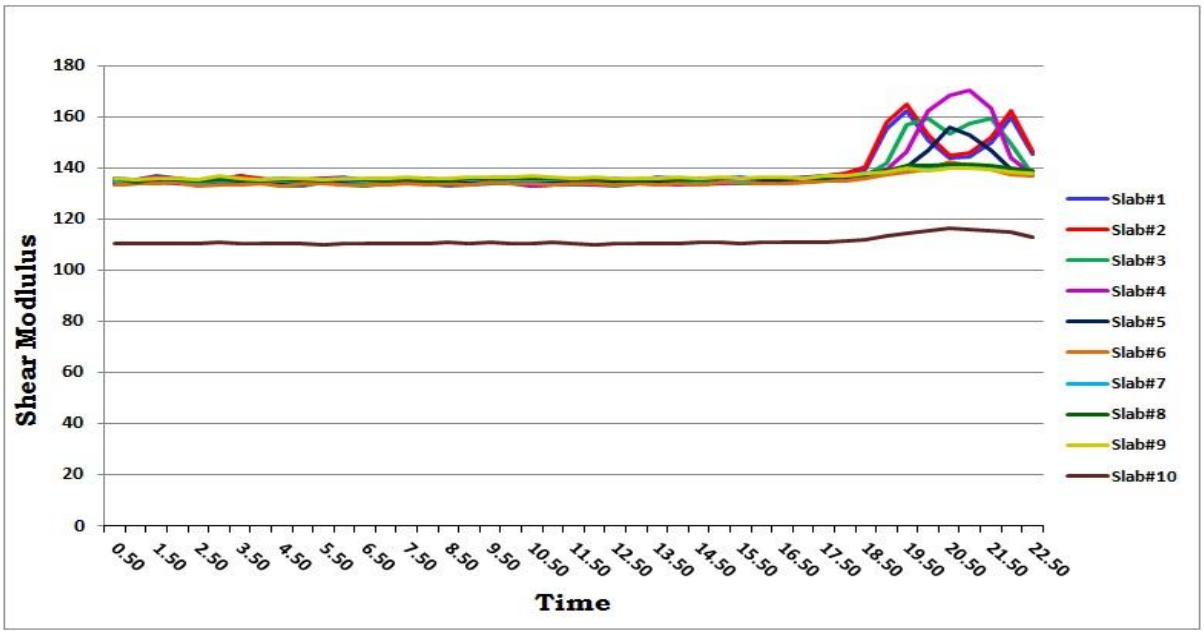

Fig 2.16 Variation of the local shear modulus of the solid-phase wall during shock impact

2.7.3 Average bulk modulus

Referring to fig 2.17, before the shock hits the solid wall, the average bulk modulus oscillates around a mean value. Once the shock hits the wall, it reaches a maximum value before it goes back to its average value when shock reflection takes place. The maximum value that was reached depends on solid wall length. The local bulk modulus figure shows that slabs far from

the gas have very little peaks compared to that of the slabs closer to the gas channel. The rise in the bulk due to strain rate effect modulus is about 7% only.

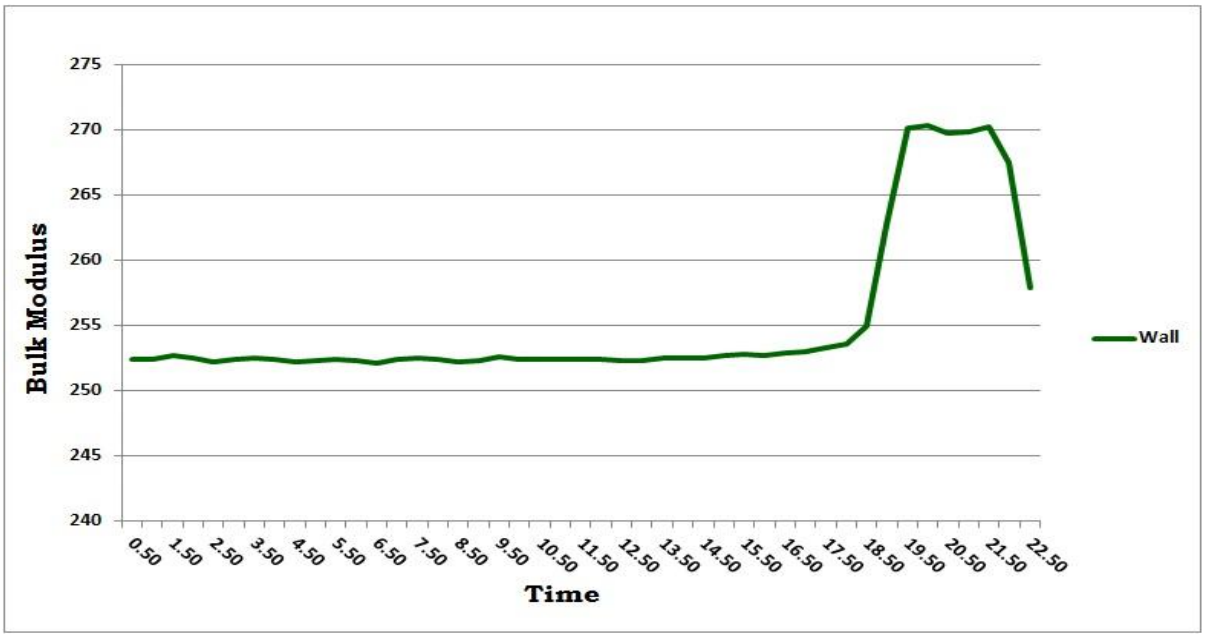

Fig 2.17 Variation of the average bulk modulus of the solid-phase wall during shock impact

2.7.4 Local bulk modulus

Referring to fig 2.18, at equilibrium front slabs have the same average value since they are surrounded by solid molecules that interacting only according to the 'GEAM' potential. However, solid particles at the end slab of the solid wall are interacting with the holding wall particles according to the 'SHRAT' potential that doesn't possess any embedding contribution, so the average value of bulk modulus at the back edge is less than that of the front slabs. As the shock wave hits the wall; front slabs will have the most impact and will have higher increase in the bulk modulus than that in the back slabs. In the front slabs, shock impact results in a primary jump the bulk modulus before it starts decreasing and when the shock is reflected back it causes the bulk modulus to have another rise, however, back slabs are closer to the holding wall and

shock reflection happens earlier. The primary rise in the bulk modulus due to the shock impact is shortly followed by another rise due to the shock reflection, therefore one jump in the bulk modulus is observed.

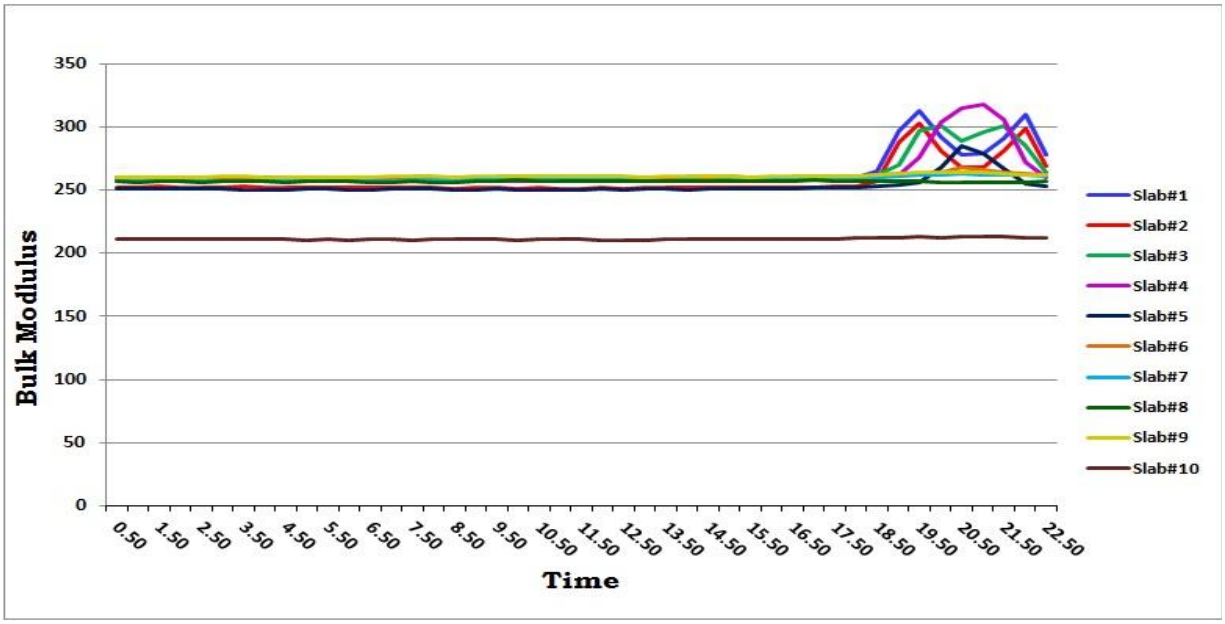

Fig 2.18 Variation of the local bulk modulus of the solid-phase wall during shock impact

2.7.5 Local displacement

The holding wall was introduced to better calculate the embedding density function and its derivatives and to limit the solid wall motion in the normal direction. Referring to fig 2.19, at equilibrium, solid particles are vibrating around a mean local locations; local displacement of solid particles close to the holding wall is negative due to the repulsive forces exerted by the holding wall particles. Further particles from the holding wall are less affected by these repulsive forces and they are free to move in the positive direction, and their local displacements are higher the further from the holding wall. As the shock passes through the solid wall, solid particles will possess more kinetic energy and due to the shock impact the solid wall will be

compressed and solid particles will deflect from their equilibrium positions. Particles close to the gas channel will have higher local displacement than those closer to the holding wall. As the shock reflection takes place, particles tend to attain their equilibrium positions.

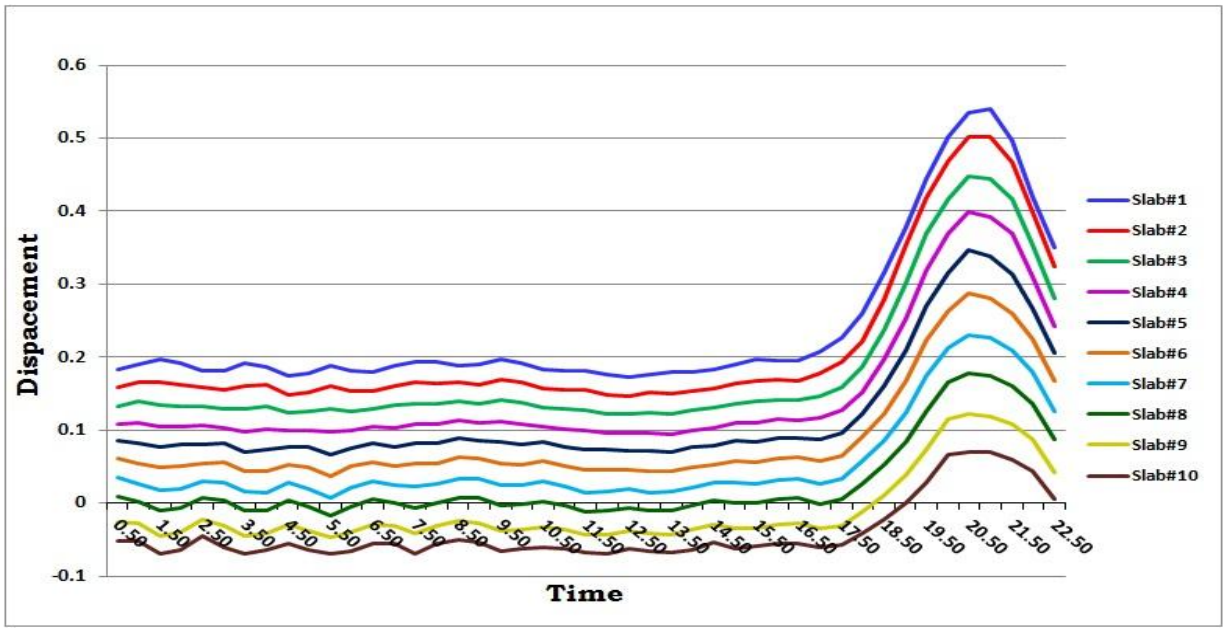

Fig 2.19 Variation of the local displacements of the solid-phase wall during shock impact

2.7.6 Average normal strain

A strain is a normalized measure of deformation representing the displacement between particles in the body relative to a reference length. Looking at fig 2.20, during equilibration and before the shock wave hits the wall, solid particles are vibrating about an average local position, distances between any two successive layers of solid particles are –on average-constant and this represents an unstrained structure. During the shock impact, the solid structure is deformed and spacing between layers of solid molecules in the normal direction is changed. Strain behavior is quite identical to that of local displacement of the solid particles; in fact, strain is the local displacement normalized by the average spacing between two successive layers of the solid

molecules. Front slabs will be deformed more than the back slabs. The average strain is obtained by averaging the local strain over the whole length of the solid wall. Strain depends on the shock wave speed and intensity which are dependent on the piston velocity and gas density.

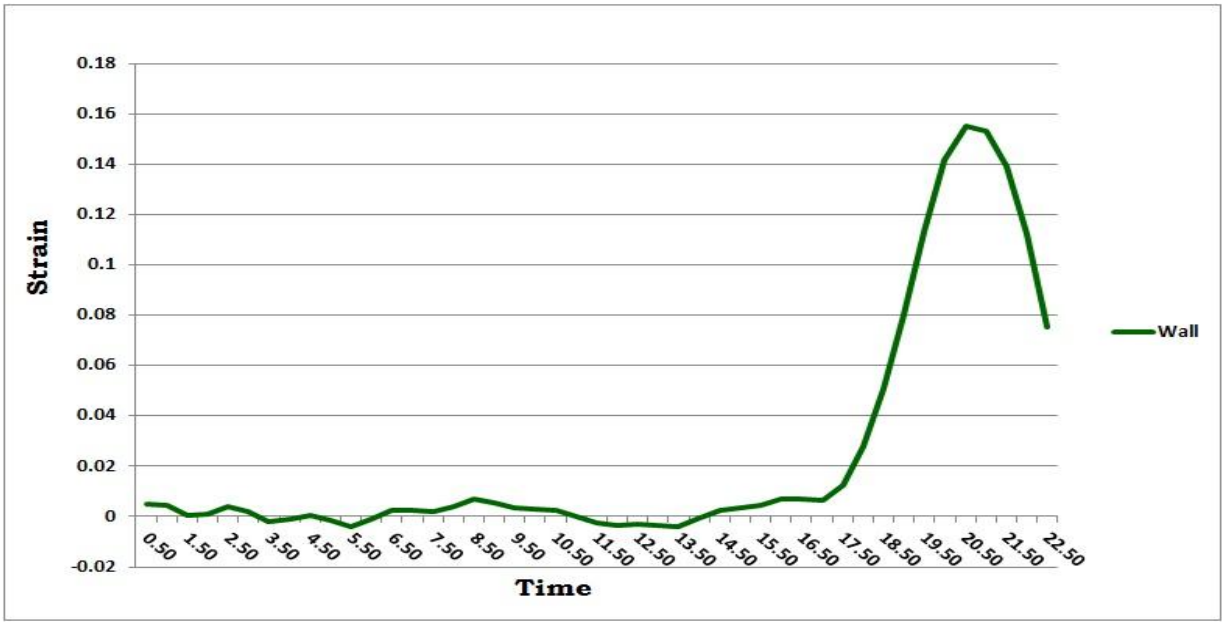

Fig 2.20 Variation of the average normal strain in the solid-phase wall during shock impact

2.7.7 Instantaneous change in energy in the solid wall

Energy in the model has the following contributions

1. Gas molecules: potential energy and kinetic energy.
2. Wall molecules: potential energy, kinetic energy and embedded energy.
3. Piston molecules: potential energy 'SHRAT and Tethering' and kinetic energy.
4. Holding wall molecules: potential energy 'SHRAT and Tethering' and kinetic energy.
5. Ghost molecules: potential energy, kinetic energy and embedded energy.

The total energy of the systems remains constant but the amount of energy in each component of the shock model varies differently but focus is made to the change in the energy of the gas molecules and the solid wall molecules.

The GEAM potential describes the interaction of the Solid-Solid molecules and Solid-Ghost molecules, whereas, SHRAT potential describes the interaction of Solid-Gas and Solid-Holding wall particles. There are three components of energy in the solid structure: Potential, kinetic and embedding. Change in energy can be found by evaluating each energy component at each time step and finding the difference in their magnitudes during the shock impact and reflection.

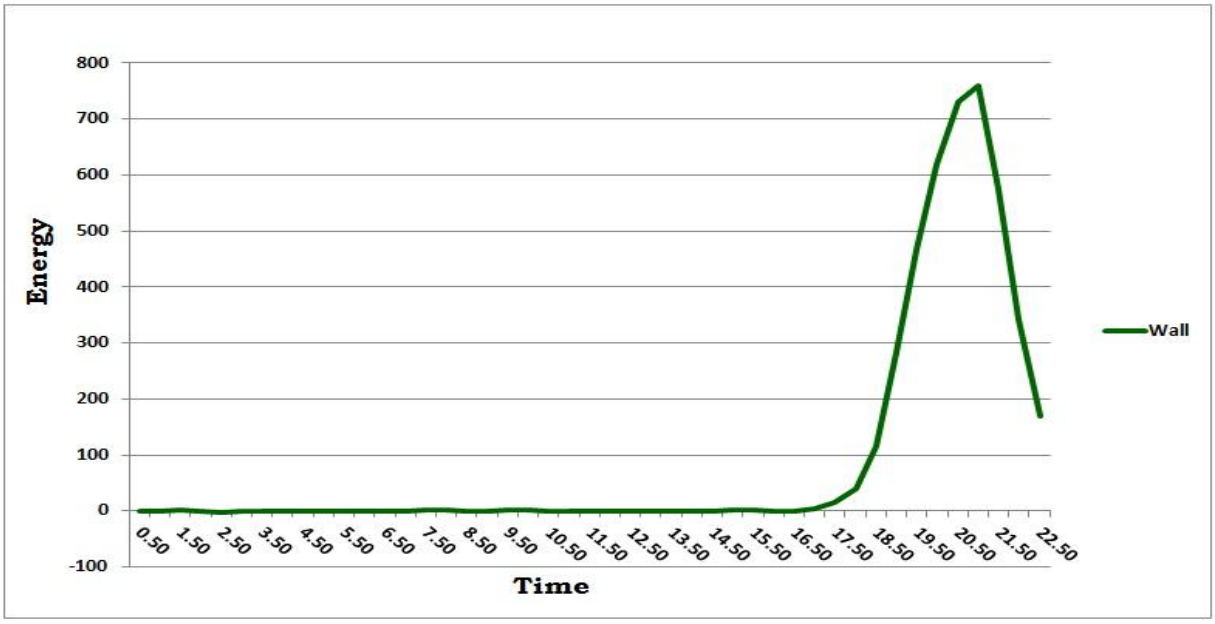

Fig 2.21 Variation of the instantaneous change in energy of solid wall particles during shock impact

However, the instantaneous change in energy can also be estimated by calculating the work done by the solid particles. The work done by the structure is the magnitude of the normal force multiplied by displacement, where normal force is the normal stress multiplied by the cross sectional area. The magnitude of the instantaneous change in energy by either way should be the same. Referring to fig 2.21, during the shock impact there is a rise in the energy in the solid structure due to energy exchange between gas particles and solid particles which results in increase in stress and strain in the solid structure. As the shock reflection takes place, structure tends to restore its unstrained state.

2.7.8 Solid properties at the interfacial slab

The bins are initially constructed in such way that the solid volume contained within 10 slabs in the normal direction with each slab contains 2 layers of solid particles. The volume of these slabs is identical to that of the solid structure. During equilibration and during the shock propagation in the gas channel, the number of solid in each slab is the same. When the shock hits the solid wall, solid particles are pushed, hence the actual volume and number of particles in the interfacial slab is reduced: however, the number of particles (i.e. density) in the next slabs gets higher than that of the equilibrium value. The deviation between the actual volume of the solid particles and the slab volume requires some attention when calculating the solid properties or any other quantity that is averaged over the volume.

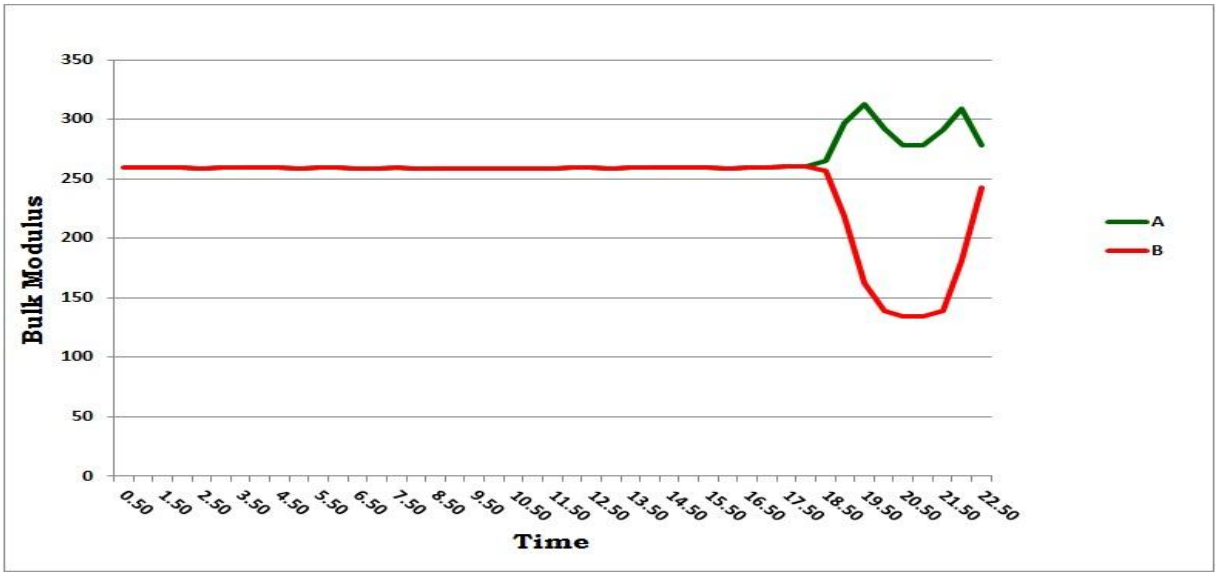

Fig 2.22 Variation of the local bulk modulus of the interfacial slab during shock impact, A: based on the actual volume, B: based on the slab volume

Figure 2.22 above shows the local bulk modulus of the interfacial slab during the shock propagation in the solid. When the average is performed based on the slab volume, there is a

reduction in the bulk modulus during compression and this contradicts the physical behavior of solids during compression. The bulk modulus $B = -V(\partial p / \partial V)$ where V is the volume, during compression there is a rise in pressure and a reduction in volume and the bulk modulus should increase. One should note that bulk modulus of the inner slabs increases. The bulk modulus reduction resulted from averaging over the slab volume which is higher than that of the actual solid volume in the interfacial slab.

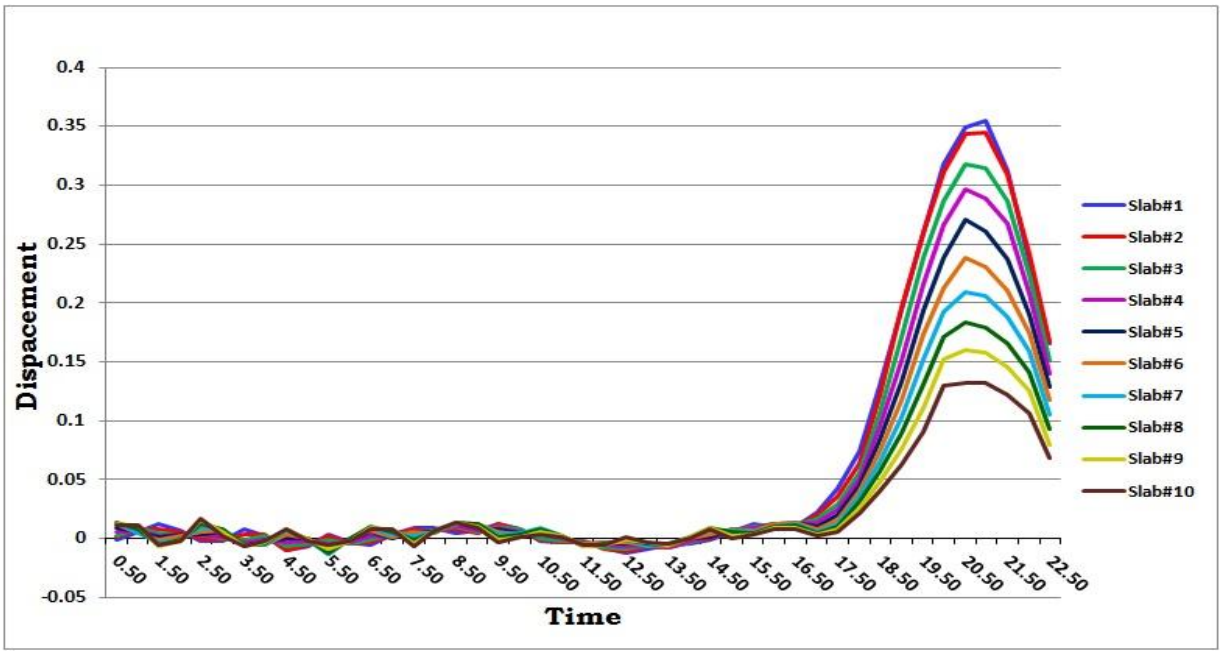

Fig 2.23 The Variation of the local relative displacement of the solid-phase wall during shock impact

The bulk modulus was more accurately determined when the actual volume was calculated and then introduced to correct the resulting modulus at the interfacial slab. The correction was made by assuming the density of the first two slabs are the same and hence the actual volume of the solid is calculated accordingly. The above approximation was adopted after the relative local displacement of the solid particles (fig 2.23) was monitored and it was found that the solid

particles in the first two slabs have the same behavior and they almost have the same peak value. The actual volume was evaluated as follows:

Density =(No. of particles/Volume) hence $\frac{N_1}{V_1} = \frac{N_2}{V_2}$ and $V_1 = \frac{N_1}{N_2} V_2$

2.8 Effect of the initial gas density

In addition to our standard case study (2708 gas particles), three other cases were simulated, one with 2420 gas particles, another one with 2304 gas particles and last one with 2132 gas particles. The gas channel dimensions remained the same in all the cases. The time of acceleration of the solid particles is the same. Piston particles were then allowed to move and stopped at the same time (i.e., location) in all three cases. The simulation is continued to the same final time in all three cases.

2.8.1 Average shear modulus

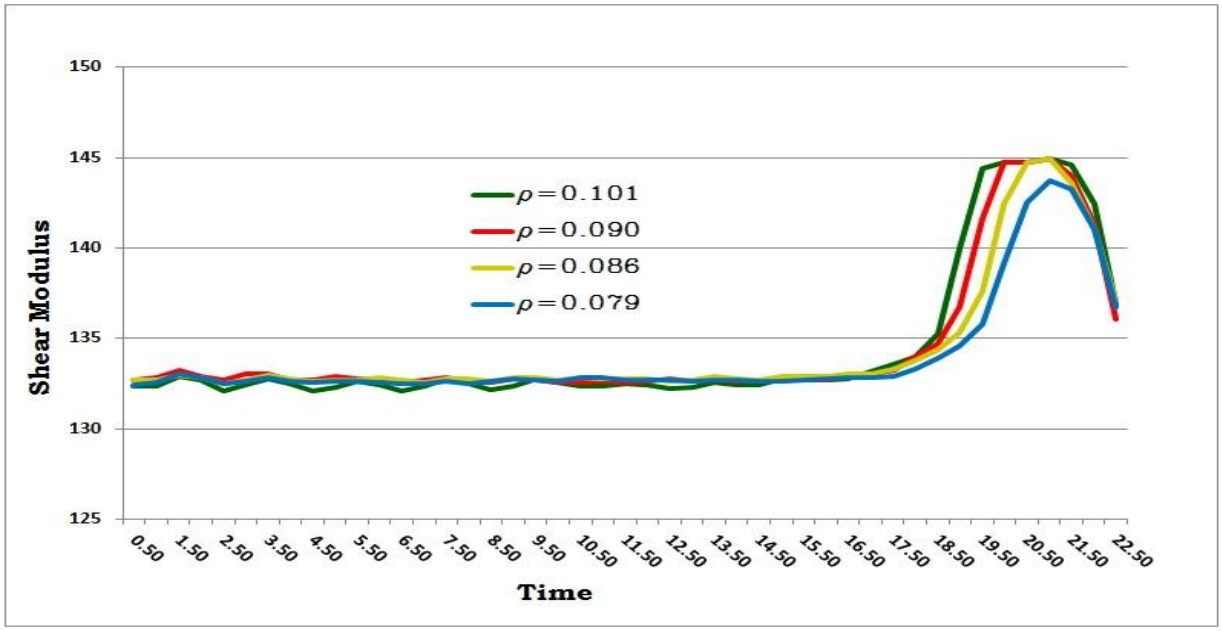

Fig 2.24 Effect of the initial gas density on the average shear modulus

Fig 2.24 shows that solid wall in all cases has the same average shear modulus before the shock hits the wall. Since shock intensity is proportional to gas density, shock produced in the dense channel will have a higher speed and will hit the wall earlier than those with lower density. The rise in shear modulus due to the stress-stain rate effect was about 10 % in all cases. After reflection takes place the structure tend to attain its equilibrium state.

2.8.2 Average bulk modulus

Fig 2.25 shows that the solid wall in all case has the same average bulk modulus before the shock hits the solid wall. A higher initial gas density will produce a shock wave with higher speed and intensity and will hit the wall earlier than the channel with less gas particles and the rise in bulk modulus happens earlier. A 7% increase in the bulk modulus due to stress-stain rate effect was observed in all these three cases, after reflection takes place structure tends to attain its unstrained state.

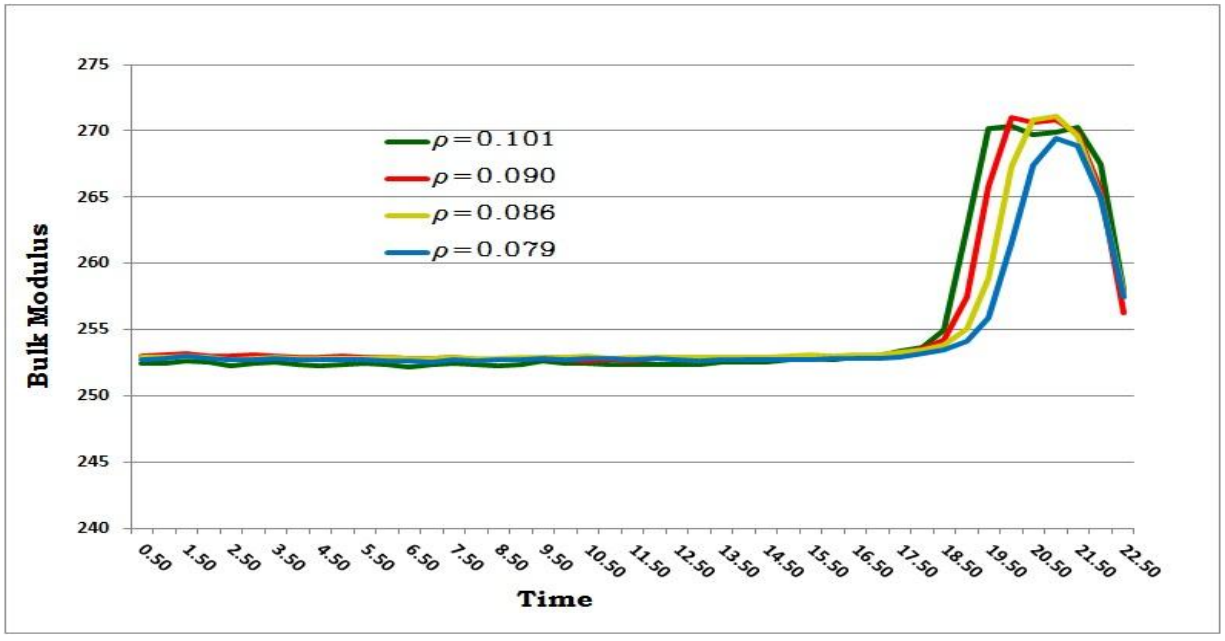

Fig 2.25 Effect of the initial gas density on the average bulk modulus

2.8.3 Normal stress and its impulse

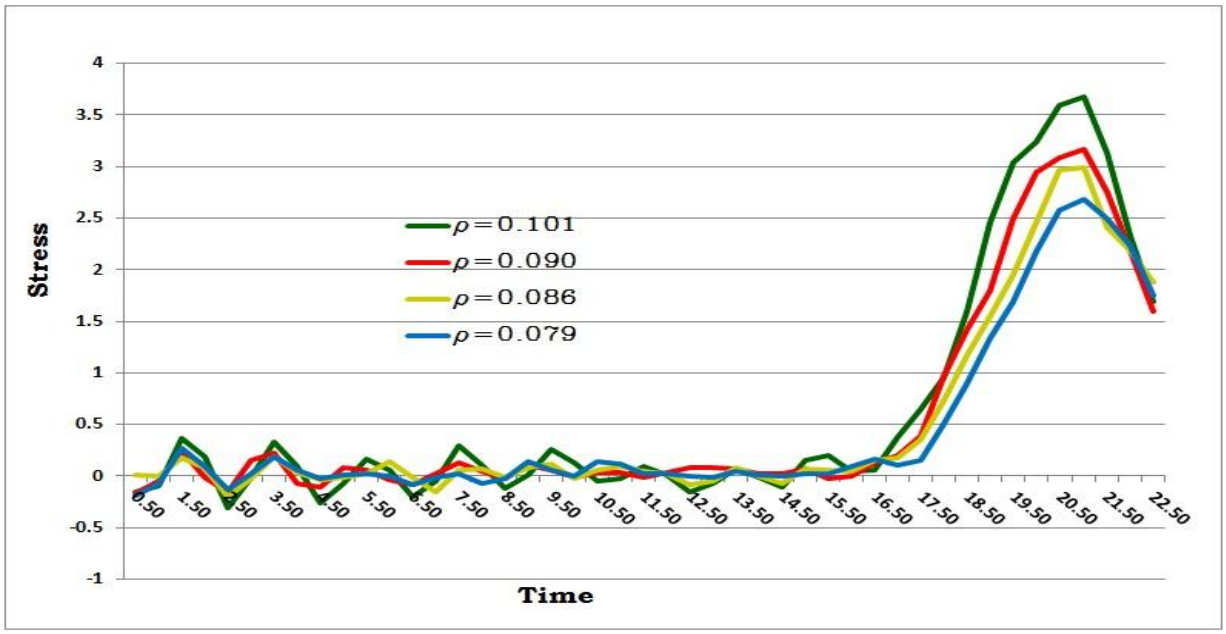

Fig 2.26 Effect of the initial gas density on the average normal stress

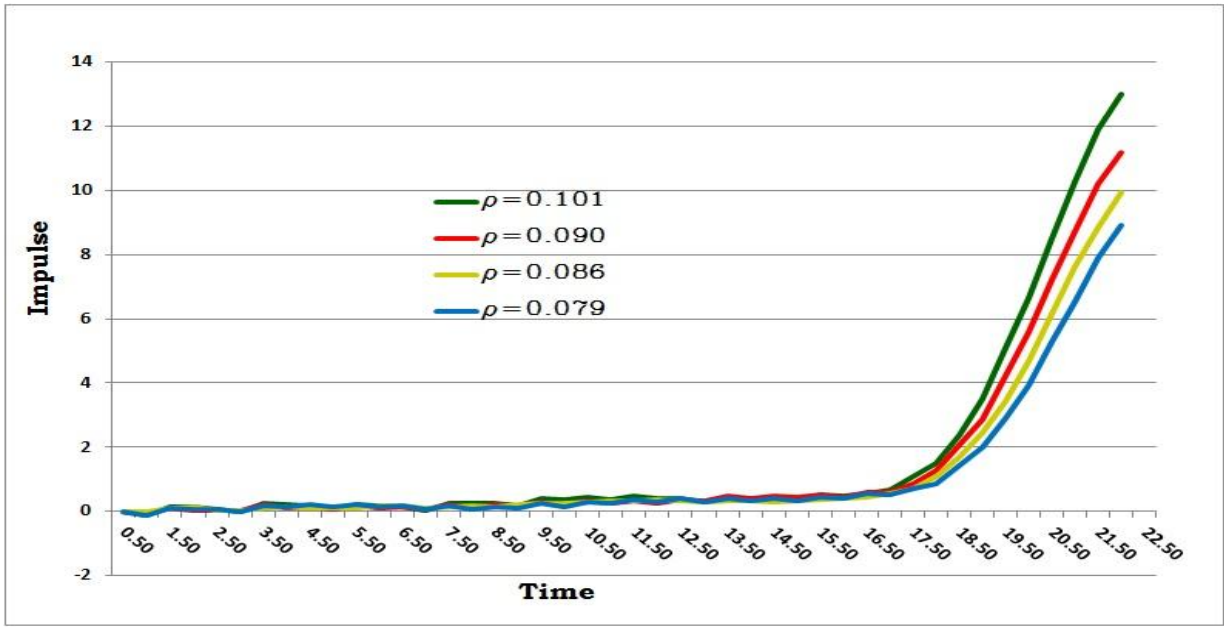

Fig 2.27 Effect of the initial gas density on the normal impulse

A higher gas density will produce a shock wave with higher speed and will hit the wall earlier than those produced by gas channels with lower densities. Moreover, the shock impact is greater as the gas density increases. The normal stress increase due to shock impact is proportional to the gas density and hence the resulting impulse. A higher gas density will result in earlier and higher rise in the normal component of stress of the solid wall particles; consequently the corresponding impulse will have earlier, higher and steeper as the gas density increases, see fig 2.26 & fig 2.27.

2.8.4 Average wall displacement

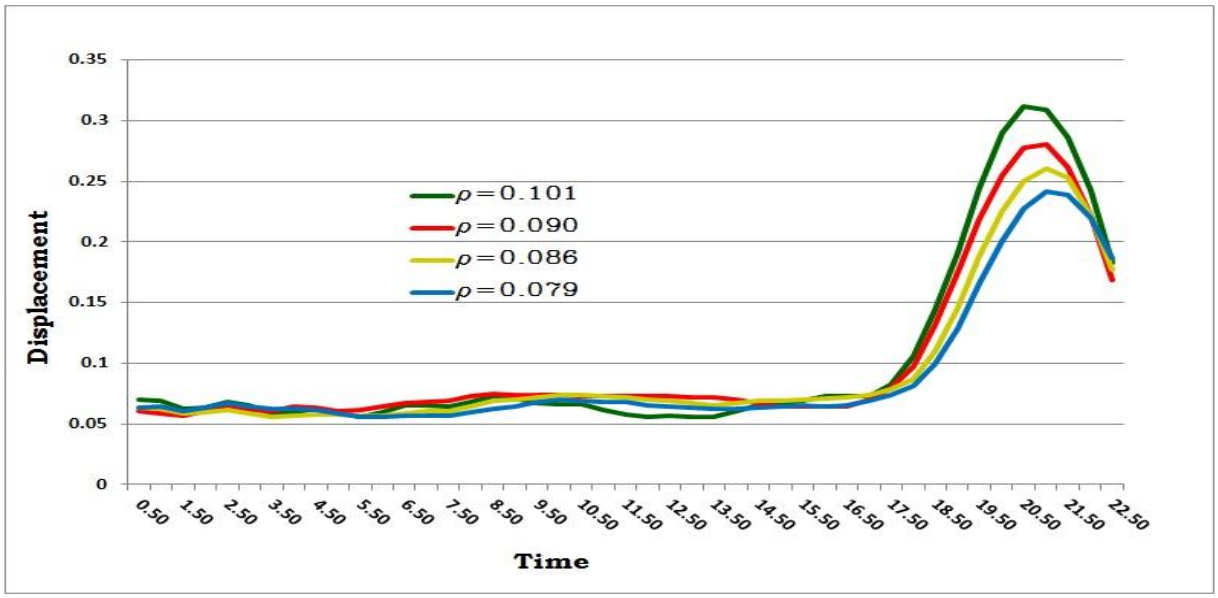

Fig 2.28 Effect of the initial gas density on the average wall displacement

Referring to fig 2.28, a higher gas density will produce a shock wave with higher speed and the shock impact happens earlier and consequently the rise in the average wall displacement of the solid structure. The shock intensity is also proportional to the gas density; the higher speed the higher the rise in the average wall displacement. After reflection takes place the structure tend to attain its equilibrium state.

2.8.5 Average normal strain

Fig 2.29 shows that during the shock impact, the solid structure is deformed and spacing between layers of solid molecules in the normal direction is changed. The strain variation with the shock impact is proportional to the shock speed and intensity. A higher gas density will produce shock wave with higher intensity and speed; hence the shock impact and the strain rise happen earlier. Moreover, the rise in the strain of the solid structure is greater.

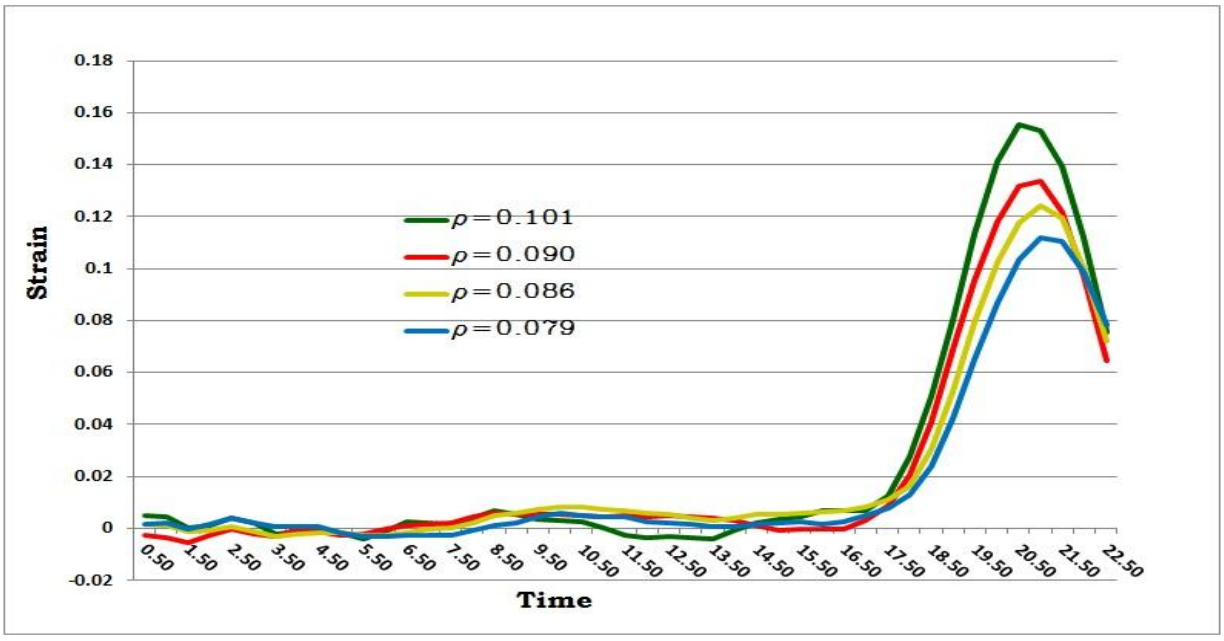

Fig 2.29 Effect of the initial gas density on the average normal strain

2.8.6 Instantaneous change in energy of the solid wall

Fig 2.30 shows that shock impact will result in an increase in stress and strain of the solid structure and consequently the energy gained by the solid particles. Both stress and strain rise in the structure is proportional to the shock speed and intensity. Moreover, shocks with higher speed will cause earlier impact. Hence, the increase in initial gas density will result in earlier and greater rise in the instantaneous energy gained by the solid particles.

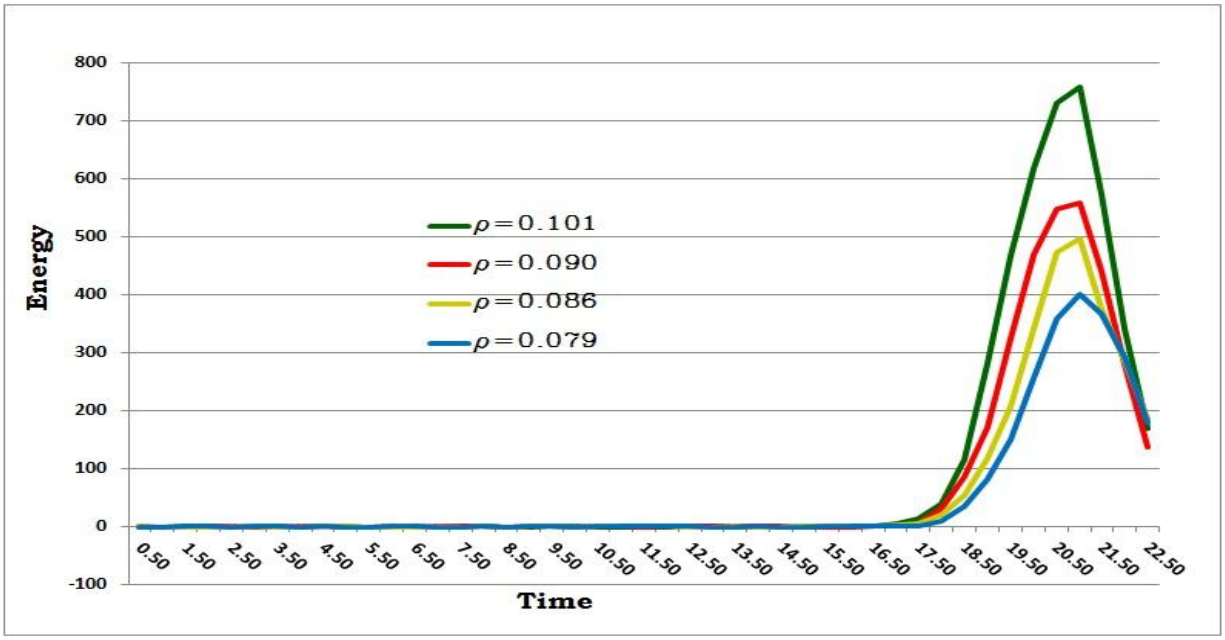

Fig 2.30 Effect of the initial gas density on the instantaneous change in energy of solid wall particles

2.9 Effect of the piston velocity

The piston was accelerated and moved at three different velocities. The time of acceleration of the solid particles is the same. Piston particles were then allowed to move and stopped at the same location in all three cases. The simulation is continued to same final time in all three cases.

2.9.1 Average shear modulus

The solid wall in all case has the same average shear modulus before the shock hits the solid wall. A higher piston speed will produce a shock wave with higher speed and intensity and will hit the wall earlier than the pistons with lower speed and the rise in shear modulus happens earlier. A 10% increase in the shear modulus was observed in all these three cases. After reflection takes place the structure tends to attain its unstrained state, see fig 2.31.

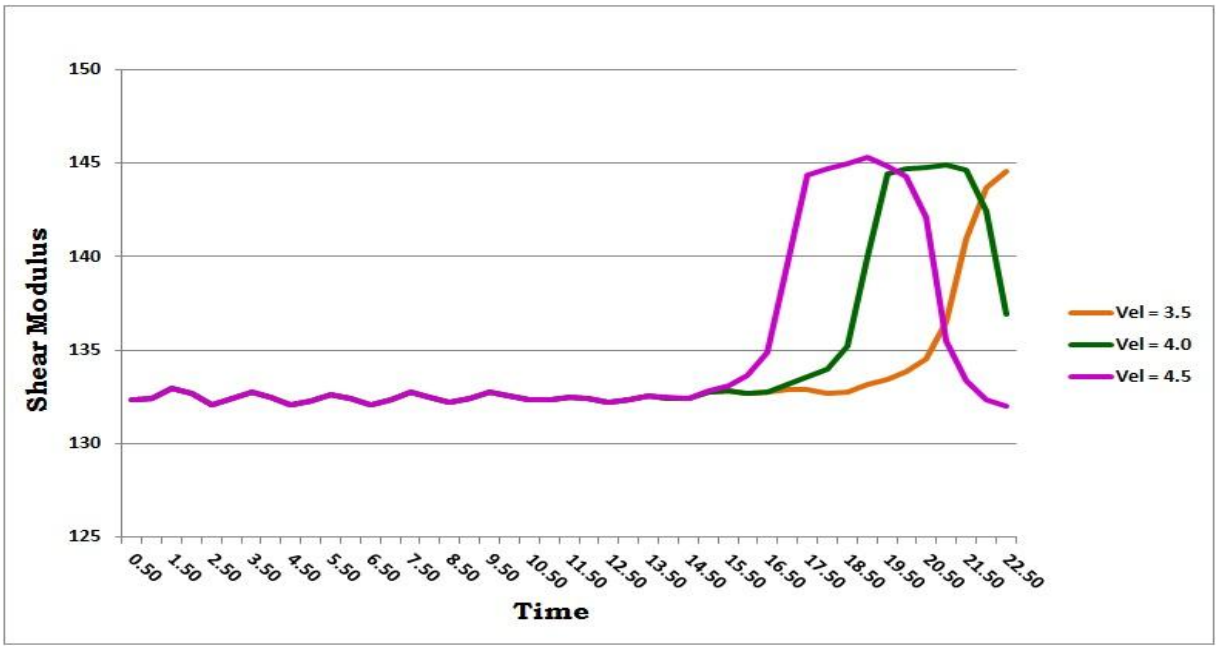

Fig 2.31 Effect of the piston velocity on the average shear modulus

2.9.2 Average bulk modulus

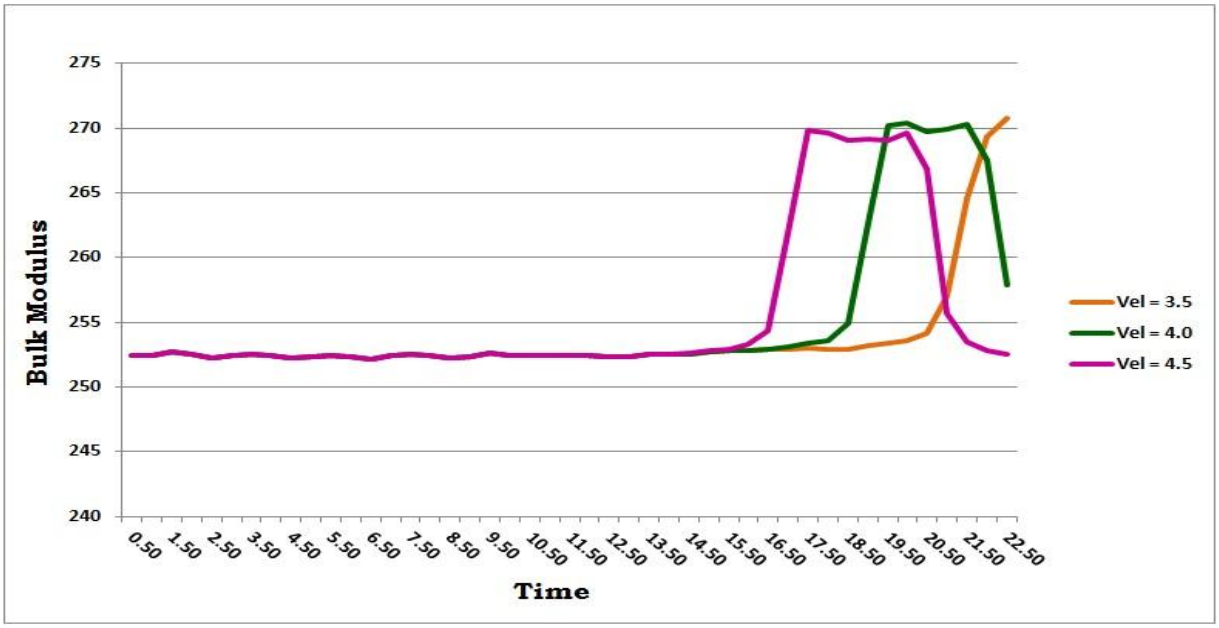

Fig 2.32 Effect of the piston velocity on the average bulk modulus

Fig 2.32 shows that in all cases, the solid wall has the same average bulk modulus before the shock impact. A higher piston speed will produce a shock with higher intensity and speed and will result in earlier higher rise in the bulk modulus. A 7% increase in the bulk modulus was observed in cases. After reflection takes place the structure tend to attain its equilibrium state.

2.9.3 Normal stress and its impulse

Referring to fig 2.33 and 2.34, a higher piston speed will produce a shock wave with higher speed and will hit the wall earlier than that produced by a piston with a lower speed. Moreover, the shock impact is higher as the piston velocity increases. The normal stress increase due to the shock impact is proportional to the piston speed and hence the resulting impulse. A higher piston speed will result in an earlier and higher rise in the normal component of stress of the solid wall particles; consequently, the corresponding impulse will be earlier, higher and steeper as the piston velocity increases.

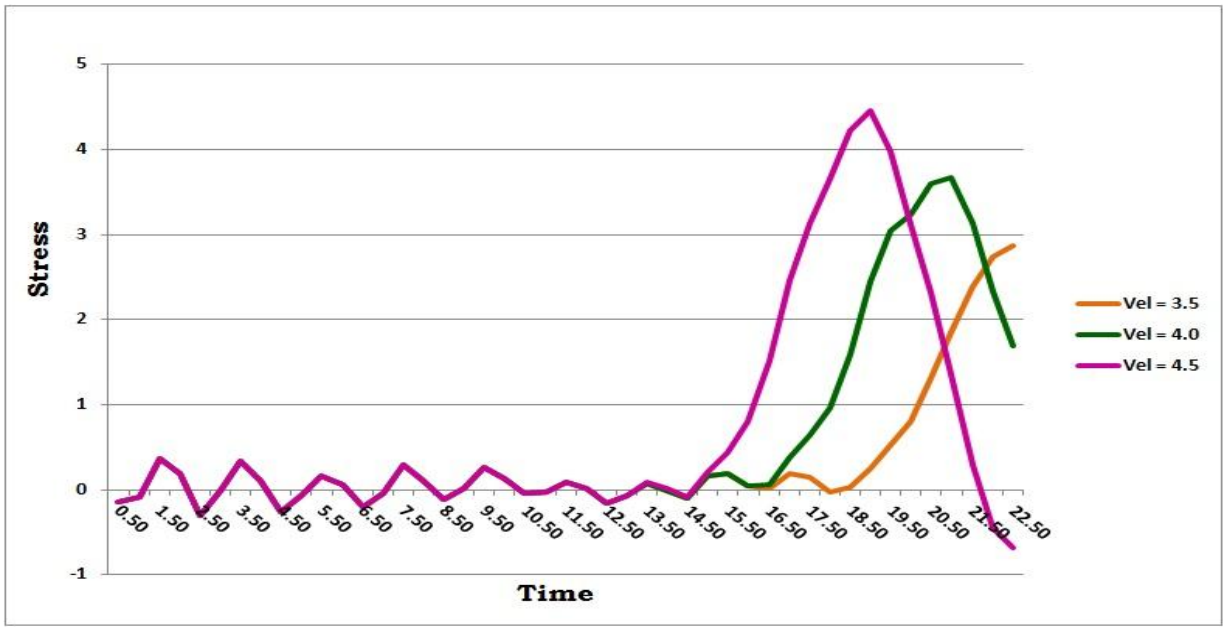

Fig 2.33 Effect of the piston velocity on the normal stress of the solid wall

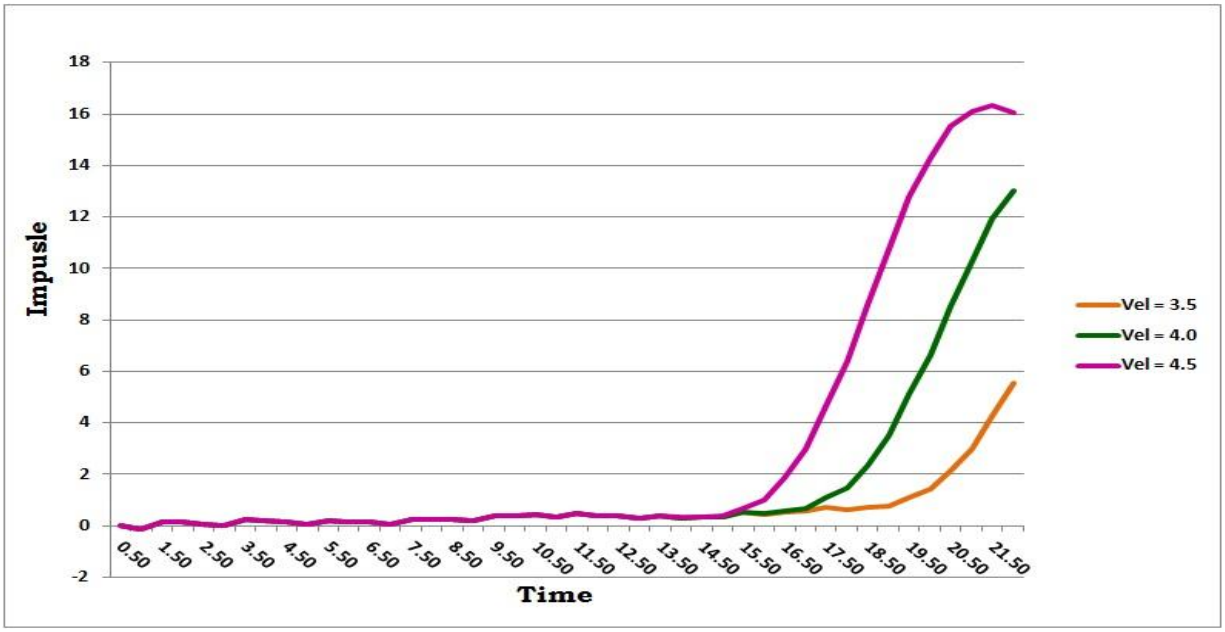

Fig 2.34 Effect of the piston velocity on the normal impulse of the solid wall

2.9.4 Average wall displacement

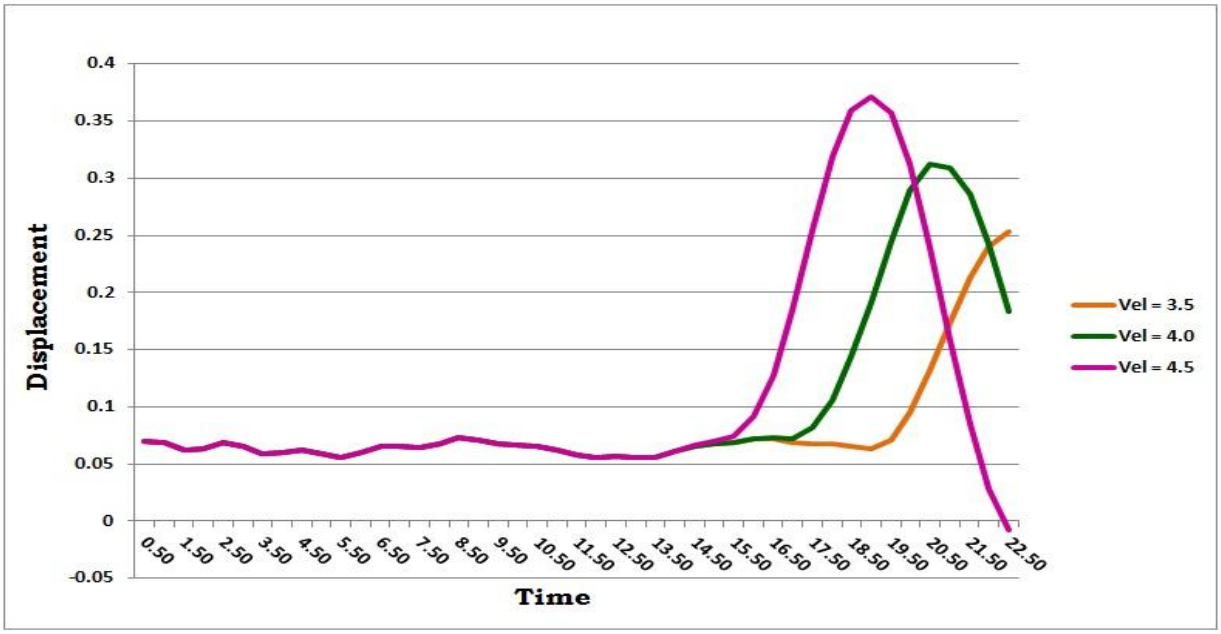

Fig 2.35 Effect of the piston velocity on the average displacement of the solid wall

Fig 2.35 shows that higher piston speed velocity will result in an earlier and higher rise in the average wall displacement. It's also obvious that in the case of the highest piston velocity, the simulation time was enough to show that the solid wall bounced back after the shock reflection took place.

2.9.5 Average normal strain

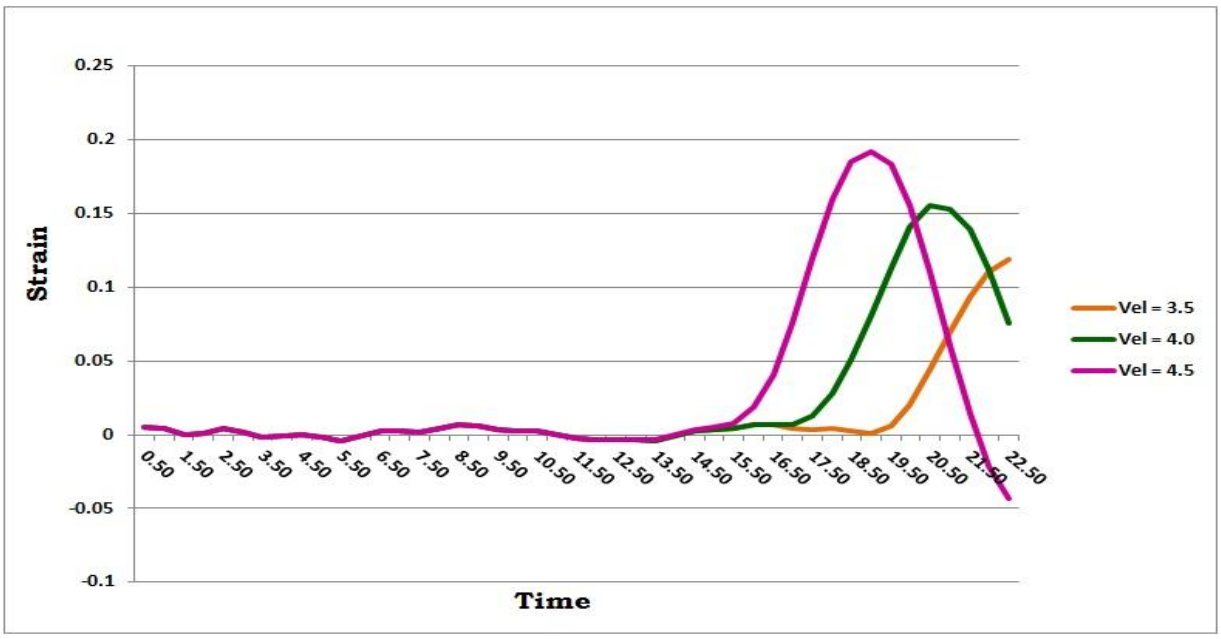

Fig 2.36 Effect of the piston velocity on the average normal strain of the solid wall

Referring to fig 2.36, the normal strain variation with the shock impact has the same response to that of the average wall displacement, where a higher piston speed will produce a shock wave with higher speed; hence, the shock impact happens earlier and consequently the rise in the normal strain of the solid structure. The shock intensity is also proportional to the piston speed and hence the rise in the normal strain.

2.9.6 Instantaneous change in energy of solid wall

Fig 2.37 shows that the shock impact will result in an increase in stress and strain of the solid structure and consequently the energy gained by the solid particles. The stress rise as well as the strain rise in the solid structure is proportional to the shock speed and intensity. Moreover, shocks with higher speed will cause an earlier impact. Hence, the increase in piston velocity will result in an earlier and greater rise in the energy gained by the solid particles.

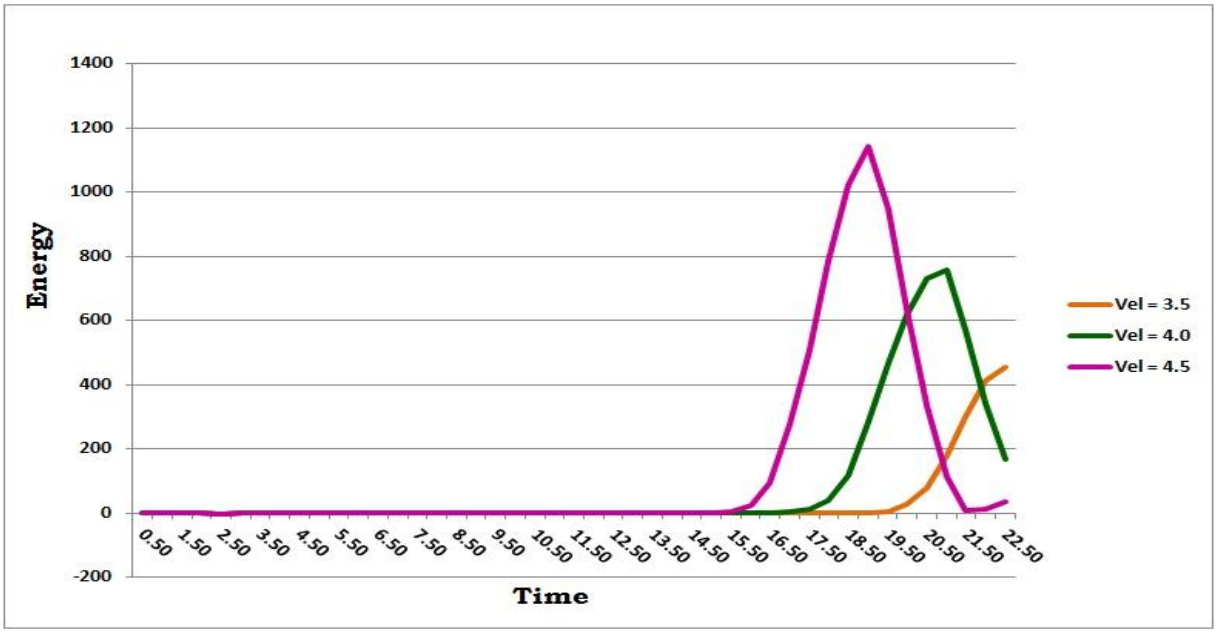

Fig 2.37 Effect of the piston velocity on the instantaneous change in energy of the solid wall

Chapter Three

Dynamics of Shock Waves impacting Porous wall

3.1 Model setup

The dimensions of the gas channel remained the same but the solid wall structure is changed. In order to form a porous structure some of the solid particles are removed to form circular poles of solid particles that are attached to full layers of solid particles. The removed particles are compensated by the ghost particles; hence, the total number of particles of the structure remains the same regardless of the number and size of the poles. Referring to fig 3.1, there are three rows of poles with three poles in each row; this sums up to nine poles. The first and third rows are in line with each other and the second is offset by half the distance between any two rows. All the poles have the same diameter and depth. Porosity is controlled by varying the poles diameter. In all cases the depth is set to $9.66\psi_w$. The volume occupied by the poles particles is the cross sectional area multiplied by the poles length. The poles are attached to a solid wall that has an axial length of $16.11\psi_w$.

When the poles are formed a desired value of the pole diameter was set. However, porosity cannot be calculated based on this diameter since the position vector has discrete values and there always will be a deviation between the desired diameter value and actual size of the produced poles. Porosity was calculated based on the number of particles in the volume occupied by the poles particles only divided by the number of solid and ghost particles in that volume.

$$\eta = \left(\frac{N_{solid}}{N_{solid} + N_{ghost}} \right)$$

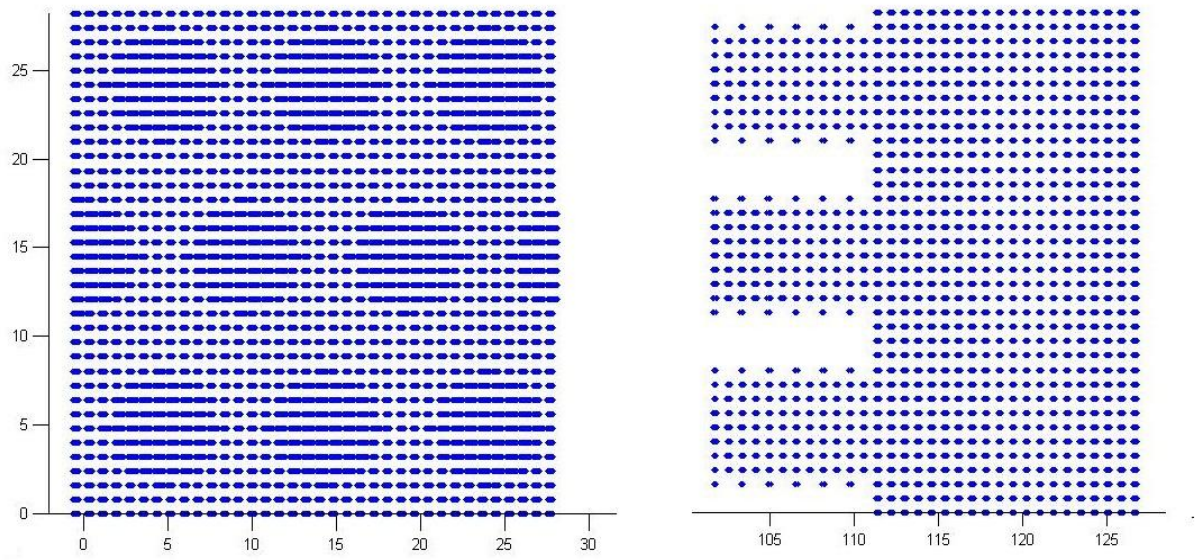

Fig 3.1 Schematic view of straight poles attached to solid structure

3.2 Shock wave propagation in the gas channel

3.2.1 Temperature

Fig 3.2 shows that shock wave was formed and developed as it was discussed earlier and it propagated in the gas channel till it hit the porous wall. Part of the shock hits the pole face and is then reflected back towards the piston: this is the *primary reflection*, while the other part of the shock keeps propagating in the space between the poles, hitting the base of the wall and then reflected back: designated as *secondary reflection*. The primary reflection results in a higher temperature rise than the secondary reflection, in the case of low porosity of 65%. As porosity increases the strength of the primary reflection decreases and the secondary reflection gets

greater. However in the case of a porous wall, the reflected shock temperature is always less than that of a solid wall. This depends on the frontal reflecting area ratio. For the same depth of each test case lower porosity is equivalent to higher frontal area associated with the primary reflection.

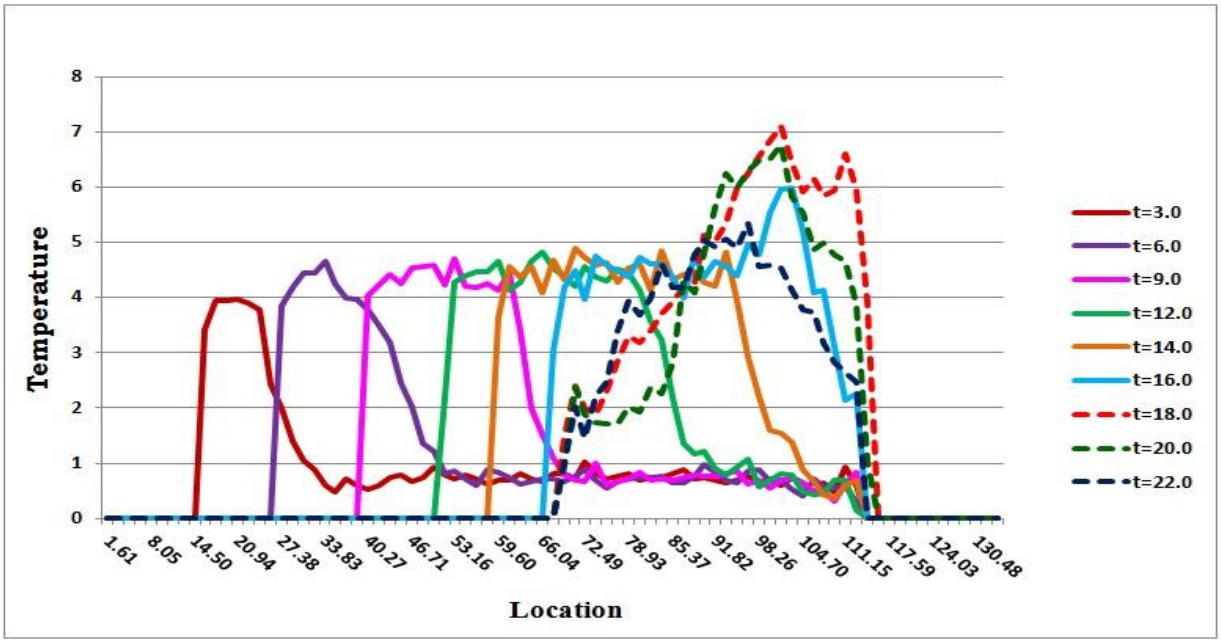

Fig 3.2 Temperature profiles in the gas flow domain generated by the propagating shock wave at various times.

3.2.2 Pressure

According to fig. 3.3, values of the pressure behind the primary or secondary reflected shocks depend on porosity. As porosity increases less frontal area is available and the primary reflection strength is weaker; on the other hand the base area becomes higher with the increase of porosity and secondary reflection is greater. The pressure behind the secondary reflection is higher than that of the primary reflection and it is less than that of the solid wall case, see fig 2.7

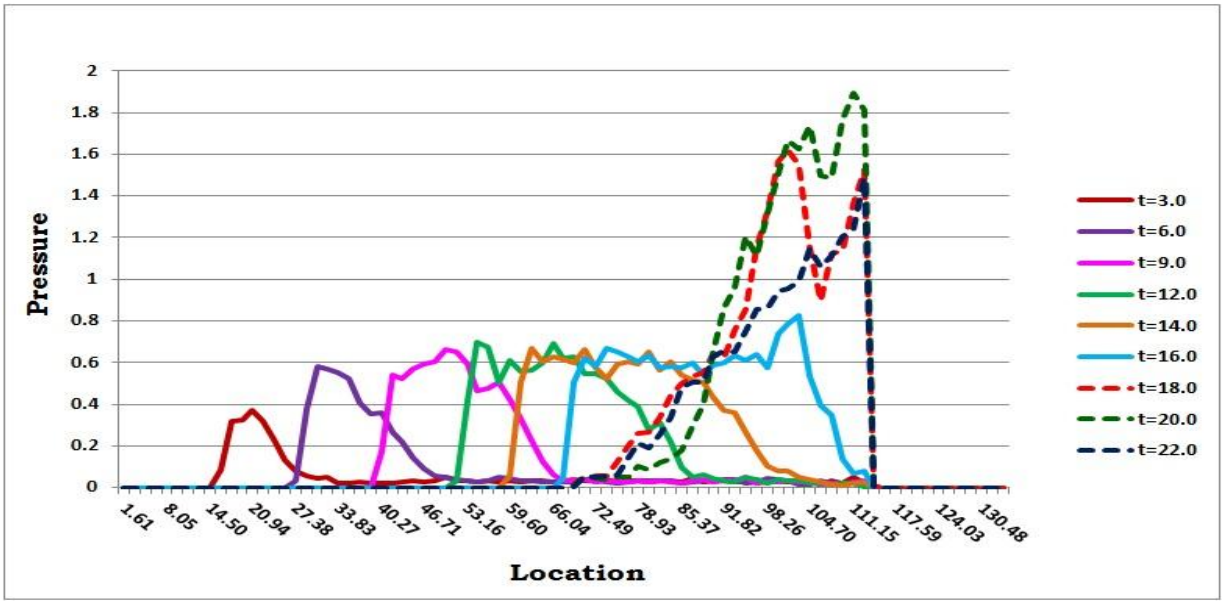

Fig 3.3 Pressure profiles in the gas flow domain generated by the propagating shock wave at various times.

3.2.3 Velocity

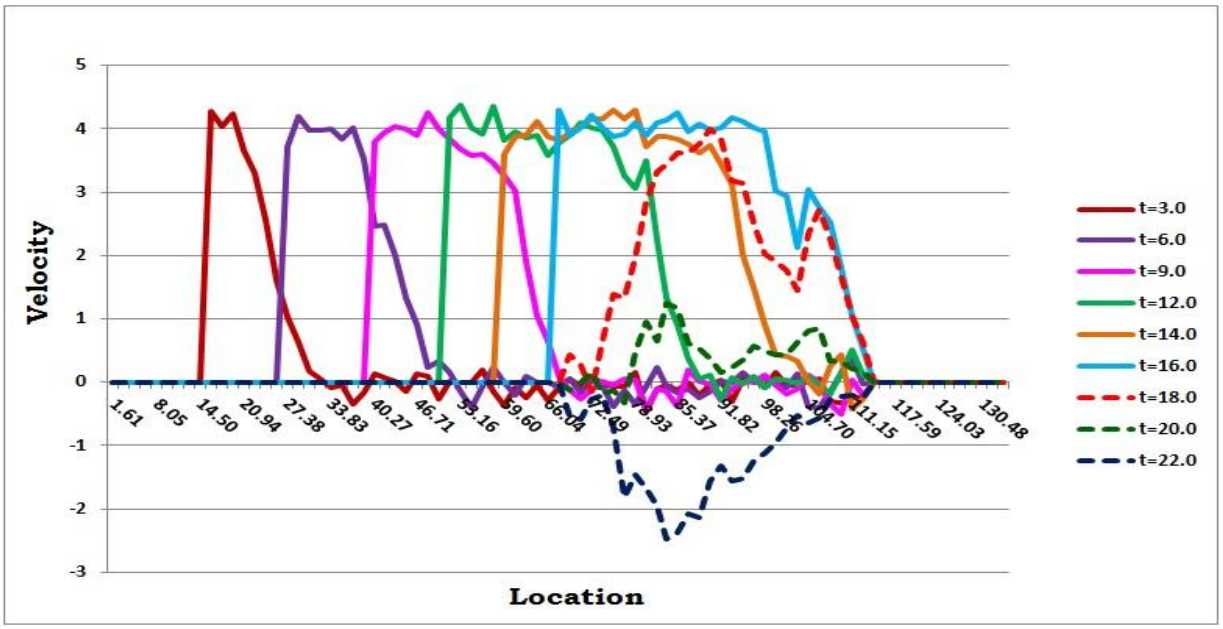

Fig 3.4 Velocity profiles in the gas flow domain generated by the propagating shock wave at various times.

Figure 3.4 shows that gas velocity at various locations along the domain for various times. The propagating shock causes the gas particles to acquire a velocity. The shock span-distance between shock front and the piston is getting greater as the simulation time increases and the shock speed gets higher as it passes through the gas molecules. Primary and secondary reflections were observed; both reflections cause deceleration of the gas flow and eventually the flow changes direction towards the piston. When the shock hits the solid wall, not only the energy is exchanged, but also the solid structure is pushed and displaced. The displacement of the solid structure causes the gas flow to change direction.

3.2.4 Density

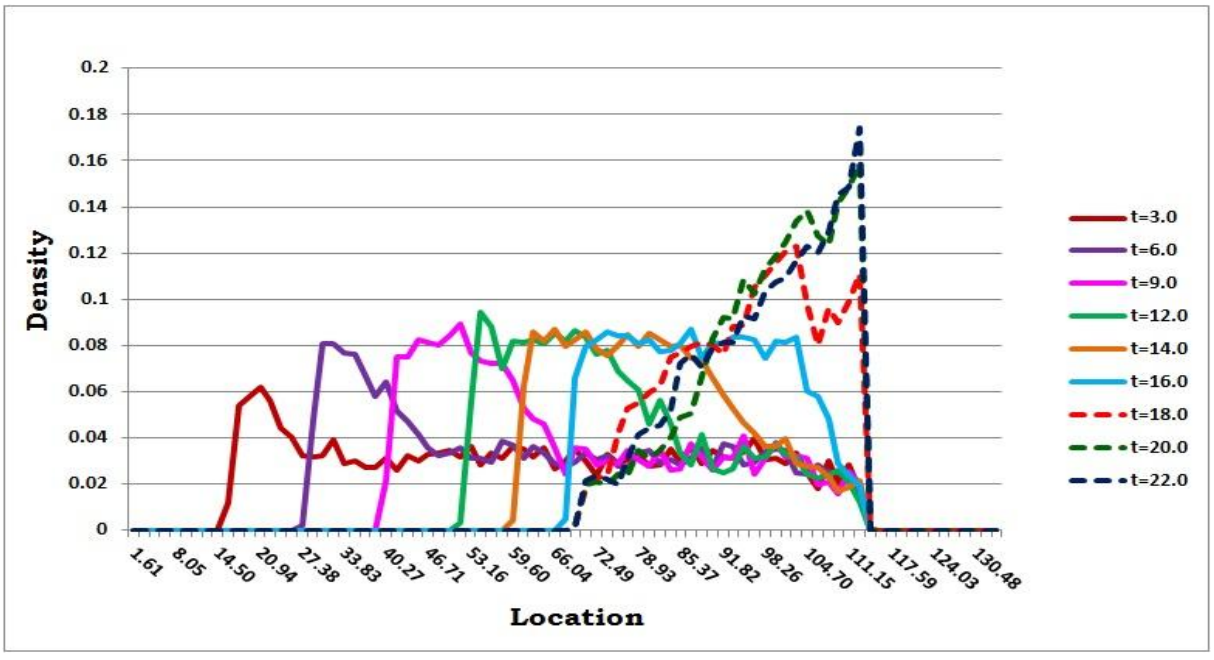

Fig 3.5 Density profiles in the gas flow domain generated by the propagating shock wave at various times.

The primary and secondary reflections have effect on all the quantities of the flow. In the case of density, as shown in fig 3.5, the density at the poles face reaches a maximum value and as the reflection continues the density decreases. However, since the secondary reflection lags the primary reflection, the density build up at the face area is then followed by another build up at the base area where it reaches a maximum value. This maximum value drops down as the flow changes direction. At 65% porosity, the maximum value of density reached during reflection at the base area is greater than that reached at the face area. However, the maximum value of density reached is less than that of the solid wall case, see fig 2.9.

3.2.5 Heat Flux

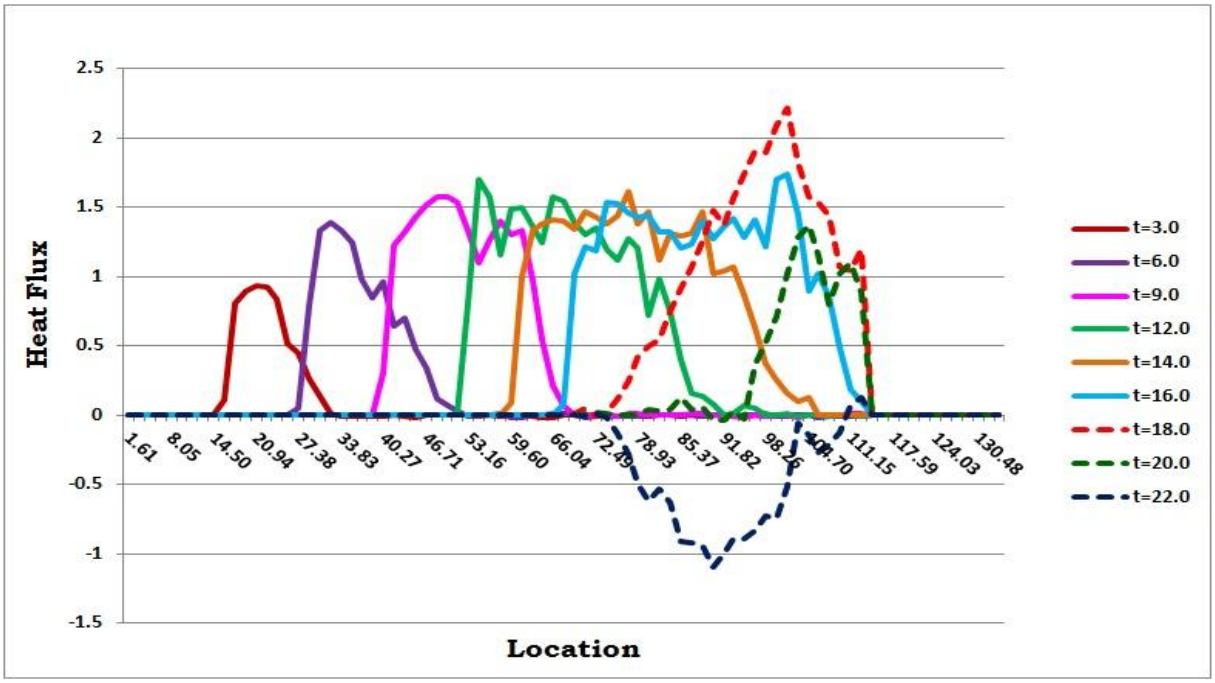

Fig 3.6 Heat flux profiles in the gas flow domain generated by the propagating shock wave at various times.

Fig 3.6 shows that the heat flux exhibits a similar behavior to that of gas velocity, with both primary and secondary reflections observed. The heat flux increases as the shock hits the poles face, unlike the solid wall where less rise in the heat flux is observed due to the flow direction reversal process that takes place over the whole slab cross section. In the porous medium, only part of the flow changes direction and the other parts keep moving in the space between the poles and this leads to a higher heat convection process. As the secondary shock propagates and is reflected from the pole base there is a rise in the heat flux vector before the flow changes direction causing the heat flux to change direction accordingly.

3.2.6 Gas Normal stress on the pole face and pole base area

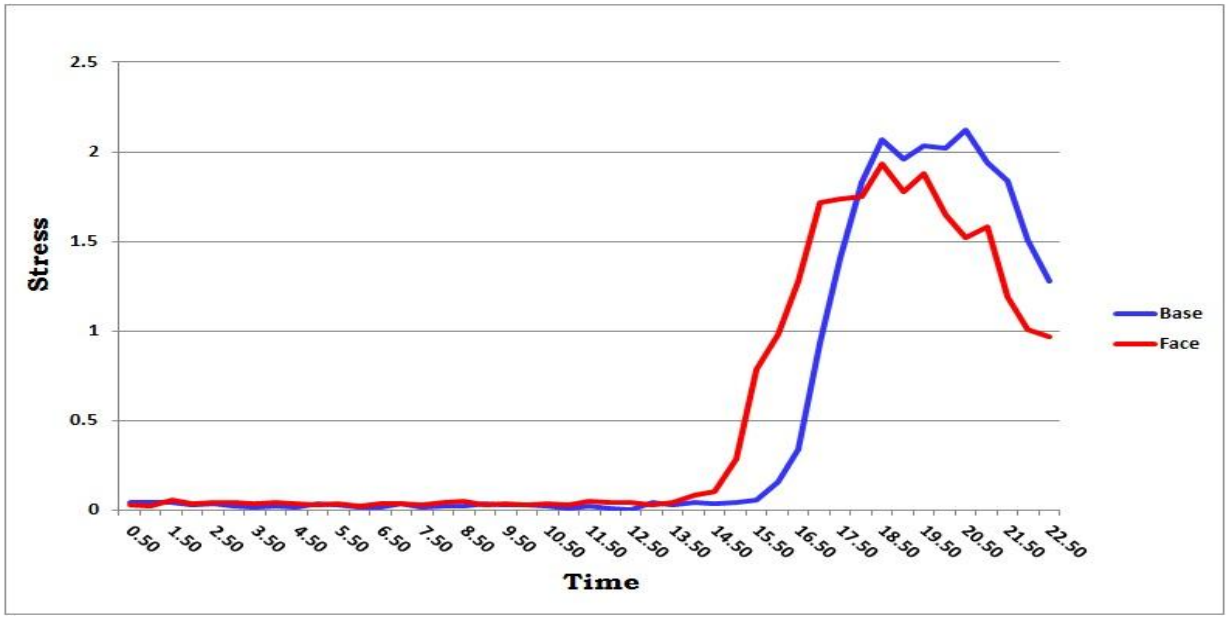

Fig 3.7 Gas normal stress on the pole face and the pole base area during shock impact

Figure 3.7 shows the gas phase normal stresses exerted on the poles face and on the pole base area during the primary and secondary shocks impulsive load on the solid structure: the primary shock impacts the poles face first followed by secondary shock impact on the base area. The

normal stress at the poles face area rises with time due to the primary shock impact which results in a partial reflection and partial transmission into the porous material. It decreases subsequently as the shock travels upstream and the flow changes direction. Besides, the normal stress at the poles base area also rises due to the secondary shock impact. Then it decreases as the shock is fully reflected and the flow changes direction within the pores.

The normal stress rise at the face is different in magnitude from that at the base and it occurs earlier than that at the base. The normal stress increase in each location depends on the gas density, piston velocity and porosity parameters: thickness, shape and length of the poles as well as the number of the poles and their placement. The area of the poles face and the poles base are varying depends on the porosity but both sum up to the total cross sectional area of the channel. In the case of 65% porosity the pressure rise at poles face is higher.

3.2.7 Normal stress and its impulse

The normal stress component of the solid structure before the shock impact, shown in fig. 3.8, oscillates around zero corresponding to an unstressed/unstrained state. Once the shock hits the structure there will be a rise in the normal stress component due to the transmitted stress before it starts decreasing as shock reflection takes place at the end of the target wall. The impulse is the time integral of forces acting on the wall, i.e. the normal stresses will exert impulsive forces on the solid structure. Numerical integration was used by applying the trapezoidal rule over the time period from the instant the piston starts moving till the end of simulation. When the shock wave hits the solid wall, the force exerted on the solid wall particles depends on the shock wave pressure and time duration of the shock impact. The impulsive force is the integral of the normal force that is normal stress multiplied by the wall area over the time duration. Since the pressure

gradient across the shock wave is large and during reflection there is a pressure buildup on the solid wall, the impulse significantly increases when the shocks hits the wall and during reflection, see fig 3.8 and fig 3.9.

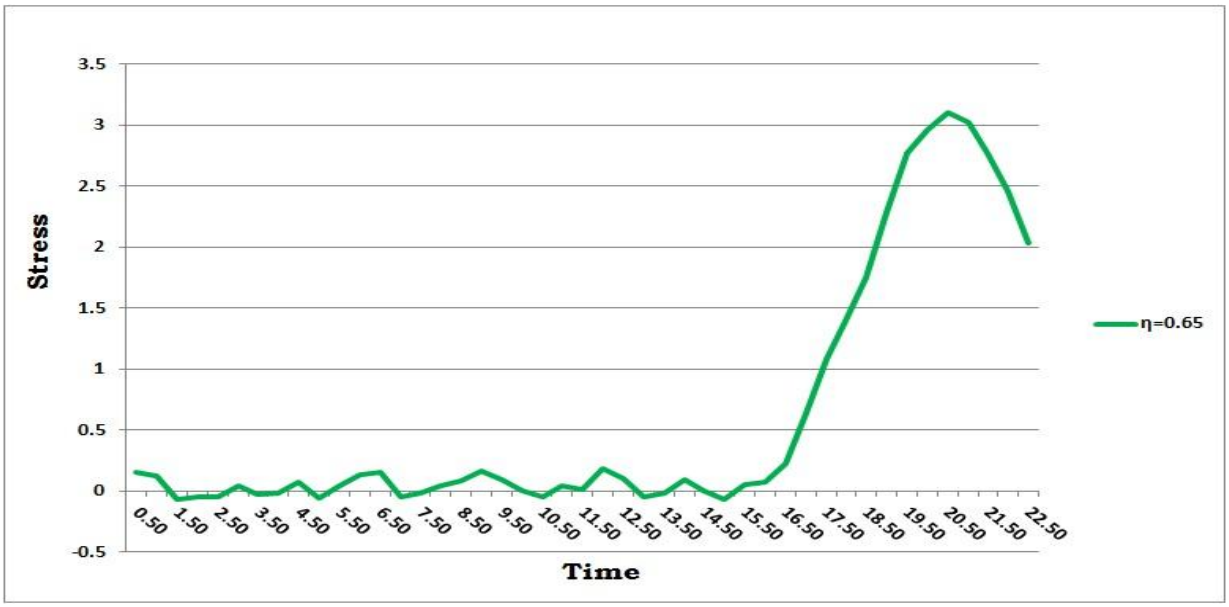

Fig 3.8 Variation of the normal stress in solid wall during shock impact

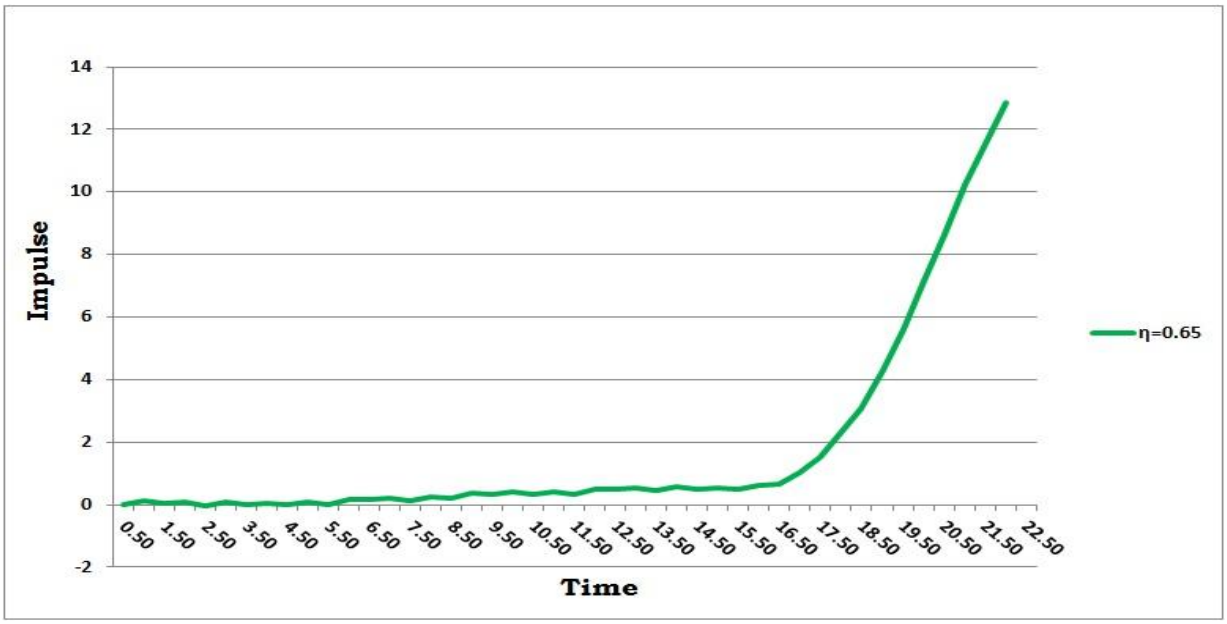

Fig 3.9 Variation of the solid wall normal impulse during shock impact

3.3 Solid properties

3.3.1 Average shear modulus

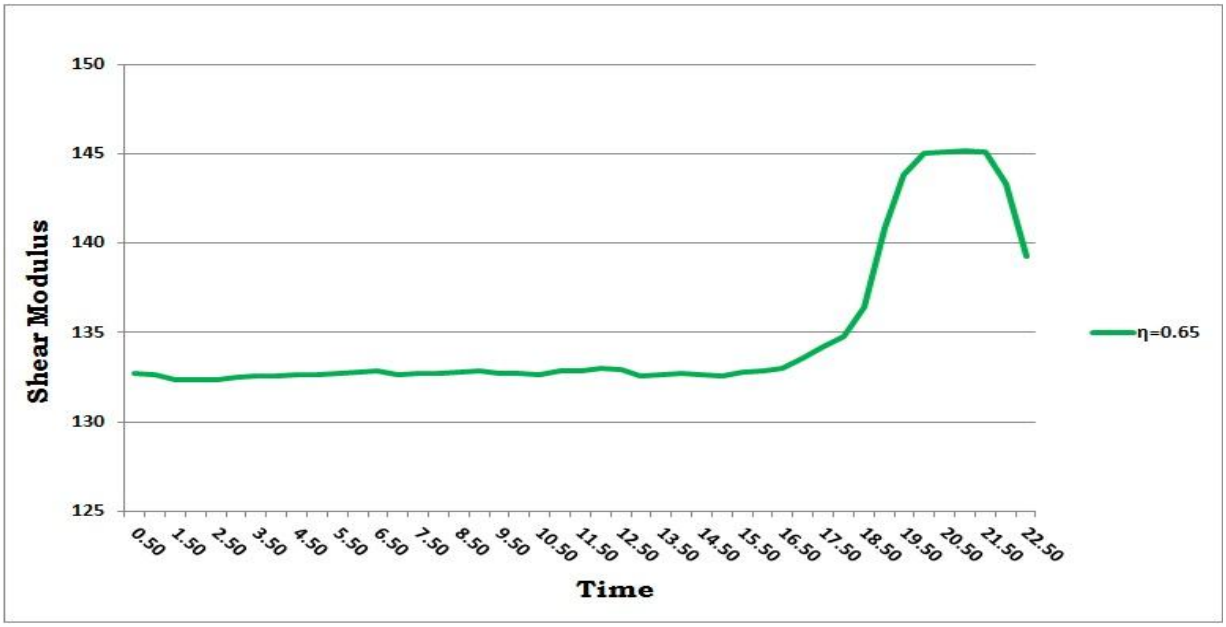

Fig 3.10 Variation of the solid wall average shear modulus during shock impact

Fig 3.10 shows that before the shock hit the solid wall, the shear modulus oscillates around a mean value. Once the shock hits the wall and the stress is transmitted in the solid, it reaches a maximum value before it goes back to its average value before the shock impact. The rise in the shear modulus due to strain rate effect is about 10% which is almost the same value observed in the solid wall case, see fig. 2.15.

3.3.2 Average bulk modulus

Referring to fig 3.11, before the shock hits the solid wall, the bulk modulus oscillates around a mean value. Once the shock hits the wall and it is transmitted in the solid, it reaches a maximum value before it goes back to its average initial value before the shock reflection takes place. The

rise in the bulk due to strain rate effect modulus is about 7% only, a value that is almost the same to the one observed in the solid wall case, see fig 2.17.

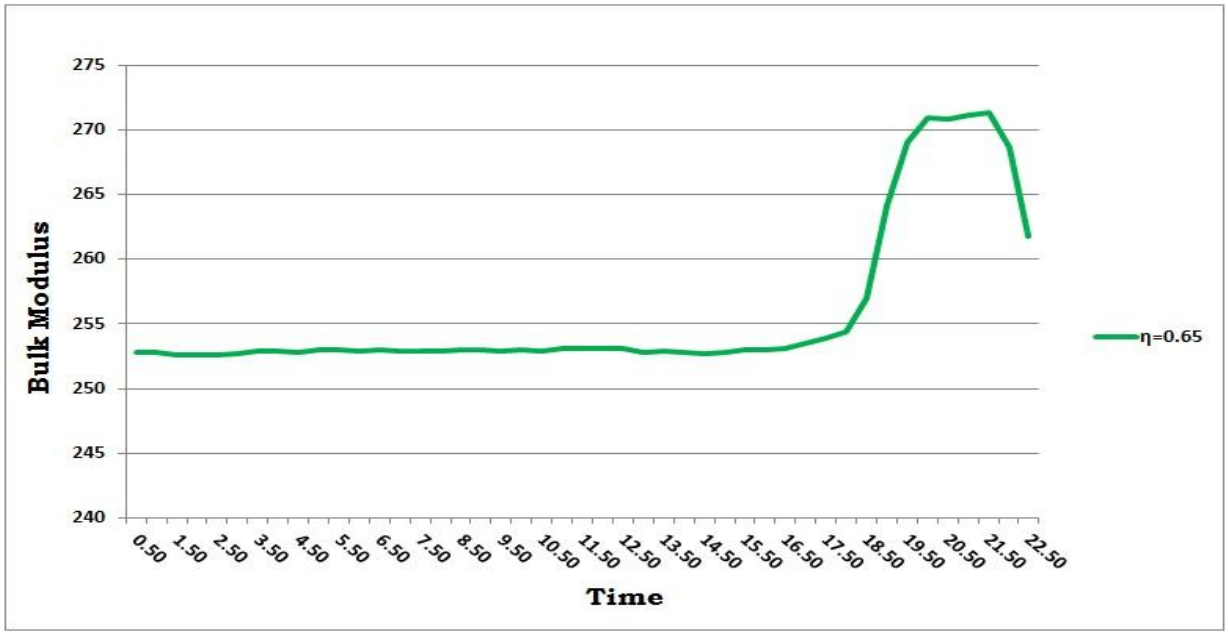

Fig 3.11 Variation of the solid wall average bulk modulus during shock impact

3.3.3 Local displacement

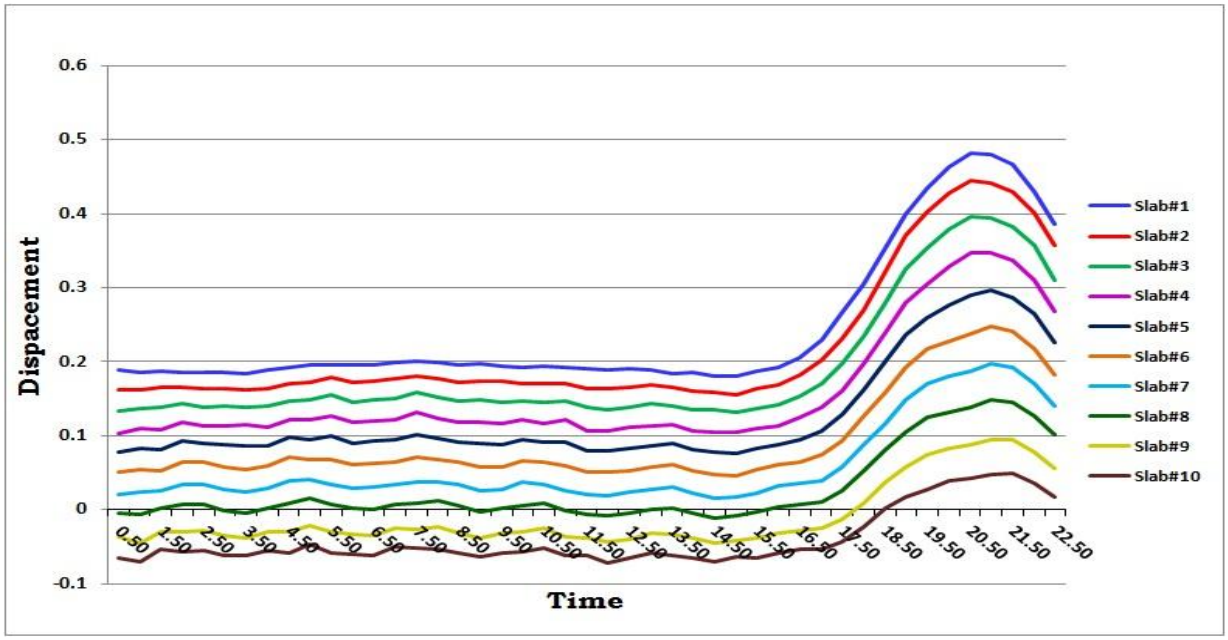

Fig 3.12 Variation of the local displacement of the solid wall during shock impact

Fig. 3.12 shows the local displacement due to the shock impact and transmission inside the solid wall target. At equilibrium, the solid particles are vibrating around the corresponding mean locations; the local displacement of solid particles close to the holding wall is negative due to the repulsive forces exerted by the holding wall particles. Further particles from the holding wall are less affected by these repulsive forces and they are free to move in the positive direction with their local displacements being higher the further from the holding wall. As the shock is transmitted through the solid wall, solid particles possess more kinetic energy and due to the shock impact, the solid wall will be compressed and the solid particles will deviate from their equilibrium positions: particles close to the gas channel will have higher local displacement than those closer to the holding wall. After the shock reflection over the end wall takes place, particles tend to attain their equilibrium positions. The maximum displacement observed is less than that of the solid wall case due to the decrease in the shock impulse on the structure, see fig 2.19.

3.3.4 Average normal strain

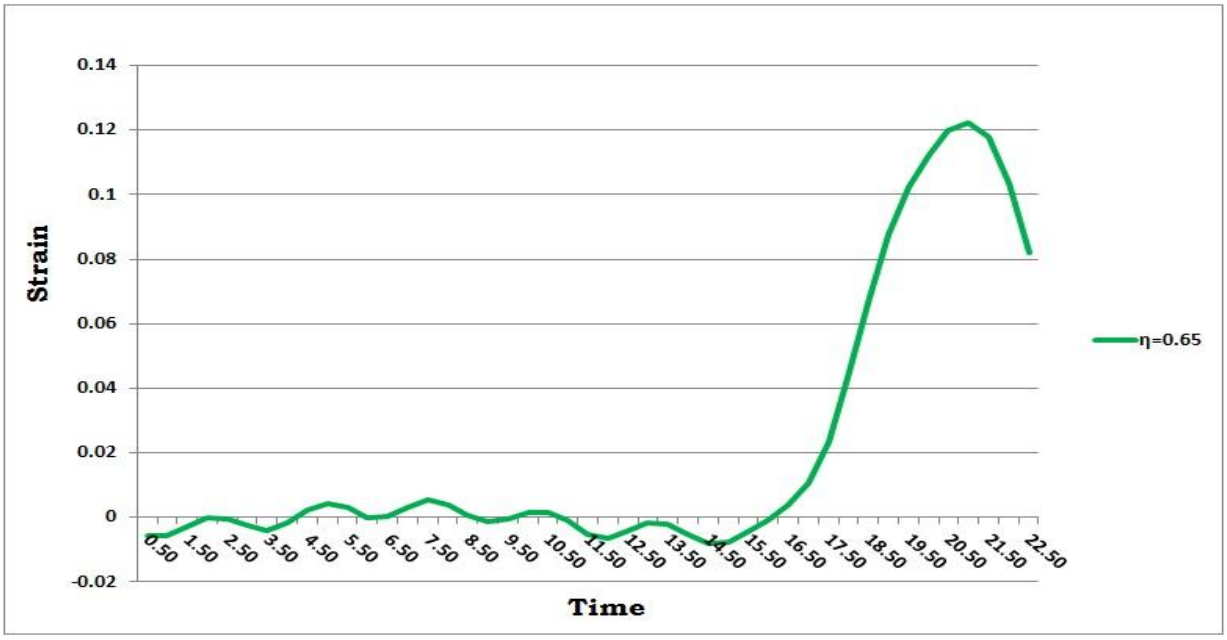

Fig 3.13 Variation of the average normal strain of the solid wall during shock impact

According to fig 3.13, an unstrained state is observed before the shock hits the porous wall. As the shock impacts the structure, the strain rises before it starts decreasing as the shock reflection takes place and gas flows back into the channel away from the solid structure. The maximum strain value is less than that of the solid wall case due to the decrease in the shock impulse on the structure, see fig 2.20. The strain depends on the piston velocity and gas density as well as the porosity parameters.

3.3.5 Instantaneous change in energy in the solid Wall

The change in energy of the solid structure is computed by calculating the work done by the structure deformation. Fig 3.14 shows that during the shock impact there is a rise in the energy change in the solid structure due to energy exchange between gas particles and solid particles which results in an increase in stress and strain in the solid structure. As the shock reflection takes place, the structure tends to restore its unstrained state.

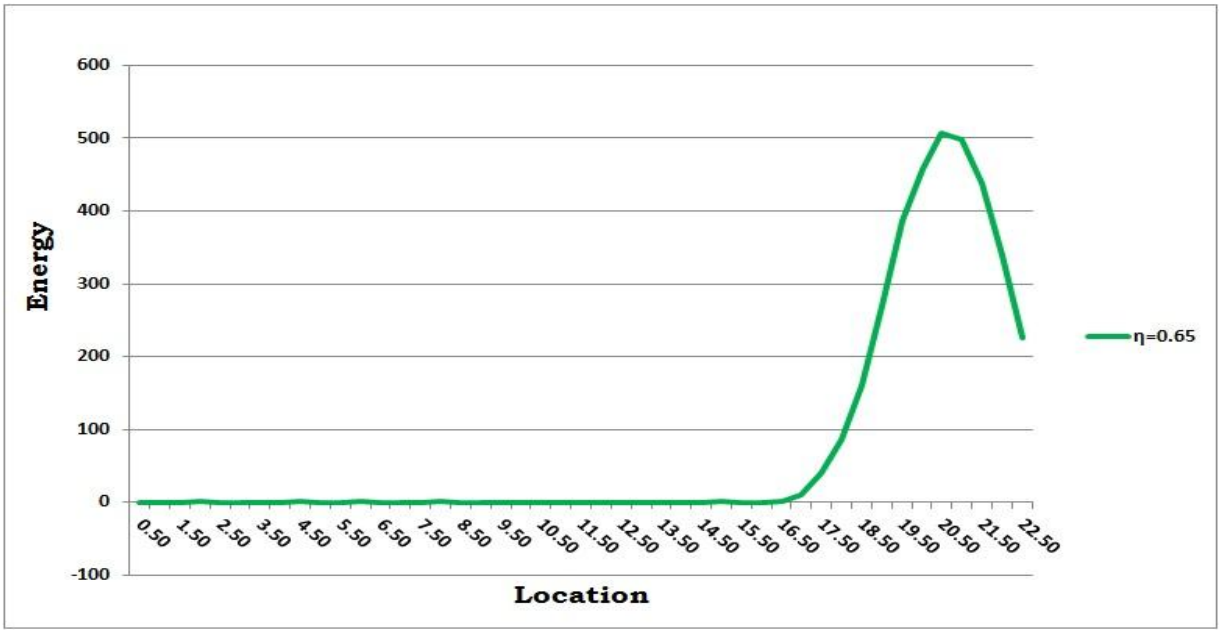

Fig 3.14 Variation of the instantaneous change in energy of solid wall particles during shock impact

3.4 Effect of porosity on solid structure

3.4.1 Normal stress and its impulse

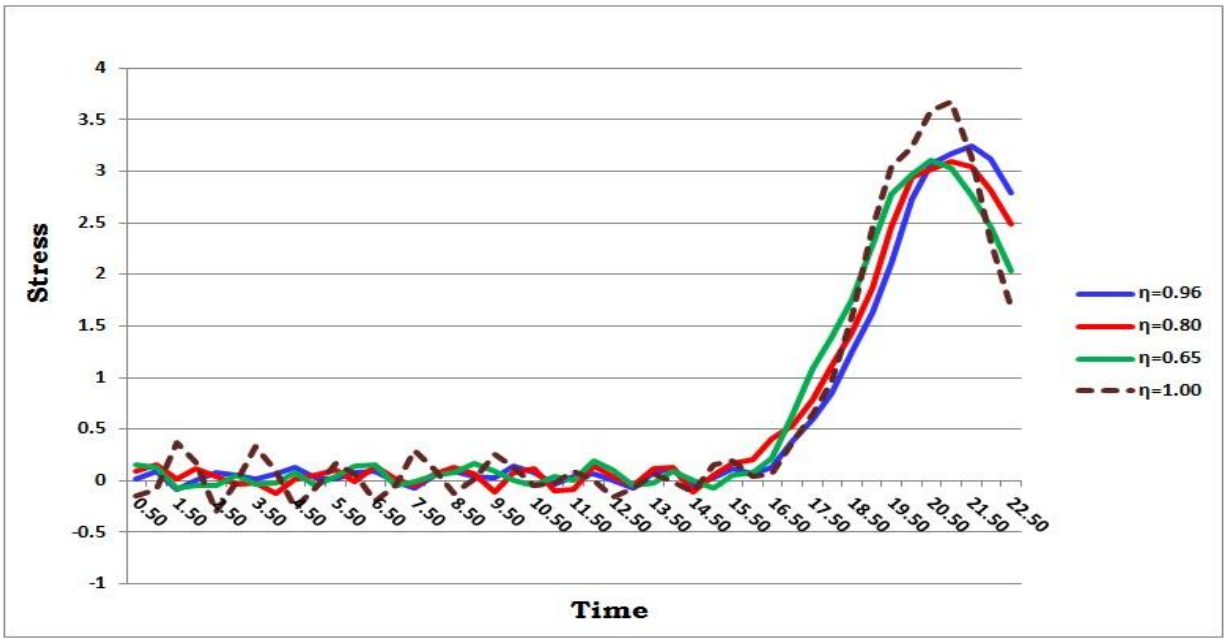

Fig 3.15 Effect of the porosity on the solid wall normal stress

The normal stress response to shock impact exhibits the typical increase behavior when the shock wave hits the solid wall and the pressure builds up during shock reflection. Then the normal stress decreases when the flow changes direction towards the piston away from the solid structure. The maximum rise in the solid structure is proportional to porosity. Porosity also affects the arrival time of shock impact where the time delay increases with the increase of porosity. In addition it affects the rate of loading i.e., stress build up with time. It appears to be decreasing with decreasing porosity. The case of solid wall structure (100% porosity) has the highest rise and the steepest curve. The time integral of the normal stress components computes the impulse of the shock on the solid structure. This impulse is inversely proportional to porosity,

while there is a slight difference in impulse in all case. However, the solid wall case will always have the highest impulse by a very small amount (see fig 3.15 and fig 3.16).

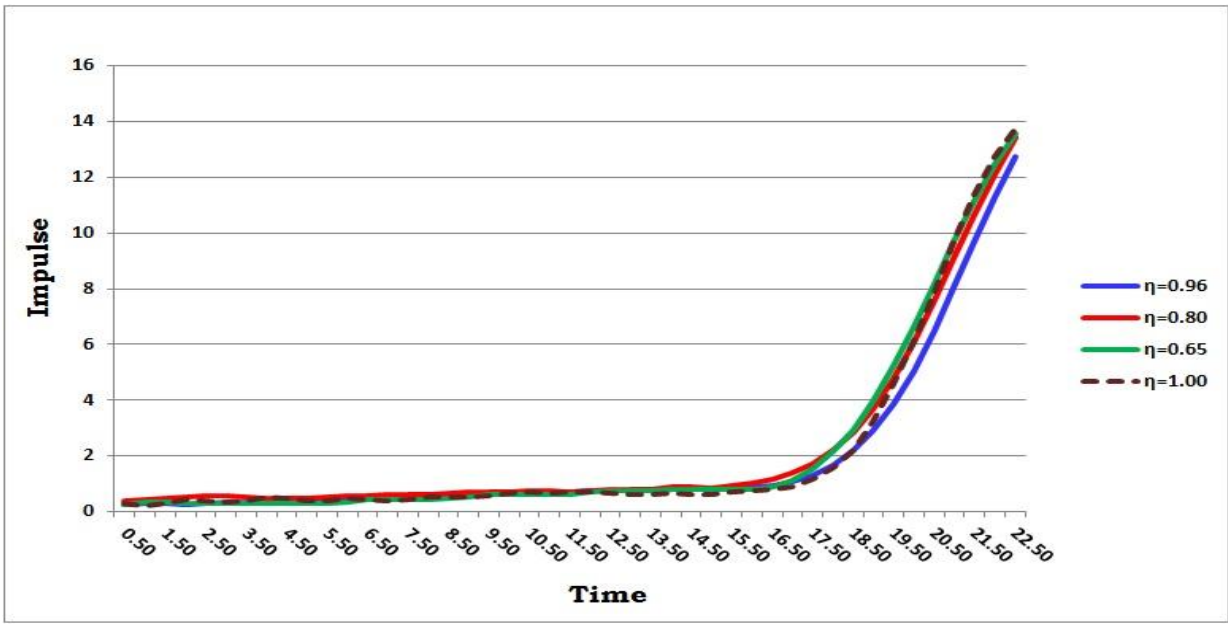

Fig 3.16 Effect of the porosity on the normal impulse on solid wall

3.4.2 Average normal strain

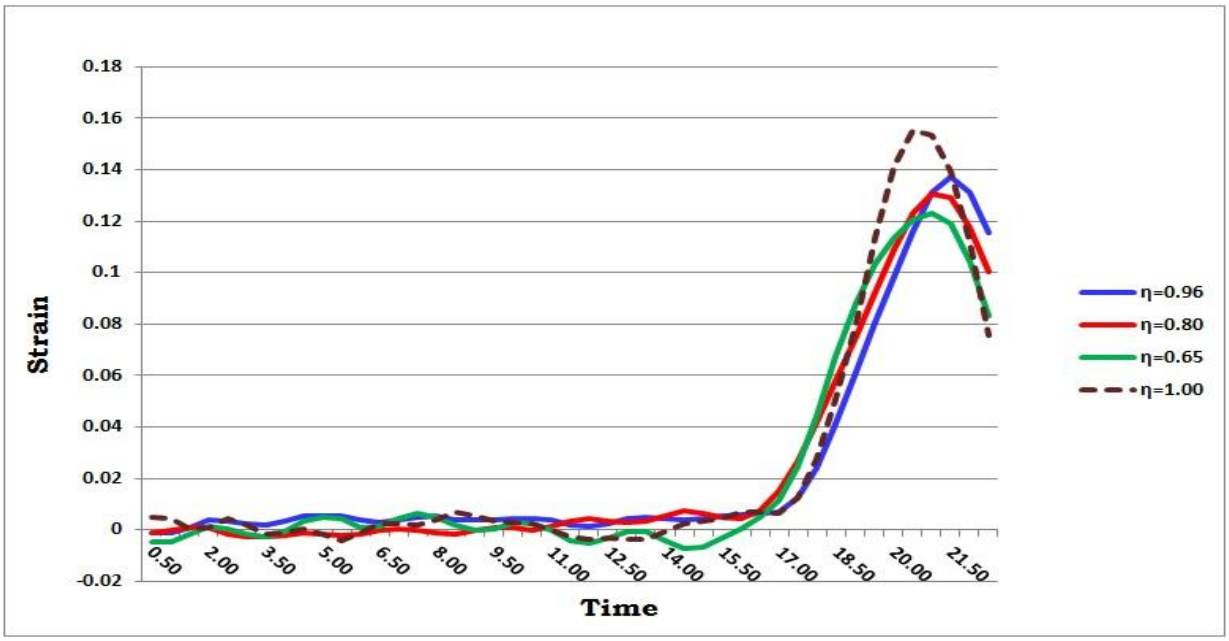

Fig 3.17 Effect of the porosity on the average normal strain of the solid wall

Fig 3.17 shows the spatially averaged strain as a function of time during the shock impact. An unstrained state is observed before the shock hits the porous wall; as the shock impacts the structure the strain rises before it starts decreasing as shock reflection takes place and the gas flows back into the channel away from the solid structure. The maximum strain appears to be inversely proportional to the porosity. Similar to the case of stress, strain in the case of solid wall (100% porosity) has the maximum rise and the steepest curve. The porosity causes a delay of the shock impact and consequently the time of shock reflection is extended, due to the flow traveling time from the face to the base of the poles.

3.4.3 Average shear modulus

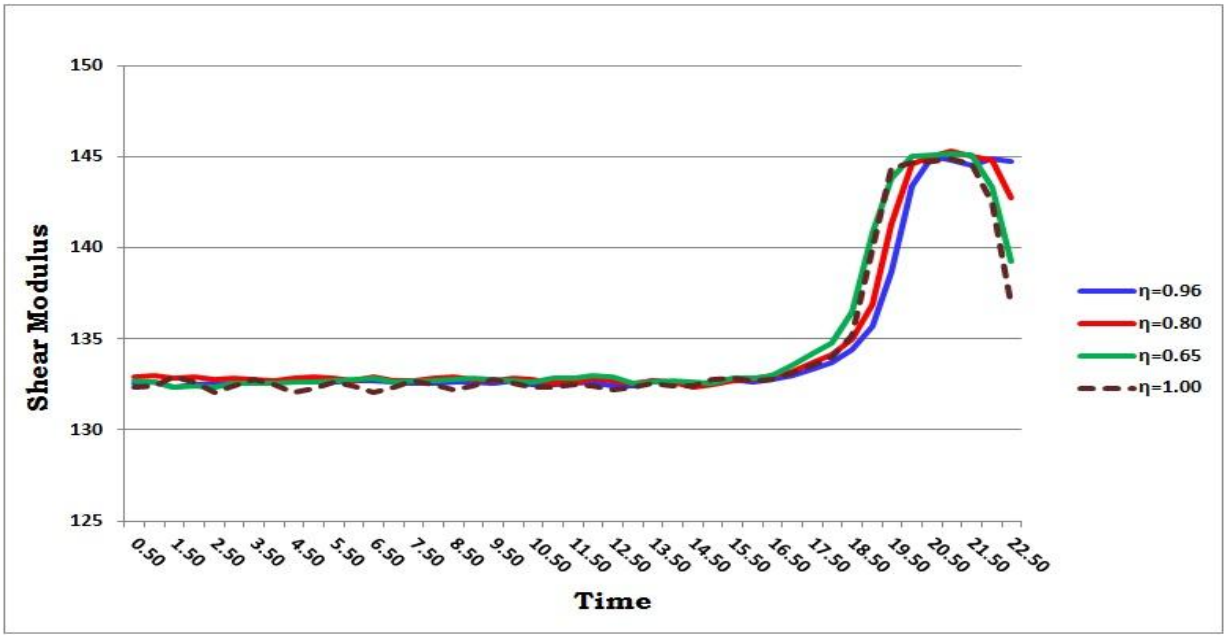

Fig 3.18 Effect of the porosity on the average shear modulus of the solid wall

Referring to fig 3.18, as the shock propagates in the gas channel, the average shear modulus oscillates around a mean value before the shock hits the solid structure. After the impact, it goes up to a maximum value before it restores back to its initial average value observed before the

shock reflection takes place. A 10% increase in the shear modulus due to stress-stain rate effect was observed in all cases. These data also show the effect porosity has in delaying the shock impact and consequently extending the time of shock reflection.

3.4.4 Average bulk modulus

Fig 3.19 shows a comparison of the bulk moduli computed in the cases of different porosities. As the shock propagates in the gas channel, the average bulk modulus oscillates around a mean value before the shock hits the solid structure; after the impact, it goes up to a maximum value before it retreats to its average value before shock reflection takes place. A 7% increase in the bulk modulus due to stress-stain rate effect was observed in all cases. The effect porosity has in delaying the shock impact and in extending the process of reflection is also evident here.

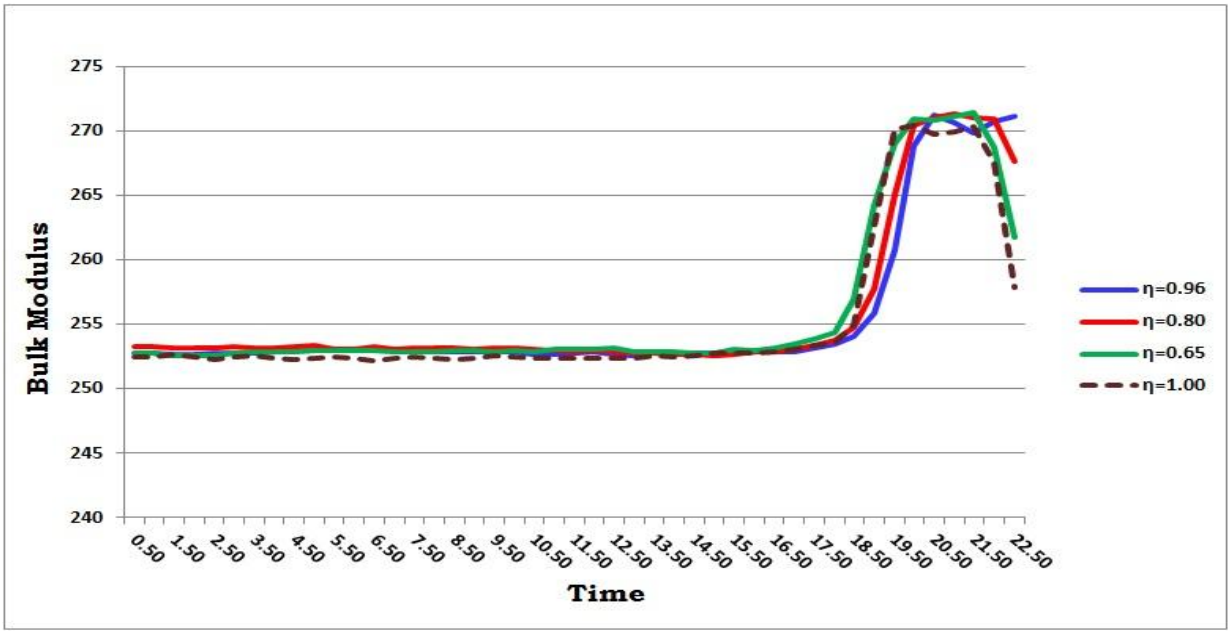

Fig 3.19 Effect of the porosity on the average bulk modulus of the solid wall

3.4.5 Instantaneous change in energy in the solid wall

The change in energy of the solid structure is computed by calculating the work done by the structure. It was shown earlier that both stress and strain rises during shock impact are proportional to the porosity. Fig 3.20 shows that the instantaneous change in the energy in the solid structure is also proportional to porosity; however, the solid wall case will always have higher stress and strain and consequently will have higher energy gain during the shock impact. The time delay due to the presence of poles is also observed here. The higher the porosity, the higher and steeper the change during shock impact.

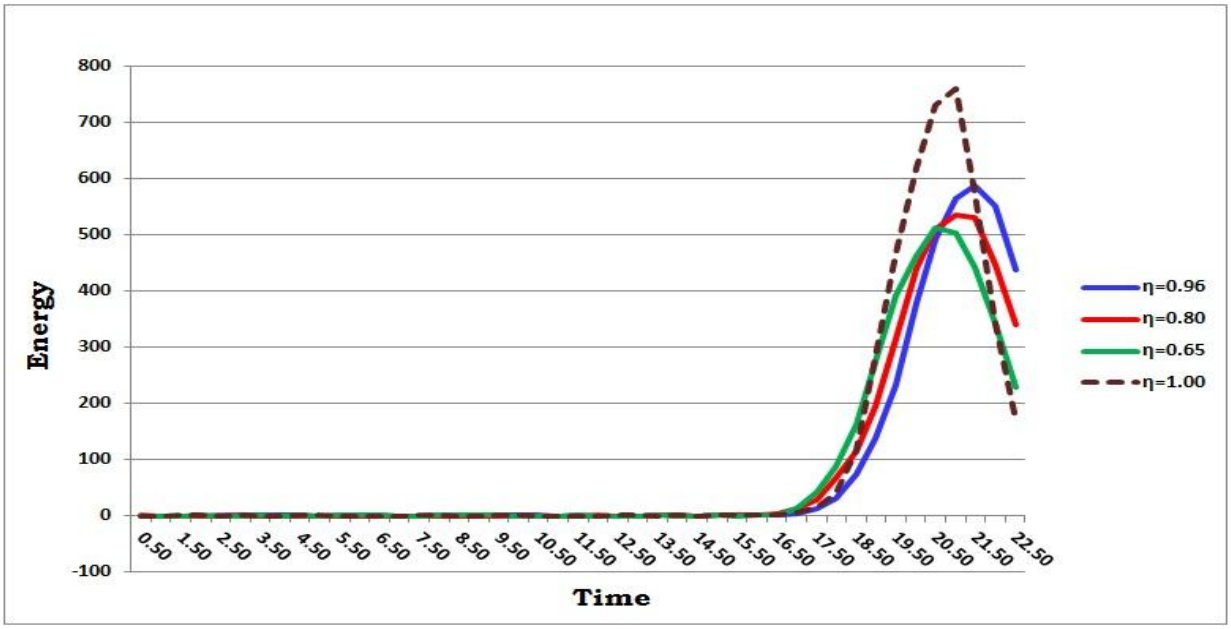

Fig 3.20 Effect of the porosity on the instantaneous change in energy of solid wall particles

3.5 Graded poles geometry

In this case the porosity along the length of the poles is not constant and changes gradually. Straight poles that were attached to the solid wall in the previous section were replaced by poles of varying cross section. These poles are attached to 20 layers of solid particles that occupy an axial length of $16.11\psi_w$. The removed particles are compensated by the ghost particles and the total number of particles of the structure remains the same regardless of the number and size of the poles. Referring to fig 3.21, there are three rows of poles with three poles in each row; this sums up to nine poles. The first and third rows are in line with each other and the second is offset by half the distance between any two rows. All the poles have the same shape and depth. The pole radius increases linearly from $0.2\psi_w$ at the tip to $4.0\psi_w$ at the pole's base and the porosity is linearly increasing from 0.77% to 52%. The average porosity is calculated by dividing the number of the solid particles forming the poles by number of the ghost and the solid particles contained in the porous section. The resulting average porosity is 80%.

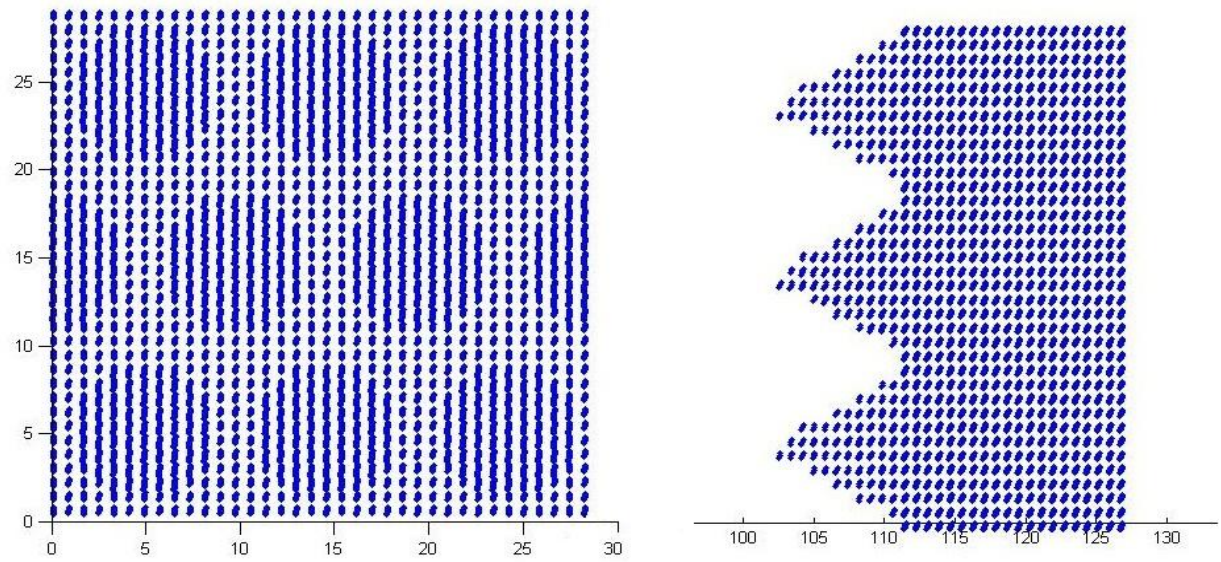

Fig 3.21 Schematic view of graded poles attached to solid structure.

3.6 Mixed poles geometry

In order to better understand the effect of various porosity parameters on the dynamics of shock waves and their effect on the solid structure two other cases were simulated:

i. The graded poles (yellow) in fig 3.22 were replaced by straight poles.

ii. The increasing thickens graded poles (yellow) in fig 3.22 were replaced by decreasing thickens graded poles as illustrated in fig 3.23.

In all cases, the average porosity was 80% and initial gas density was set to $0.0298\psi_w^{-3}$. After equilibration the piston was accelerated and moved at constant speed of 4.0. The shock wave was formed and propagated. Once the shock hits the solid wall, the piston was stopped.

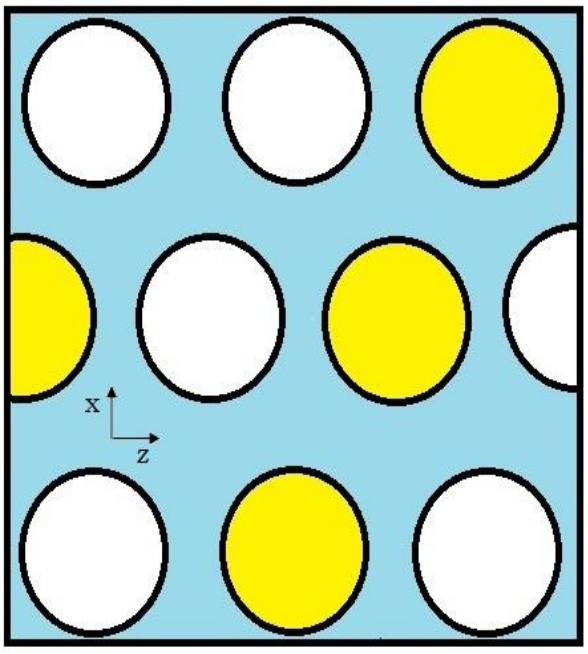

Fig 3.22 Poles distributed over the solid structure.

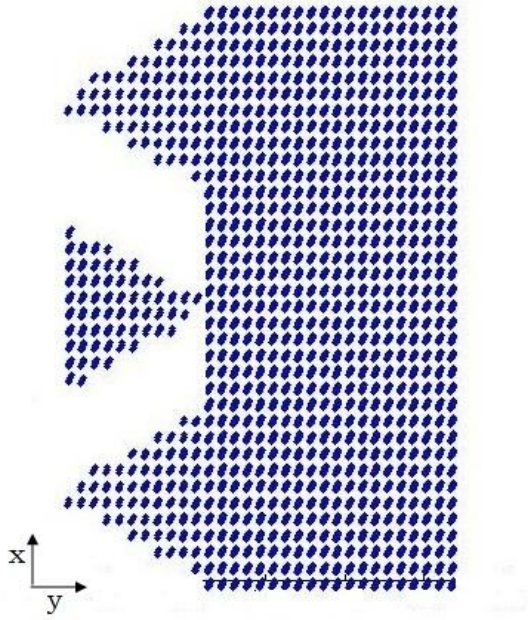

Fig 3.23 Increasing and decreasing thickness graded poles attached to solid wall.

Case #	Porosity	Poles Type
i	80%	Graded/Straight
ii	80%	Graded increasing/decreasing thickness
iii	80%	Graded increasing thickness
iv	80%	Straight
v	100%	No poles

Table 3.1 Summary of porous cases with different configurations

3.7 Effect of porosity configuration on solid wall

3.7.1 Normal stress and its impulse

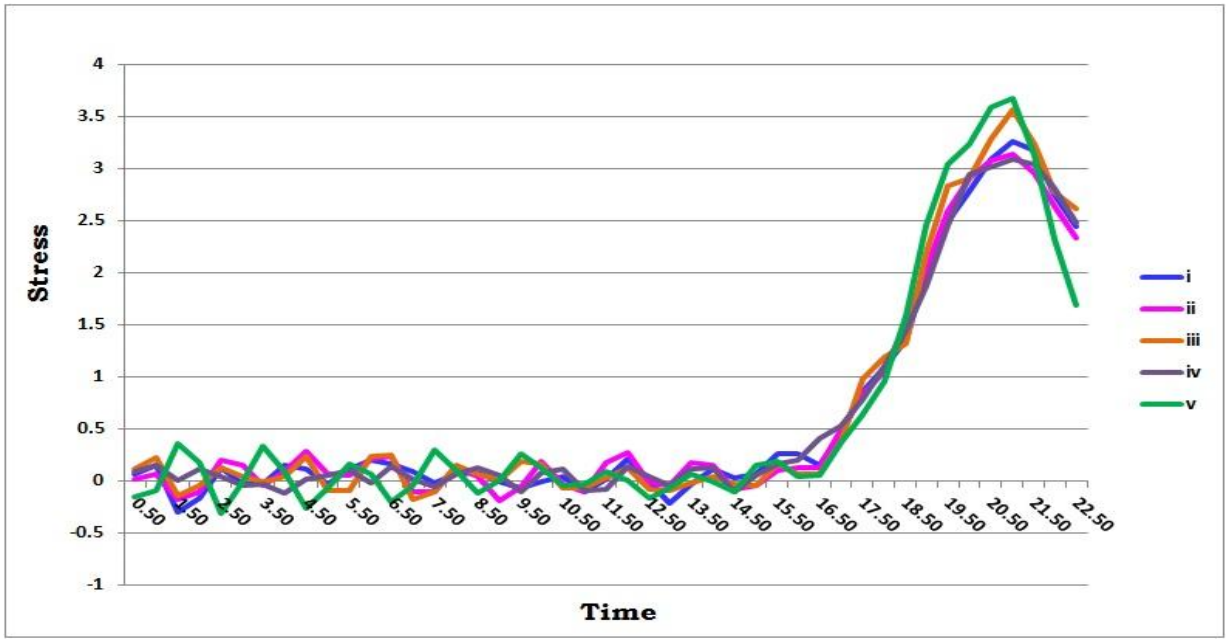

Fig 3.24 Effect of the porosity configuration on the wall normal stress

Referring to Fig 3.24, the normal stress response to shock impact has the typical increase behavior when the shock wave hits the solid wall and when the pressure builds up during the

shock reflection; then the normal stress decreases when flow changes direction and propagates back into the gas channel away from the solid structure. The use of graded poles geometry caused higher increase in normal stress than that of any porous case and it was close to that of the solid wall case (100% porosity). As it illustrated in fig 3.25, the case of straight poles had the lowest normal stress increase and it was very close to those of the mixed geometry cases. On the other hand, impulse was very comparable in all cases with slight rise in the graded poles and solid wall cases.

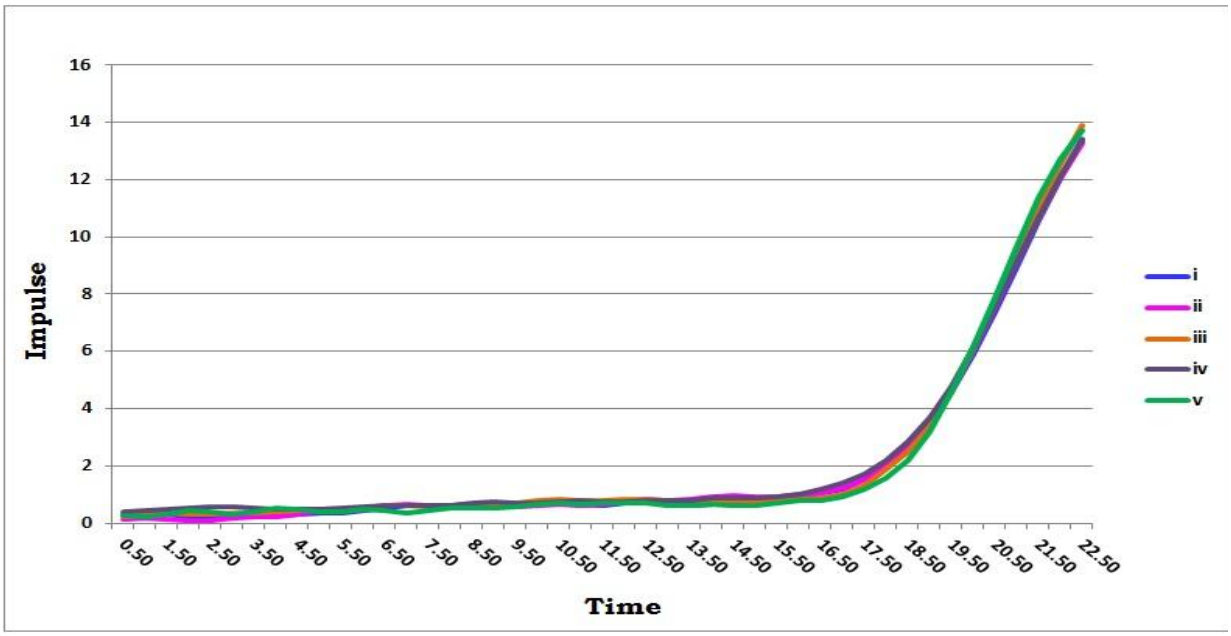

Fig 3.25 Effect of the porosity configuration on the normal impulse on solid wall

3.7.2 Average normal strain

Fig 3.26 shows that an unstrained state is observed before the shock hits the porous wall. As the shock impacts the structure, the strain rises before it starts decreasing as shock reflection takes place and gas flows back into the channel away from the solid structure. The normal strains in all

porous cases were comparable and much lower that of the solid wall case. The case of graded poles geometry caused slightly higher increase in normal strain than that of any porous case.

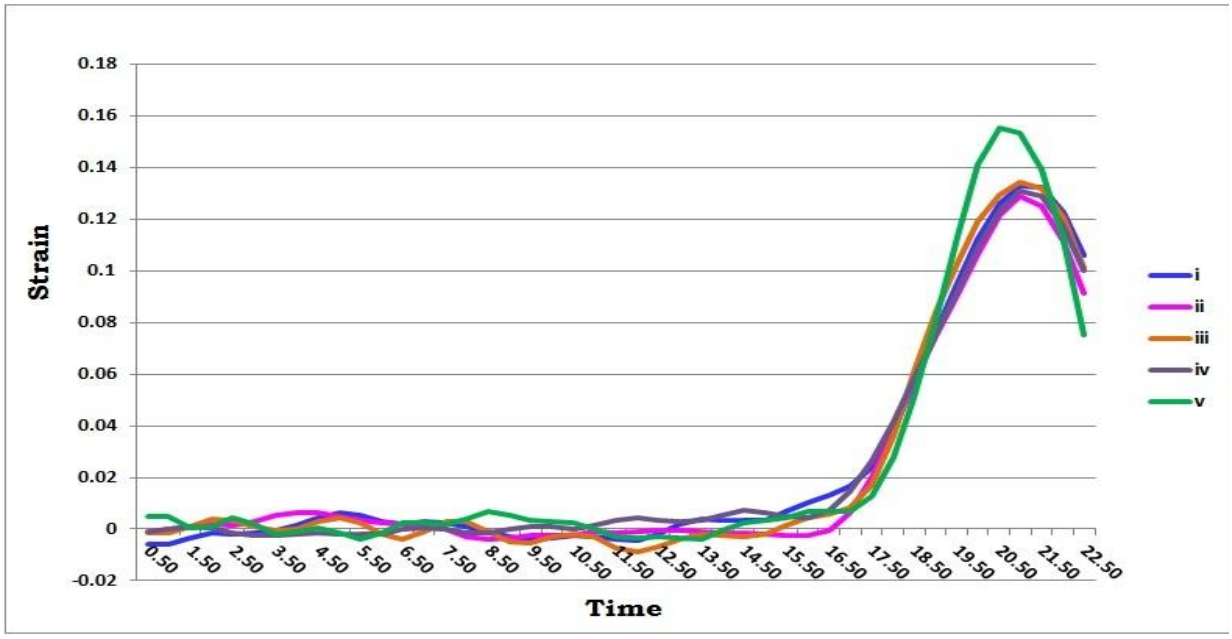

Fig 3.26 Effect of the porosity configuration on the wall normal strain

3.7.3 Average shear modulus

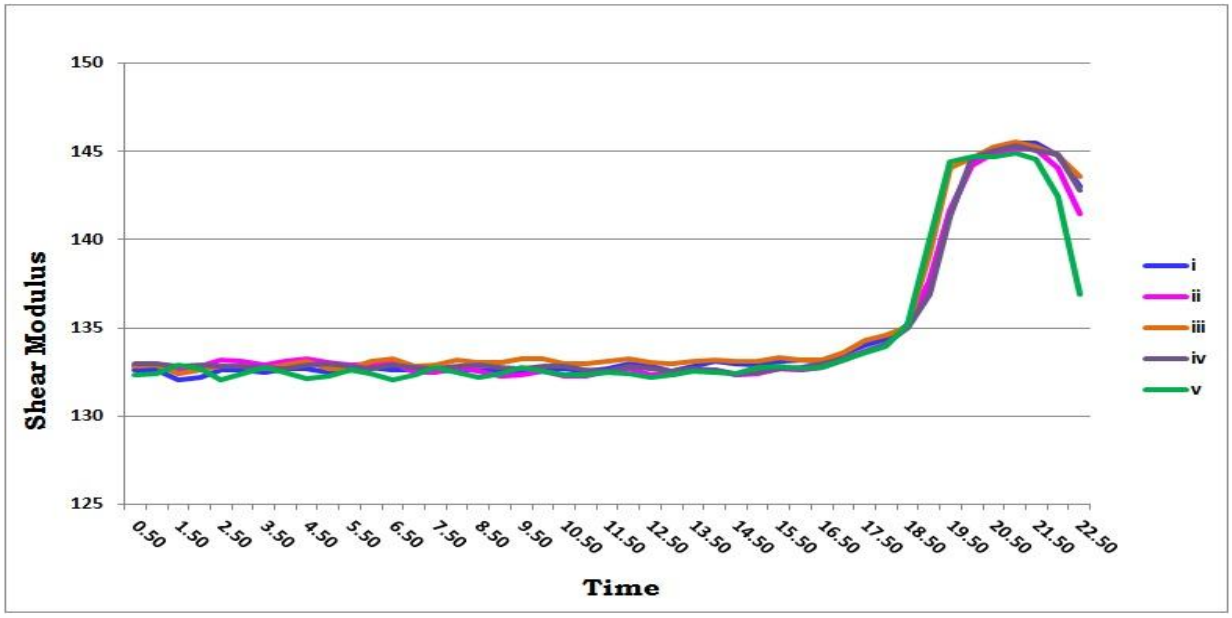

Fig 3.27 Effect of the porosity configuration on the average shear modulus of the solid wall

Referring to fig 3.27, as the shock propagates in the gas channel, the shear modulus fluctuates around a mean value before the shock hits the solid structure. Immediately following the impact, it achieves a maximum value before it decrease to its average value before the shock reflection takes place. A 10% increase in the shear modulus above its equilibrium value is observed due to high stress-stain rate effect in all cases. The structure tends to attain its unstrained state after the end of the reflection process. Porosity causes decrease in the rate of shock loading of the target structure and consequently extends the time of shock reflection and time required to restore the equilibrium state.

3.7.4 Average bulk modulus

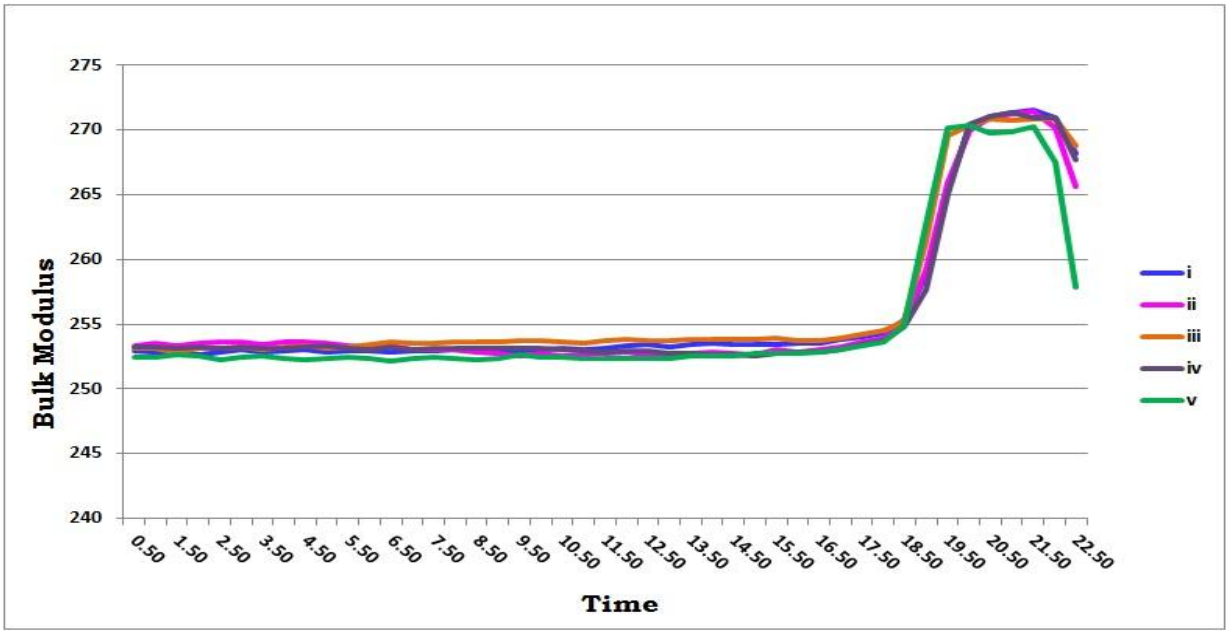

Fig 3.28 Effect of the porosity configuration on the average bulk modulus of the solid wall

As the shock propagates in the gas channel, the bulk modulus fluctuates about a mean value before the shock hits the solid structure. After the impact, it increases to a maximum value before it retreats to its average value before shock reflection takes place. A 7% increase in the bulk

modulus due to high-stain rate effect was observed in all cases, which disappears after reflection is over and the structure tends to attain to its unstrained state, see fig 3.28.

3.7.5 Instantaneous change in energy in the solid wall

The change in energy of the solid structure is computed in the way described earlier. Fig 3.29 shows that the pure solid wall case has the highest change in energy deposited in the target structure. the graded pole case has the highest change energy of all porous cases followed by the mixed geometry with straight poles, while the last two cases - mix graded (increasing and decreasing thickness) and straight pole case - have the lowest change in energy.

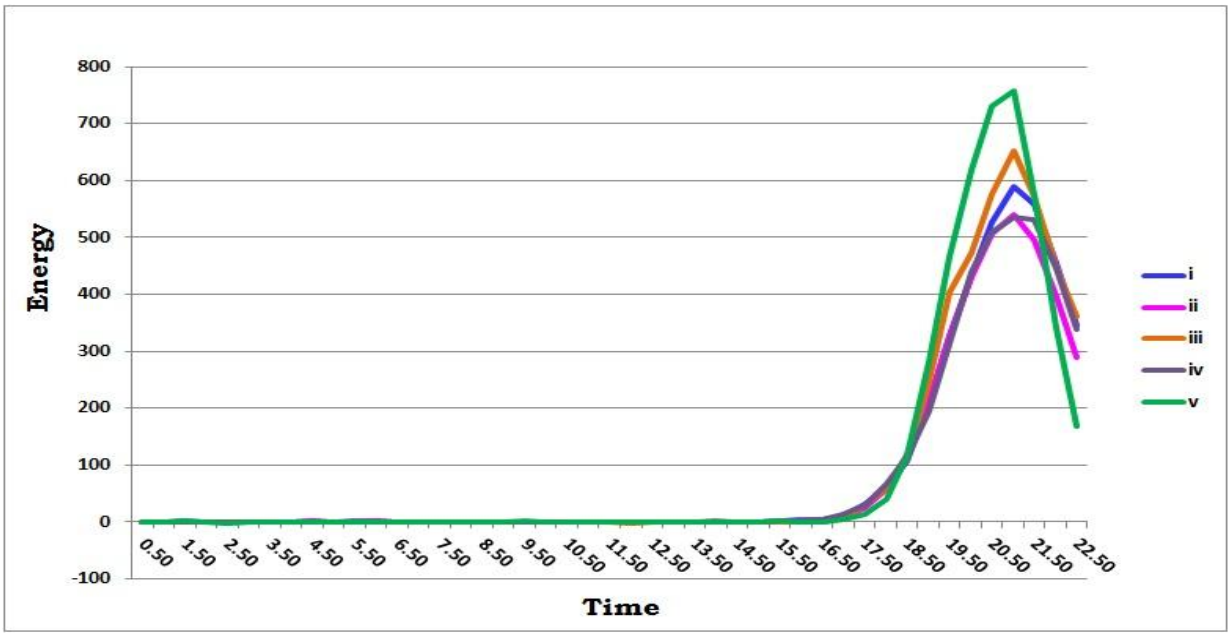

Fig 3.29 Effect of the porosity configuration on the change in energy of solid wall particles

Chapter Four

Stand Free Porous Structure

4.1 Model setup

In order to further explore the behavior of porous materials under a shock impact, the case of a free standing porous structure was investigated in the absence of a solid wall structure as target. The dimensions of the gas channel remained the same but the solid wall structure is now changed. Solid poles that are not attached to any other element are formed in the passage of the incident shock wave (see fig 4.1). Poles are placed in the normal direction of the shock wave propagation. A shock wave will be created and will propagate in the gas channel and will hit the front section of the freestanding poles. Part of the shock will be reflected and part will continue propagating into the space between the poles and eventually will exit the porous structure and will continue moving towards the end section of the gas channel where, finally, it will hit the holding wall and be reflected back into the gas channel.

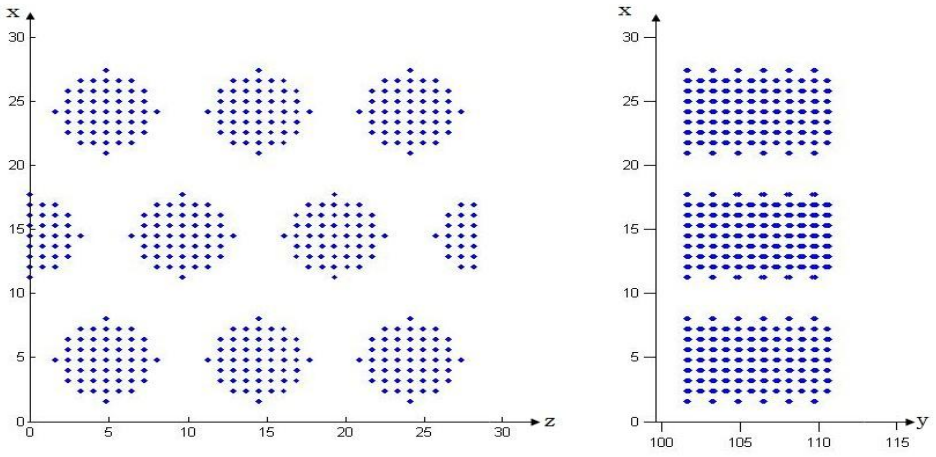

Fig 4.1 Schematic view of stand free straight poles

4.2 Thermal properties

A typical shock tube model that contains a freestanding straight pole arrangement with η=0.65 was formed. The system was equilibrated first before the piston was allowed to accelerate and then move to generate a shock wave that propagated in the gas channel.

4.2.1 Temperature

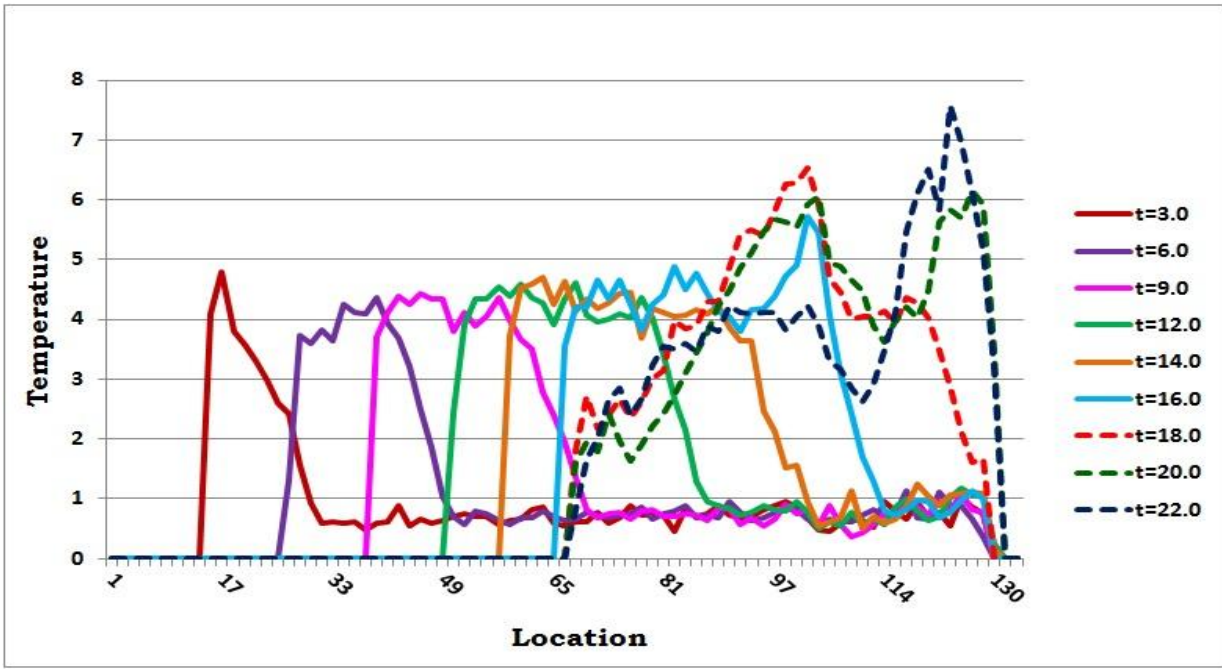

Fig 4.2 Temperature profiles in the gas flow domain generated by the propagating shock wave at various times.

Fig 4.2 shows that a shock wave was formed and developed as it was discussed earlier and it propagated in the gas channel till it hit the porous arrangement. Part of the shock hits the pole face and then reflected back towards the piston: this is the *primary reflection*, while the other part of the shock keeps propagating in the space between the poles then eventually exiting the porous structure and keeps moving in the end section of the gas channel. Finally, the flow will

hit the holding wall and be reflected back into the gas channel, designated as secondary reflection. Secondary reflection resulted in a higher temperature rise than that of the primary reflection; flow exiting from the porous section is still having high kinetic energy although its pressure is significantly dropped

4.2.2 Pressure

According to fig 4.3, the primary and secondary reflections were observed. Pressure rise due to the primary reflection is higher than that of the secondary reflection. The primary reflection results in a pressure level close to 1.7 which very close to that observed in the case the porous material is attached to the target wall (see figure 3.3).

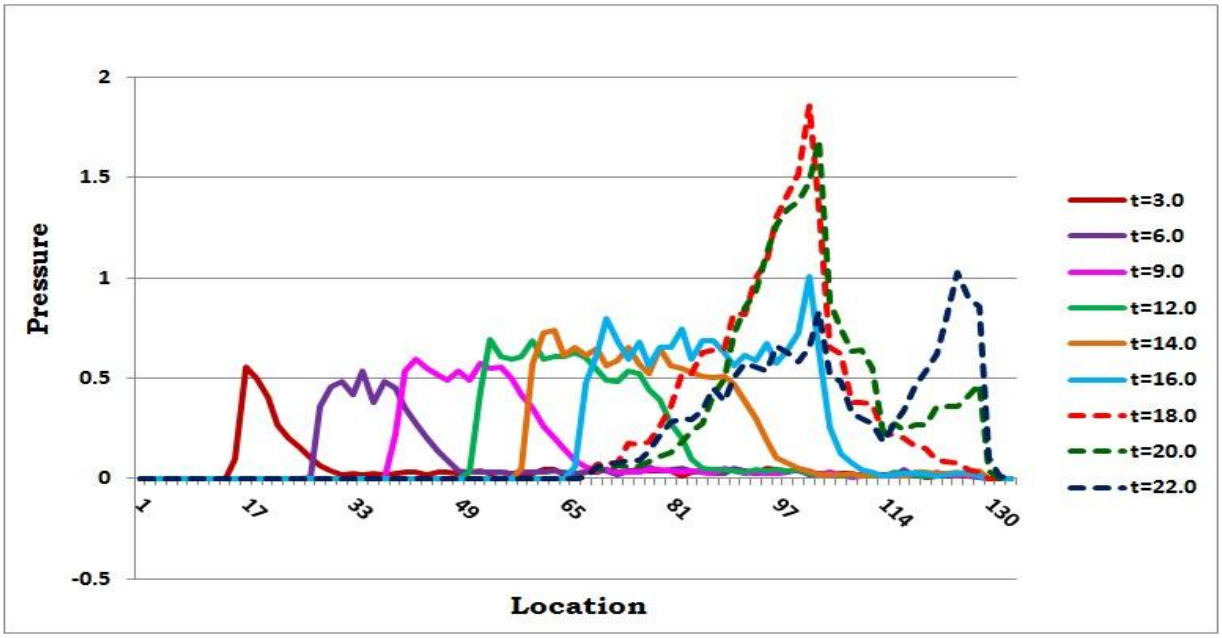

Fig 4.3 Pressure profiles in the gas flow domain generated by the propagating shock wave at various times.

4.2.3 Velocity

Figure 4.4 shows the gas velocity at various locations along the domain for various times. The passing of the propagating shock causes the gas particles to acquire a velocity. Shock span - distance between the shock front and the piston- is getting greater as the simulation time increases and the shock speed gets higher as it passes through the gas molecules. The primary reflection causes deceleration of part of the gas particles and eventually the flow formed by these particles changes direction towards the piston; however, the other part of the gas flow keeps moving between the poles till it exits the porous section and propagates towards the end section of the gas channel before it hits the holding wall where it changes direction towards the piston.

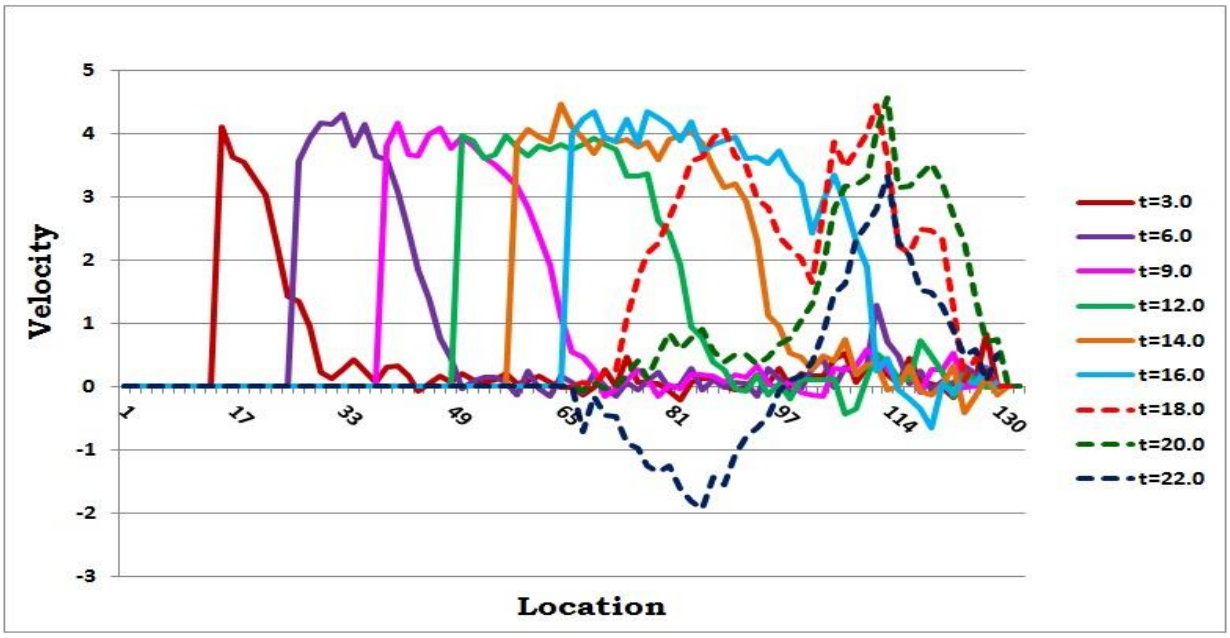

Fig 4.4 Velocity profiles in the gas flow domain generated by the propagating shock wave at various times.

4.2.4 Density

The primary and secondary reflections have an effect on all quantities of the flow. As shown in fig 4.5, the density at the poles face reaches a maximum value immediately after the passing of the primary reflected shock and then it decreases because the flow further expands as it propagates through the region between the poles. However, since the secondary reflection lags the primary reflection, the density is built up at the face area and is then followed by another increase due to the secondary reflection.

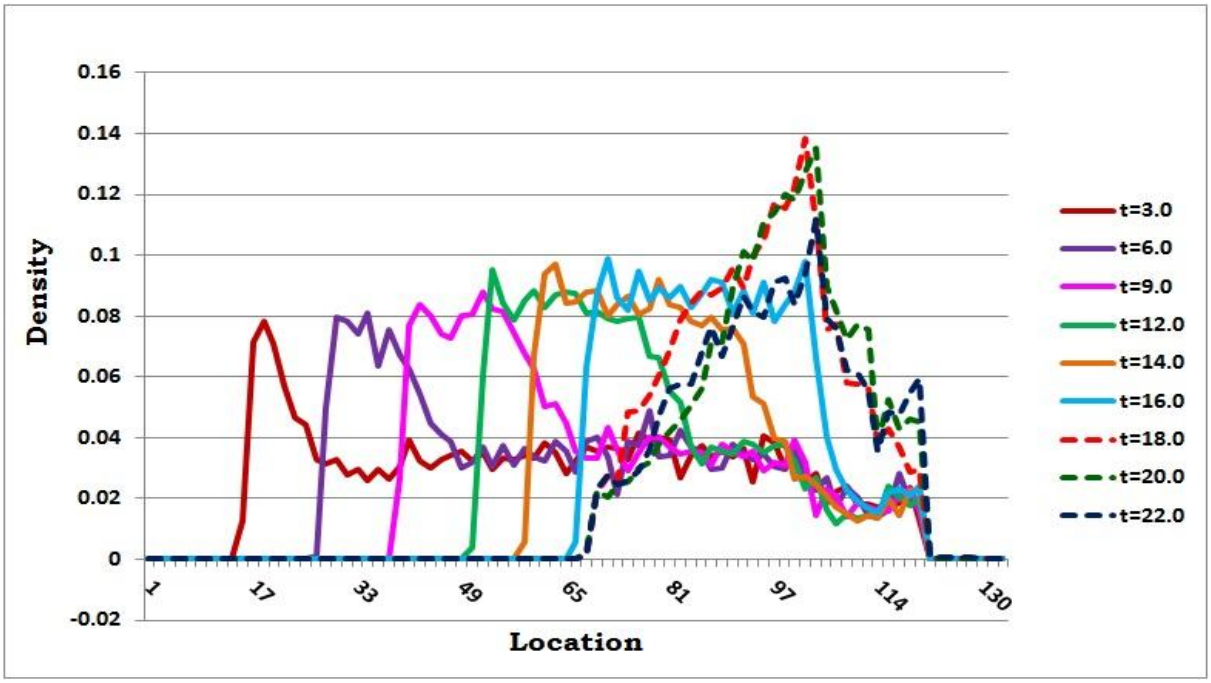

Fig 4.5 Density profiles in the gas flow domain generated by the propagating shock wave at various times.

3.2.5 Heat Flux

Fig 3.6 shows that the heat flux has a similar profile to that of the gas velocity, with both primary and secondary reflections observed. The heat flux increases as the shock hits the poles face,

unlike the solid wall where less heat flux rise is observed due to flow direction reversal that takes place over the whole slab cross section. In the porous medium, only part of the flow changes direction and the other parts keep moving in the space between the poles and this leads to a higher heat convection process. As the secondary shock propagates after it is reflected form the holding wall there is a rise in the heat flux vector before the flow changes direction causing the heat flux to change direction accordingly.

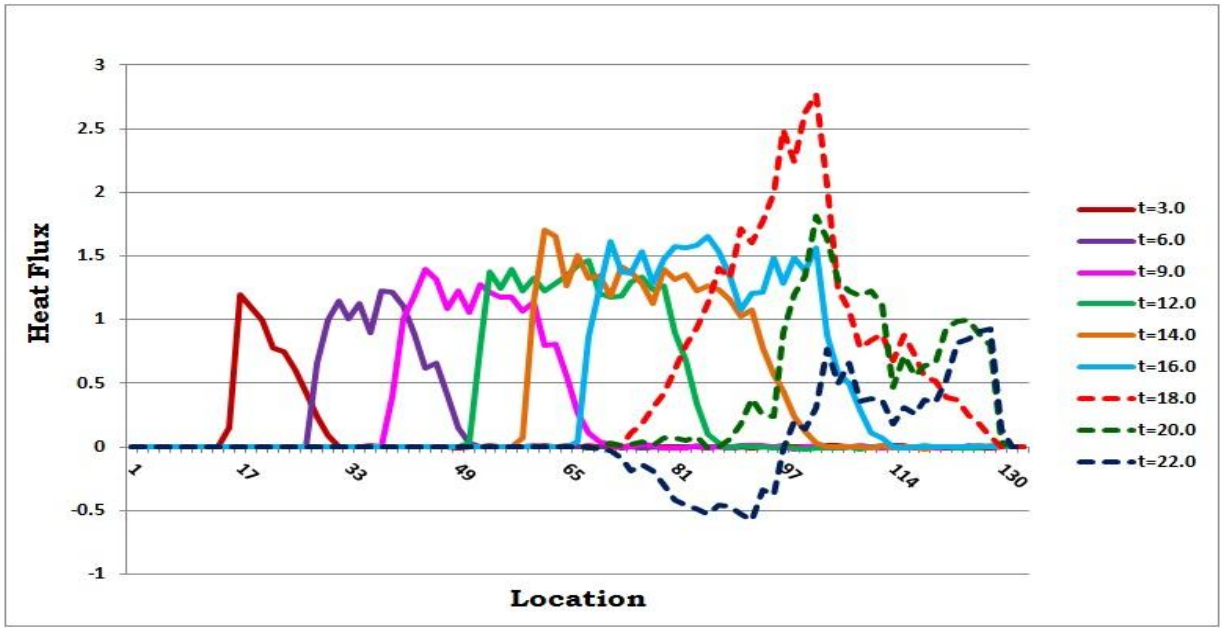

Fig 4.6 Heat flux profiles in the gas flow domain generated by the propagating shock wave at various times.

4.2.6 Gas pressure along the porous section

The flow of gas particles in a porous medium is always accompanied by a pressure drop of the flow due to friction and heat dissipation. When a shock wave hits the porous wall there will be a pressure difference between the front and back sections of the porous structure and therefore

pressure from the high pressure region will leak to the low pressure region. Fig 4.7 shows the variation of the gas pressure during shock impact at two locations inside the gas channel: *front section*, the slab adjacent to the porous structure, closer to the piston and *back section*, the slab adjacent to the porous structure, closer to the holding wall. Before the shock hits the structure, gas particles are at equilibrium. As the shock wave propagates inside the gas channel, shock reaches the front area before the back area, consequently, the pressure rises due to shock impact as well as shock reflection at front area. As time elapses, the flow exits the porous structure and the pressure rises at the back sections due to the reflection process that takes place at the holding wall. The pressure rise in both sections is highly dependent on porosity and its parameters: size, shape, placement, number and length of the poles. At η=0.65, the primary reflection is dominant and the pressure rise at the front area is much greater than that at the back area.

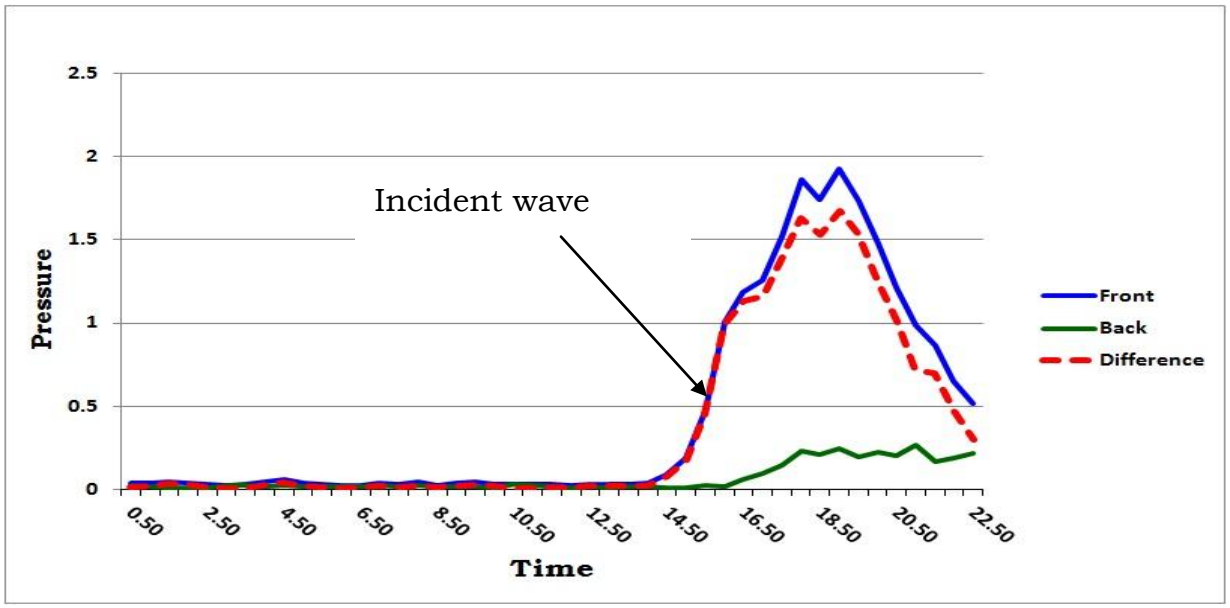

Fig 4.7 Variation of the gas pressure at the front and the back areas of the porous section during shock impact

4.3 Effect of porosity on front and back sections pressure

4.3.1 Pole front section pressure

According to fig 4.8 an equilibrium state is observed before the shock hits the porous structure. As the shock wave propagates inside the gas channel and the shock reaches the front area, the pressure rises due to shock impact as well as shock reflection at front area. The maximum pressure rise is inversely proportional to porosity. As porosity increases less face area is available and the primary reflection strength is smaller.

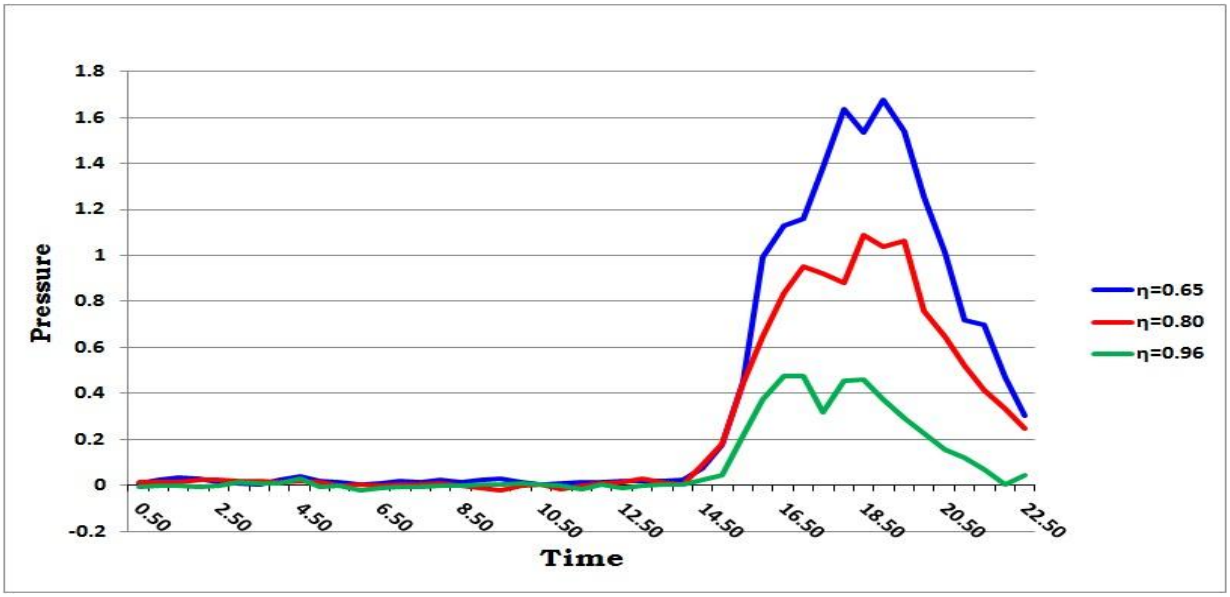

Fig 4.8 Porosity effect on the gas pressure at front area of the porous section during shock impact

4.3.2 Pole back section pressure

Fig 4.9 shows the pressure buildup at the exit of the free standing porous material. An equilibrium state is observed before the shock exits the porous structure. When the shock exits the porous section the pressure rises at the back section. The amount of the exiting flow is

inversely proportional to primary reflection strength and hence it is proportional to porosity. The gas pressure at the back section is proportional to the amount of the exiting gas particles and hence it is proportional to porosity.

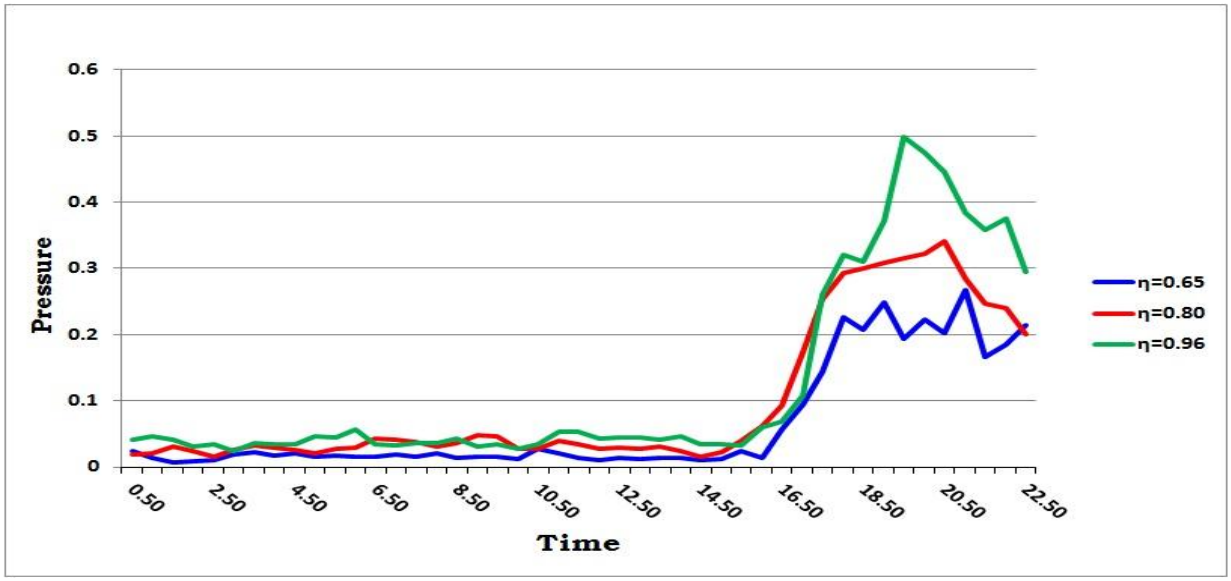

Fig 4.9 Porosity effect on the gas pressure at back area of the porous section during shock impact

4.3.3 Pressure difference across the porous section

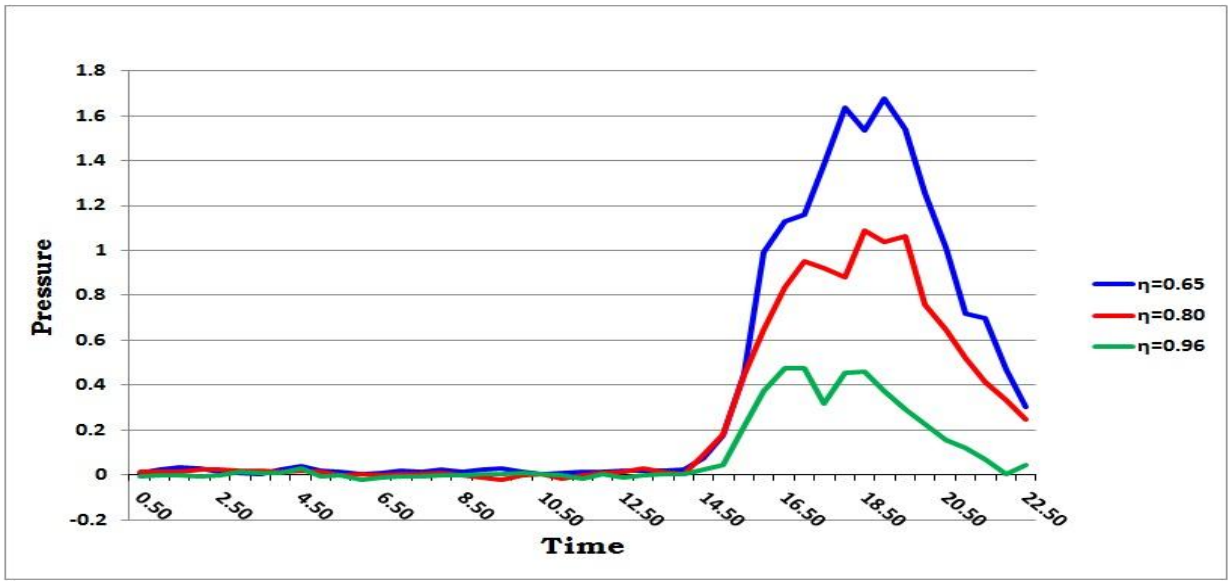

Fig 4.10 Porosity effect on the gas pressure difference between front and back areas of the porous section during shock impact

Fig 4.10 shows the pressure difference along the pores of the porous structure. It appears to be inversely proportional to porosity. It is quite obvious that the pressure at the front area is much higher than that at the back area and hence the difference in pressure across the porous section will have the same trend as that of pressure at the front section.

4.4 Orthogonal poles structure

In this configuration the poles are rotated 90 degrees and the poles will no longer be aligned with the normal direction of the shock wave but will be orthogonal with the flow direction. Fig 4.11 shows a schematic side view of the 6 pole arrangement. The porous length is chosen so that it is comparable to that of previous parallel porous cases. Dimensions of the gas channel remained unchanged.

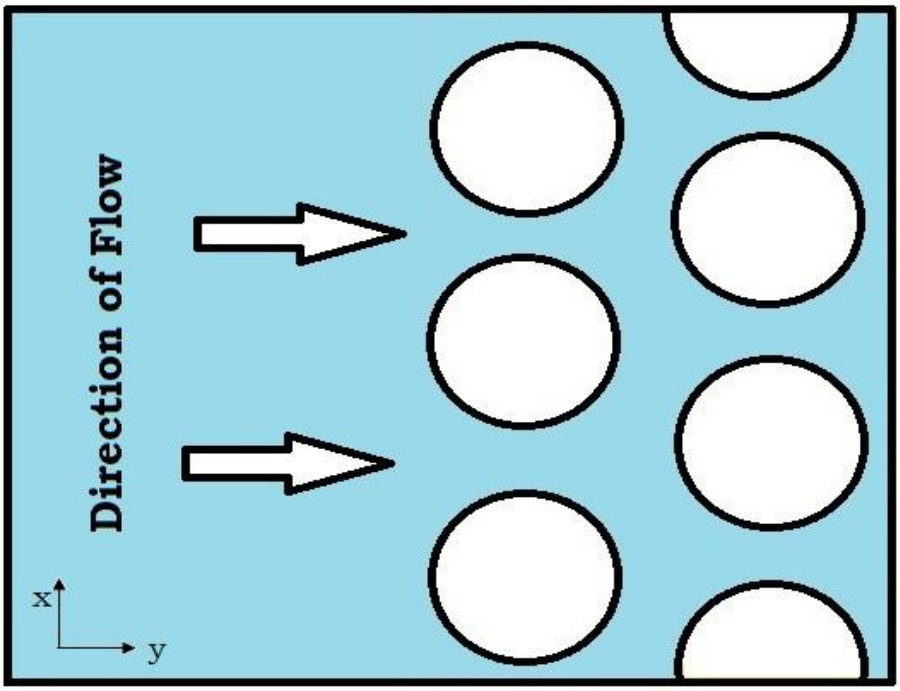

Fig 4.11 Side view of orthogonal poles structure

4.4.1 Pole orientation effect on the gas pressure

A typical shock tube model that contain a free standing orthogonal straight pole arrangement with η=0.80 was formed. The system was equilibrated first before the piston was allowed to accelerate which then moves to generate a shock wave that propagated in the gas channel. The value of the gas pressure in the front and back areas of the porous section is compared to the case of parallel poles with η=0.80.

According to fig 4.12, the gas pressure rise at the front area is higher in the orthogonal porosity case than that in the parallel porosity. On the other hand, the gas pressure rise at the back area is less in the orthogonal porosity case than that in the parallel porosity. The flow in the orthogonal poles case will face greater blockage area than that in the parallel poles case and the primary reflection will be stronger. Moreover, the spacing between poles is smaller and therefore less particles flow through the porous section. As a result the pressure difference along the pores is greater in the case of orthogonal orientation of the porous material.

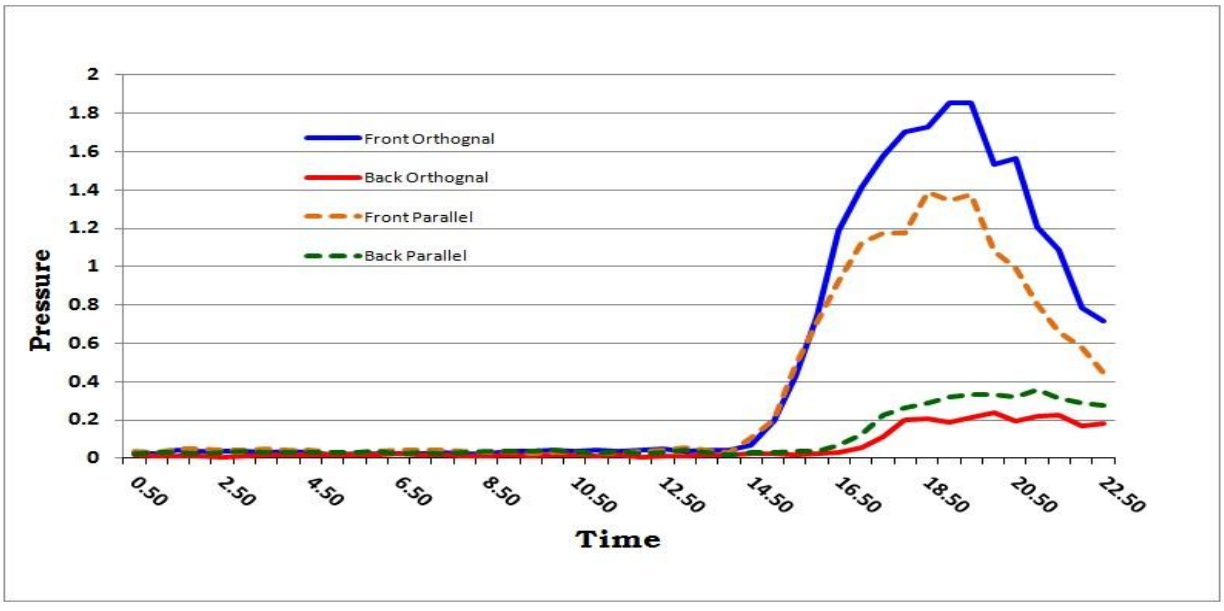

Fig 4.12 Pole orientation effect on the gas pressure during shock impact at front and back sections

Conclusion

The interaction of shock waves with nano-structured materials was investigated by using molecular dynamics. This work has been motivated by the promise of these materials to dissipate drastically fast traveling shock or blast waves at the nano-scales because their surface-to-volume ratio is substantially higher than in the case of macro-scale materials.

The interaction was setup by a piston in a stagnant gas moving with a velocity large enough to generate a shock wave upstream traveling through the gas molecules towards a solid wall target that is covered with a nano-structured porous material in front which provides the required protection. This setup allowed a preliminary evaluation of the effectiveness of the material in blast mitigation strategies. In order to provide a reference for comparison, the case of the shock impacting the target wall in the absence of a protective material was extensively investigated and documented first. This case also provided details of the fluid-structure interaction which involved the shock reflection at the front interface of the target wall, its transmission into the solid material as well as the deformation of the target. Although the setup of the interaction in this case may show similarities with the shock tube flow at the macro-scale level, there are notable differences between them, the most significant being the flow reversal immediately after the impact of the shock on the target wall as shown in the velocity profiles of figure 2.8. In the classical shock tube flow, the end wall is considered rigid and the flow behind the shock reflection is suddenly decelerated to full stagnation. In the present case, the wall is elastic and its time-dependent deformation and motion are the reasons for the flow reversal.

In MD the stress tensor and heat flux were evaluated by using relations which do not assume or invoke any constitutive law between stress and strain or heat flux and temperature. Shear and

bulk moduli were evaluated independently of constitutive relations. Our results suggest the presence of high-strain-rate effects in the solid wall material which show a moderate increase of its strength during the shock impact.

The increase of the target wall stress, strain as well as energy due to the transmitted wave during shock impact is proportional to the shock intensity and to the shock speed. However, the increase of initial gas density as well as the increase in the piston speed will increase the generated shock wave speed and intensity. Hence, the increase of the target wall stress, strain as well as energy due to the transmitted wave during shock impact is proportional to the initial gas density and the piston speed as well.

The presence of nano-porous material layers in front of the target wall appears to have beneficiary effects on its survivability. First, it reduces the stress magnitude observed inside the target wall by about 30 percent (in case of η=0.65) while the deposited energy is also decreased by about the same amount when compared to the non-protected target case which is equivalent to a fully porous material with 100 percent porosity. Second, it decreases the loading rate of the target wall and thus further protecting the integrity of the structure.

The increase of the target wall stress, strain as well as energy due to the transmitted wave during shock impact is inversely proportional to the porosity. Moreover, porosity causes time delay of the shock impact where time delay is proportional to the porosity.

Not only the magnitude of porosity affects the dynamics of the shock wave impact and reflection but the orientation of the poles attached to target wall. Other porosity parameters like number, size, shape, length and placement of poles will affect the flow characteristics during the impact and the reflection of shock wave.

Appendix

Speed of sound

The speed of sound can be predicted using molecular dynamics by disturbing a region of gas molecules and calculating the speed of formed wave by monitoring the wave motion inside the channel. By locating the peaks of the propagated wave at different times the speed can be calculated by dividing the distance between successive peaks by the time difference.

A simple gas channel consisting of 2880 gas molecules that are contained between two rigid walls was formed, all molecules are interacting according to SHRAT and rigid walls particles are fixed to a constant lattice positions by elastic springs.

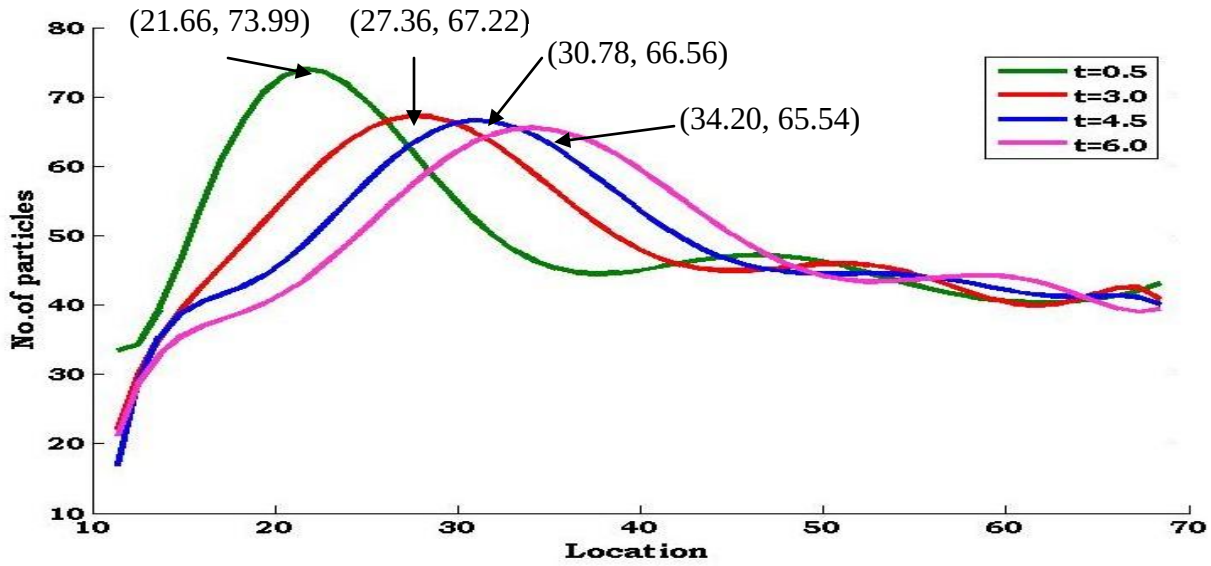

Fig A.1 The sound wave formed in the gas channel

After equilibration, the piston "left rigid wall" was accelerated and then allowed to move in a sinusoidal wave with an amplitude of 2.0 and period of 0.001π. The Piston was moved for only one cycle then stopped. The local properties of gas molecules were averaged every 100 time steps and then stored in a separate file.

The density profiles of the gas particles inside the channel were plotted and the sound wave was observed. MATLAB was used to plot the gas density profiles with an 8 order fitting polynomial, see fig A1. The peaks of the formed wave were tracked and speed of sound was calculated as follows:

$speed = \frac{\delta}{\Delta t}$ where: δ is the distance between any two peaks, Δt : time difference.

For the graph above we have the following possibilities

Distance between peeks	$\delta_{1,2} = 5.7$	$\delta_{1,3} = 9.12$	$\delta_{1,4} = 12.54$	$\delta_{2,3} = 3.42$	$\delta_{2,4} = 6.84$	$\delta_{3,4} = 3.42$
Time Difference	$\Delta t_{1,2} = 2.5$	$\Delta t_{1,3} = 4.0$	$\Delta t_{1,4} = 5.5$	$\Delta t_{2,3} = 1.5$	$\Delta t_{2,4} = 1.5$	$\Delta t_{3,4} = 1.5$
Speed of sound	2.28	2.28	2.027	2.28	2.28	2.28

Table A.1 speed of sound calculation results

Average value of speed of sound =2.24

Standard deviation = 0.1033

Speed of sound at 95% confidence = 2.24±0.2066

Publications from parts of this research

[1] A. Al-Qananwah, J. Koplik and Y. Andreopoulos, "Shock Wave Interactions with Nano-structured Materials: a Molecular Dynamics Approach" submitted to **Shock waves**, Springer, under review

[2] A. Al-Qananwah, J. Koplik and Y. Andreopoulos, "Molecular Dynamics Simulation of Shock Waves Interacting with Nano-structures", 62nd Annual Meeting of the APS Division of Fluid Dynamics, Volume 54, Number 19 , Sunday–Tuesday, November 22–24, 2009; Minneapolis, Minnesota.

References

[1] Gong M. and Andreopoulos Y. "*Shock Wave Impact on Monolithic and Composite Material Plates: The Preferential Aeroelastic Response*," Journal of Sound and Vibration 313, 171–194, (2008)

[2] Gong M. and Andreopoulos Y. "*Coupled fluid–structure solver: The case of shock wave impact on monolithic and composite material plates*", J. Computational Physics (2009), 228, 4400-4434, doi:10.1016/j.jcp.2009.03.009.

[3] Subramaniam, K.V., Nian, W. and Andreopoulos, Y., "*Response of an Elastic Structure Subject to Air Shock Considering Fluid-Structure Interaction*", International Journal of Impact Engineering, 36 (2009) pp. 965-974

[4] Andreopoulos, Y., Xanthos, S., and Subramaniam K. "*Moving shocks through metallic grids: their interaction and potential for blast wave mitigation*", Shock Waves, vol. 16(6), (2007)

[5] Nian W., Subramaniam K. and Andreopoulos Y. "*Response of an Elastic Structure Subject to Air Shock Considering Fluid-Structure Interaction*" J. Aerospace Engineering. 23, 176 (2010)

[6] Kazemi-Kamyab V., Kolluru Subramaniam K. and Yiannis Andreopoulos "*Stress transmission in porous materials impacted by shock waves*" J. Appl. Phys. 109(1), 013523 (2011); doi:10.1063/1.3517791.

[7] Seitz, M.W., and Skews, B.W., "*Effect of compressible foam properties on pressure amplification during shock wave impact*", Shock Waves, vol.15, 177-197, (2006)

[8] M.W Seitz and B.W. Skews, Shock Impact on Porous Plugs with a Fixed Gap between the Plug and a Wall, in B. Sturtevant, J. E. Shepherd, H. G. Hornung, eds., *Proceedings of the 20th International Symposium on Shock Waves* (World Scientific, Singapore) (1996).

[9] G. Mazor, G. Ben-Dor, O. Igra, O. and S. Sorek, "*Shock wave interaction with cellular materials*", Shock Waves vol. 3**,** 159 (1994)

[10] M.R. Baer and N.W. Nunziato, "*A two-phase mixture theory for the deflagration-to-detonation transition (ddt) in reactive granular materials*", International Journal of Multiphase Flow, Volume 12, Issue 6, 861 (1986)

[11] M.A. Biot, "General Theory of Three-Dimensional Consolidation", Journal of Applied Physics 12 155 (1941)

[12] A. Levy, S. Sorek, G. Ben-Dor, and J. Bear,"*Evolution of the balance equations in saturated thermoelastic porous media following abrupt simultaneous changes in pressure and Temperature"*, Transport in Porous Media, 21, 241-268, (1995)

[13] J. Bear and Y. Bachmat, *Introduction to Modeling Transport Phenomena in Porous Media* (Klumer, Dordrecht) (1990)

[14] A.A. Gubaidullin, A. Britan, and D.N. Dudko, "*Air shock wave interaction with an obstacle covered by porous material*", Vol. 13, No. 1, P. 41−48 (2003)

[15] J.G.M van deer Grinten, An Experimental Study Of Shock-Induced Wave Propagation In Dry Water-Saturated, And Partially Saturated Porous Media. PhD Thesis, Applied Physics Department, Eindhoven University of Technology, The Netherlands (1987).

[16] D. Smeulders and M.E.H. van Dongen, Linear Waves and Shock waves in Flexible and Rigid Porous Media. In Shock Wave Science and Technology Reference Library, M.E.H van Dongen, Editor Vol.1, Springer (2007)

[17] Levy, A., Ben-Dor, G., Skews, B.W. and Sorek, S., "*Head-On Collision of Normal Shock Waves with Rigid Porous Materials*", Experiments in Fluids, 15, 183-190, (1993)

[18] M.E.H van Dongen, D.M.J Smeulders, T. Kitarnura, K. Takayama, On the Modelling of Wave Phenornena in Permeable Foam. In: R. Brun, L.Z. Dumitrescu (eds.) Proceedings 19th International Symposium on Shock Waves, Marseille, Springer-Verlag. Vol. III, pp. 163-168 (1995).

[19] M. Yasuhara, S. Watanabe, K. Kitagawa, T. Yasue T. and M. Mizutani, "*Experiment on effects of porosity in the interaction of shock wave and foam*", Japanese Society of Mechanical, Engineering-International Journal, Series B 39, 287 (1996)

[20] A. Britan and G. Ben-Dor, "*Shock tube study of the dynamical behavior of granular materials*", International Journal of Multiphase Flow 32, 623 (2006)

[21] G. Ben-Dor, A. Britan, T. Elperin, O. Igra and J.P. Jiang, "*Experimental investigation of the interaction between weak shock waves and granular layers*", Experiments in Fluids 22, 432 (1997).

[22] K. Kitagawa, K., Takayama ans M. Yasuhara, "Attenuation of shock waves propagating in polyurethane foams", Shock Waves, Vol#15, 437 (2006)

[23] M.P Allen and D.J Tildesly, “Molecular simulation of liquids”, Oxford University Press, Oxford, 1987.

[24] J. Koplik and J. R. Banavar, “*Continuum deductions from molecular hydrodynamics”*, Annual review of fluid Mechanics 27, 257 (1995)

[25] Stankovic I, Hess S. and Kroger M “*Structural changes and viscoplastic behavior of a generic embedded-atom model metal in steady shear flow*” Physical Review E 69, 021509 (2004).

[26] Hess S. and Kroger M. “*Thermophysical properties of gases, liquids and solids composed of particles interacting with a short-range attractive potential*", Phys. Rev. E 64, 011201 (2001).

[27] Hess S. and Kroger M, “*Elastic and Plastic Behavior of Model Solids*”, TECHNISCHE MECHANIK, Band 22, Heft 2, (2002)

[28] Hess s., Kroger M, and Hoover W. G., “*Shear modulus of fluids and solids*”, Physica A 239 (1997)

[29] J. Haile, “*Molecular Dynamics Simulation: Elementary Methods*” New York: John Wiley & Sons Inc (1997)

[30] Murray S. Daw and M. I. Baskes “*Embedded-atom method: Derivation and application to impurities, surfaces, and other defects in metals*” Phys. Rev. B 29, 6443–6453 (1984)

[31] S. M. Foiles, M. I. Baskes, and M. S. Daw “*Embedded-atom-method functions for the fcc metals Cu, Ag, Au, Ni, Pd, Pt, and their alloys*” Phys. Rev. B 33, 7983–7991 (1986)

[32] Denis J. Evans and Gary P. Morriss "*Statistical Mechanics of Non-Equilibrium Liquids*" Academic Press, London (1990)

[33] D. H. Tsai and S. F. Trevino, "Thermal relaxation in a dense liquid under shock compression", Physical Review A, vol. 24, no. 5, pg. 2743 (1981)

[34] B. L. Holian, W. G. Hoover, B. Moran and G. K. Straub, "*Shockwave structure via non-equilibrium molecular dynamics and Navier-Stokes continuum mechanics*", Physical Review A, vol. 22, no. 6, pg. 2798 (1980)

[35] B. L. Holian, "*Modeling shock wave deformation via molecular dynamics*", Physical Review A, vol. 37, no. 7, pg. 2562 (1988)

[36] Woo, M. and Greber, I., "*Molecular dynamics simulation of piston-driven shock wave in hard sphere gas*", AIAA Journal. v37 i2. 215-221, (1999)

[37] William G. Hoover, "*Structure of a Shock-Wave Front in a Liquid*"**,** Physical Review Letters, Vol. 42, 1531 - 1534 (1979)

[38] S. Schlamp, B. C. Hathorn, T. E. Hofmann, P. Simon, "*Shock wave structure in dense nitrogen: Steady-state profile and unsteady processes*", AIAA Paper 2005-5212, (2005)